

Solid-State ^{31}P NMR of Nucleotide Binding Proteins



Dissertation zur Erlangung des Doktorgrades der Naturwissenschaften
(Dr. rer. nat.) der Naturwissenschaftlichen Fakultät III
-Biologie und Vorklinische Medizin-
der Universität Regensburg

vorgelegt von
Adriana Iuga
aus Baia Mare, Rumänien
Oktober 2004

Promotionsgesuch eingereicht am:

Die Arbeit wurde angeleitet von: Prof. Dr. Eike Brunner

Prüfungsausschuss:
Prof. Dr. Günter Hauska (Vorsizender)
Prof. Dr. Eike Brunner (1. Gutachter)
Prof. Dr. Dr. Hans Robert Kalbitzer (2. Gutachter)
Prof. Dr. Reinhard Sterner (3. Prüfer)

Table of Contents

1	Introduction	1
1.1	Biological Background	1
1.2	Goal of the Thesis	7
2	Principles and Techniques of Solid-State NMR	10
2.1	Internal Magnetic Interactions of ^{31}P Nuclei and their Hamiltonians	10
2.1.1	Zeeman Interaction	11
2.1.2	Chemical Shift Interaction	12
2.1.3	Dipole-Dipole Interaction	15
2.1.4	Indirect Spin-Spin Interaction	16
2.2	High Resolution NMR Techniques for Solid-State	17
2.2.1	Magic Angle Spinning	17
2.2.2	Cross-polarization	20
2.2.3	Heteronuclear Dipolar Decoupling	22
3	Materials and Methods	30
3.1	Materials	30
3.2	Preparation of Protein Samples	31
3.2.1	Ras Expression, Purification, and Exchange of Nucleotide	31
3.2.2	Ras Crystallization	33
3.3	NMR Methods	35
3.3.1	EXSY (EXchange SpectroscopY) and ^1H Spin Diffusion	35
3.3.2	PMLG (Phase Modulated Lee-Goldburg)	37
3.3.3	Refocused INADEQUATE (Incredible Natural Abundance Double QUAntum Transition Experiment)	40
3.3.4	Rotational Resonance	41
3.3.5	Temperature Calibration	42
3.3.5.1	2.5 mm ZrO_2 rotor	42
3.3.5.2	4 mm ZrO_2 rotor	44
4	Results and Discussion	47

Table of Contents

4.1	Solid-State ^{31}P NMR Spectroscopy of Phosphorylated Amino Acids	47
4.2	Solid-State ^{31}P NMR Spectroscopy of Ras·Mg $^{2+}$ ·GppCH $_2$ p	55
4.2.1	Solid-State ^{31}P NMR Spectroscopy of Ras(wt)·Mg $^{2+}$ ·GppCH $_2$ p	55
4.2.2	Ras effector Loop Mutants in the GppCH $_2$ p-Bound State	65
4.2.2.1	Solid-State ^{31}P NMR Spectroscopy of Ras(T35S)·Mg $^{2+}$ ·GppCH $_2$ p	66
4.2.2.2	Solid-State ^{31}P NMR Spectroscopy of Ras(T35A)·Mg $^{2+}$ ·GppCH $_2$ p	68
4.3	Solid-State ^{31}P NMR Spectroscopy of Ras·Mg $^{2+}$ ·GppNHp	72
4.3.1	Solid-State ^{31}P NMR Spectroscopy of Ras(wt)·Mg $^{2+}$ ·GppNHp	72
4.3.2	Ras Effector Loop Mutants in the GppNHp-Bound State	81
4.3.2.1	Solid-State ^{31}P NMR Spectroscopy of Ras(T35S)·Mg $^{2+}$ ·GppNHp	82
4.3.2.2	Solid-State ^{31}P NMR Spectroscopy of Ras(T35A)·Mg $^{2+}$ ·GppNHp	86
4.4	Solid-State ^{31}P NMR Spectroscopy of Ras·Mg $^{2+}$ ·GTP γ S	91
5	Summary and Conclusions	93
6	Bibliography	96

1. Introduction

1.1 Biological Background

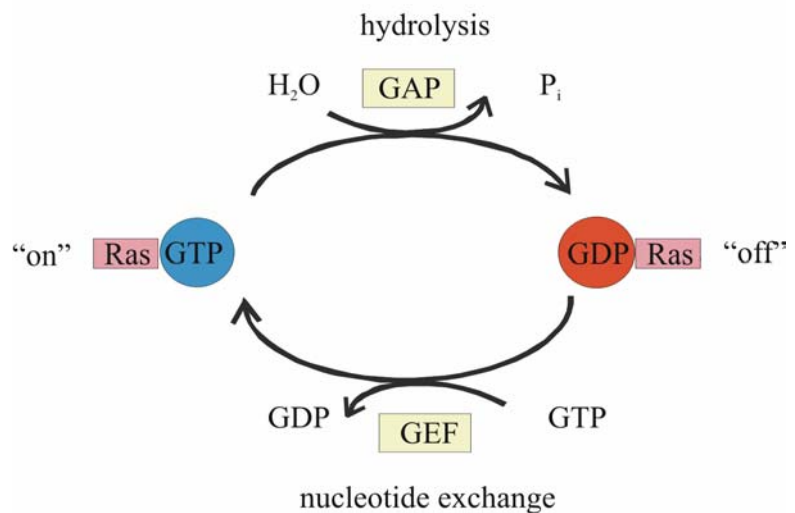
Guanine nucleotide binding proteins (G proteins) are a large family of molecules responsible for signal transduction between transmembrane receptors and cellular effectors [Wittinghofer *et al.*, 2000; Bos, 1997]. Signal transducing G proteins occur in two forms: “small G proteins” that are low molecular weight monomeric GTP-binding proteins (Ras superfamily) and heterotrimeric G proteins that are composed of α , β , and γ subunits. The structure of these proteins share a structural core called G domain, consisting of six β strands and five α helices [Wittinghofer *et al.*, 1991]. The large superfamily of Ras-like GTPases is divided into several families, one of which is the Ras family. The beginning of Ras research can be traced back to 1964 when Jennifer Harvey observed that the preparation of a virus, taken from a leukaemic rat, induced sarcomas in new born rodents (thereby the name Ras is derived from **rat sarcoma**). Ras is called an oncogene, a gene that is able to induce tumors in animals or in cell cultures [Scolnick *et al.*, 1979; Lowy *et al.*, 1993]. In humans, the Ras family consists of three Ras proteins: Harvey (H)-Ras, Kirsten (K)-Ras, and neuroblastoma (N)-Ras [Kuhlmann *et al.*, 2000]. Numerous studies have shown that different Ras proteins are activated in different tumors (K-Ras in colon and pancreatic carcinomas, H-Ras in bladder and kidney carcinomas, and N-Ras in myeloid and lymphoid cancers) [Bos, 1989]. The Ras proteins consist of 189 amino acids, having a molecular mass of 21 kDa [Wittinghofer *et al.*, 2000]. It has been shown that the first 166 residues of Ras are necessary and sufficient for its biochemical properties. The C terminus is only necessary for localization in the plasma membrane and is not involved in any other interactions [Willingham *et al.*, 1980]. The Ras protein is strongly conserved among different species. It is found in fruit fly, nematode, yeast, and mammals. The first 85 amino acids of N-, H-, and K-Ras are identical and the next 80 amino acids exhibit 85% homology between any pair of Ras isoforms. [Malumbres *et al.*, 1998]. The presented studies were carried out on human H-Ras (in the following H-Ras will be abbreviated Ras) with truncated C terminus (amino acids 1-166) and a molecular mass of 19 kDa.

MTEYKLVVVG AGGVGKSALT IQLIQNHFVD EYDPTIEDSY RKQVVIDGET CLLDILDITAG QEEYSAMRDQ
 YMRTGEGFLC VFAINNTKSF EDIHQYREIQI KRVKDSDDVP MVLVGNKCDL AARTVESRQA QDLARSYGIP
 YIETSAKTRQ GVEDAFYTLV REIRQHKLRK LNPPDESGPG CMSCKCVLS

Figure 1.1 Primary structure of H-Ras consisting of 189 amino acid residues (shown here in 1 letter code). Amino acids 1 to 166 are marked in red, indicating the truncated form of Ras employed in our studies. The N-terminal residue in the truncated form of Ras is methionine (M) and the C-terminal residue is histidine (H).

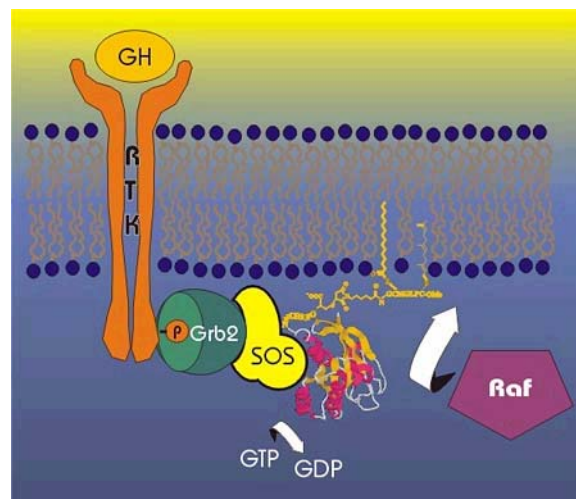
Ras acts as a molecular switch (Figure 1.2) [Wittinghofer *et al.*, 1991]. It is complexed with GDP in its resting (“off”) state [Wittinghofer *et al.*, 1995]. In its active (“on”) state, GTP is bound to the molecule.

Figure 1.2 Activation - inactivation cycle of Ras. Ras is inactive in the GDP-bound form. It can be activated by the action of GEFs (guanine nucleotide exchange factors). In the GTP-bound form, it interacts with effectors. Deactivation of the active state results in the hydrolysis of GTP to GDP and inorganic phosphate (P_i).



Ras molecules relay signals from receptor tyrosine kinases (RTKs) to the nucleus to promote cell differentiation, proliferation, and apoptosis in all multicellular organisms. As mentioned before, Ras is activated by GDP-to-GTP exchange, initiated by membrane-bound receptors such as RTKs. A resting cell maintains its RTKs as inactive monomers (separate subunits).

Figure 1.3 Ras signal transduction pathway. Recruitment of the RasGEF SOS (son-of-sevenless) to the plasma membrane by activating growth factor GH (growth hormone) bound RTKs leads to the activation of Ras. Activated Ras interacts with an effector (e.g., Raf) which activates the MAP (mitogen activated protein) kinase module thus permitting the transmission of the biological signal to the nucleus.



The binding of a peptide such as the growth hormone (GH) causes the RTKs to dimerise, and this activates their kinase activities, leading to autophosphorylation. This phosphorylation produces binding sites for proteins with Src (where Src is an oncogene originally isolated from a *Sarcom*) homology 2 (SH2) domains, such as growth factor receptor bound protein 2 (Grb2). Grb2, complexed with son-of-sevenless protein (SOS) then binds to the RTK, which activates SOS. SOS is a guanine nucleotide exchange factor (GEF) which activates Ras by inducing it to release GDP and exchange it by GTP [Bos, 1997].

In the active state Ras interacts with so-called downstream targets or effectors, which in turn communicate with other partners located further downstream in the signal cascade. Effectors are defined as proteins that interact much more tightly with the GTP-bound form of the nucleotide binding protein than with its GDP-bound form. This interaction is determined by the hydrolysis of protein-bound GTP to GDP, which restores the GDP-bound form and terminates the interaction with the effector. Recently, multiple effector pathways have been found contributing to the Ras function [Vojtek *et al.*, 1998].

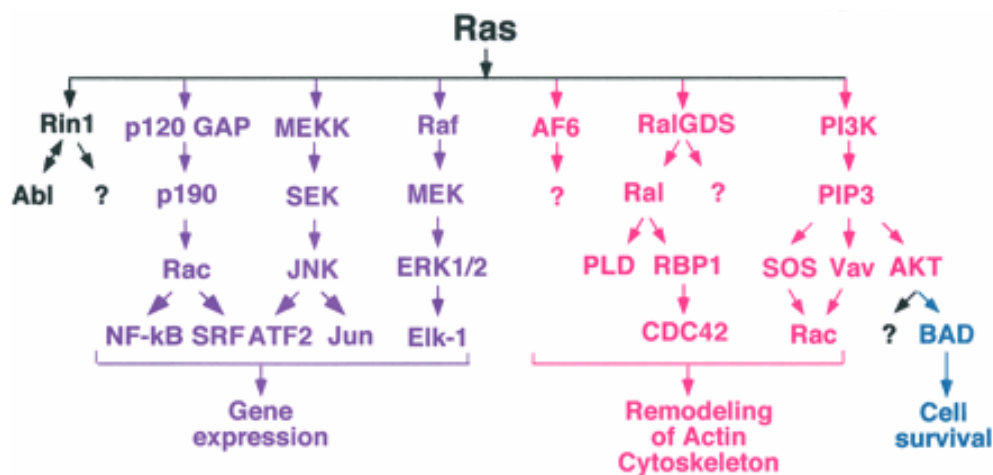


Figure 1.4 Multiple effector pathways contribute to Ras function. Once in the active form, Ras is able to stimulate a number of effector proteins, each representing distinct signalling pathways. p120 GAP - GTPase activating protein; p190 - GAP for Rho family members; SEK, SAPK/JNK kinase; MEKK, MEK, ERK1/2 kinase; PIP3 - phosphatidylinositol; SRF - serum response factor; PLD - phospholipase D; RalGDS - Ral guanine nucleotide dissociation stimulator; AF6 - fusion partner for chromosome 6; Rin1 - Ras interaction/interference; Rac - related to A and C kinases; CDC42 - cell division cycle 42; RBP1 - RNA-binding protein 1.

One intriguing aspect of Ras signalling is that Ras can promote both cell death and cell survival through the interaction with distinct effectors. For example, activation of the best known signalling pathway downstream from Ras, i.e. the serine-threonine kinase pathway Raf-MEK-ERK promotes apoptosis (programmed cell death), while activation of PI3K

(phosphatidylinositol-3-kinase) promotes cell survival (see Figure 1.4). There is no sequence homology and no functional relationship among these effectors. So far, only for three effectors namely Raf, PI3K, and RalGDS, the activation of their biological function by Ras could be demonstrated [Kuhlmann *et al.*, 2000].

The intrinsic GTPase reaction is usually very slow and can be accelerated by several orders of magnitude by GTPase activating proteins (GAP). In the resting state, Ras is activated by the action of guanine exchange factors (GEF) catalysing the dissociation of GDP, thus facilitating subsequent binding to GTP. The latter is the more abundant guanine nucleotide in living cells [Feig, 1994; Ma *et al.*, 1997; Wittinghofer *et al.*, 1995]. The conversion of the Ras gene from a proto-oncogene to an oncogene is the result of a point mutation at position 12, 13, or 61 [Barbacid, 1987]. The mutated proteins are continuously activated, producing a permanent signal since the intrinsic and the GAP stimulated GTPase activities are strongly reduced [McCormick, 1991]. Together with mutations in some other genes, e.g. the gene of the tumor suppression p53, the cell becomes transformed which finally results in tumor growth. This happens because the Ras protein regulates diverse extracellular signalling pathways for cell growth, differentiation, and apoptosis. The deregulated function of other cellular components can then cause aberrant Ras protein function in the absence of mutations of the Ras genes themselves. Thus, although oncogenic Ras is not alone responsible for cell transformation but only in concert with other genetic disruptions, Ras is one of the most frequent oncogenes. It is estimated that up to 30% of human tumors carry a mutated Ras oncogene [Takai *et al.*, 2001].

Recently, Bivona *et al.* [2003] have shown that the Ras protein is also activated on the Golgi apparatus inside the cell (see Figure 1.5). The Golgi is involved in protein secretion. It thereby controls how signals leave the cell. The critical event in the pathway described by Bivona *et al.* is an increase in the intracellular level of calcium ions, which causes a Ras guanine-nucleotide-exchange factor, known as RasGRP1, to move to the Golgi, and a Ras GTPase-activating protein, CAPRI (Ca²⁺-promoted Ras inactivator), to move to the plasma membrane. We know that GEFs activate Ras and GAPs turn Ras off. It was suggested [Di Fiore, 2003] that the relative levels of RasGRP1 and CAPRI determine, whether Ras signals primarily emanate from the plasma membrane or from intracellular membranes. Bivona *et al.* predict that Ras signalling occurs mainly from the Golgi in cells displaying persistent intracellular increases of Ca²⁺ level. But when these rises are short-lived, signalling might be mostly from the plasma membrane.

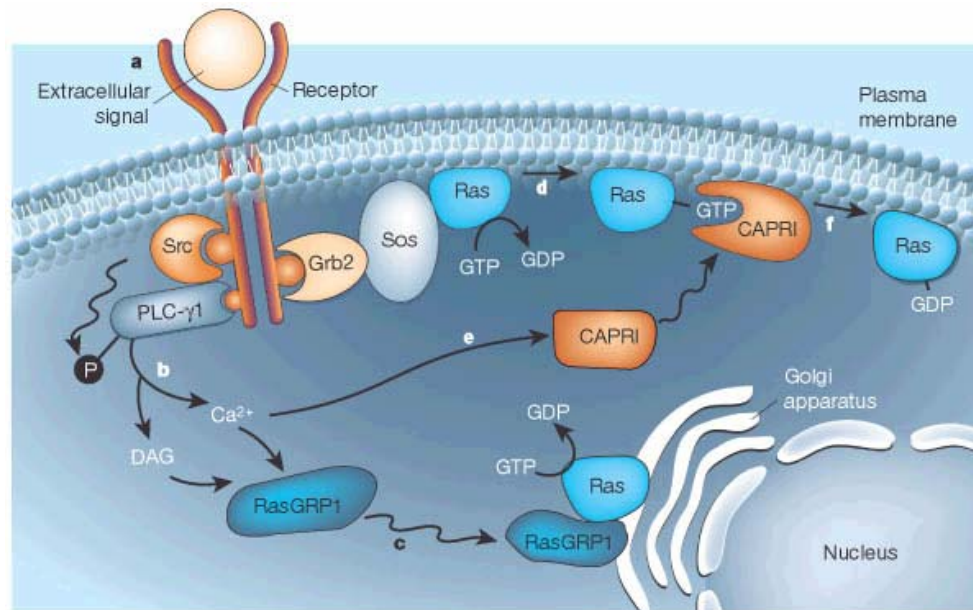


Figure 1.5 Activation of Ras in different cellular locations. **a:** When receptors on the cell surface are activated, they recruit the enzyme Src. Simultaneously, another enzyme, phospholipase C γ 1 (PLC- γ 1), is recruited and phosphorylated by Src (represented by a circled 'P'), activating it. **b:** PLC- γ 1 leads to the generation of diacylglycerol (DAG) and an increase in the level of Ca²⁺ ions. **c:** DAG and Ca²⁺ cause a cytoplasmic protein, RasGRP1, to move to the Golgi. This protein activates Golgi-associated Ras, by catalysing the exchange of GDP by GTP. This new pathway coexists in the cell with the pathway: receptor→Grb2→Sos. The latter protein activates Ras at the plasma membrane (**d**) in a Ca²⁺-independent way. **e:** The increase in Ca²⁺ level also leads to the activation of CAPRI (Ca²⁺-promoted Ras inactivator) and, possibly, to its transport to the plasma membrane. **f:** CAPRI inhibits Ras by stimulating its intrinsic GTPase activity, which hydrolyses GTP to GDP.

The structure of Ras was determined both in diphosphate-bound [Tong *et al.*, 1991] and triphosphate-bound form. For this purpose, non- or slowly hydrolysing GTP analogues were used: GppNHp [Pai *et al.*, 1989] and GppCH₂p [Brünger *et al.*, 1990] where the β - γ oxygen bridge was replaced by NH or CH₂ group (see Figure 1.6). The Ras structure was also determined in the GTP γ S-bound form [Scherer *et al.*, 1988]. For the GTP γ S analogue, the oxygen of the γ -phosphate group is replaced by a sulphur atom resulting in a smaller polarization of P γ leading to a slower rate of hydrolysis. Among the described analogues, GTP γ S is the most unstable one [Stumber *et al.*, 2002].

The X-ray crystallographic studies were carried out on truncated Ras (amino acids 1-166 or 1-171) expressed in *E.coli*. X-ray studies of full length Ras were also made, but the C-terminal part was not well enough resolved. The structure encompasses five α helices and six β strands. The β strands form a mixed β sheet. Because of the mainly parallel β strands, both surfaces are hydrophobic and must interact with layers of amphiphatic helices to mediate contact with the surrounding solvent.

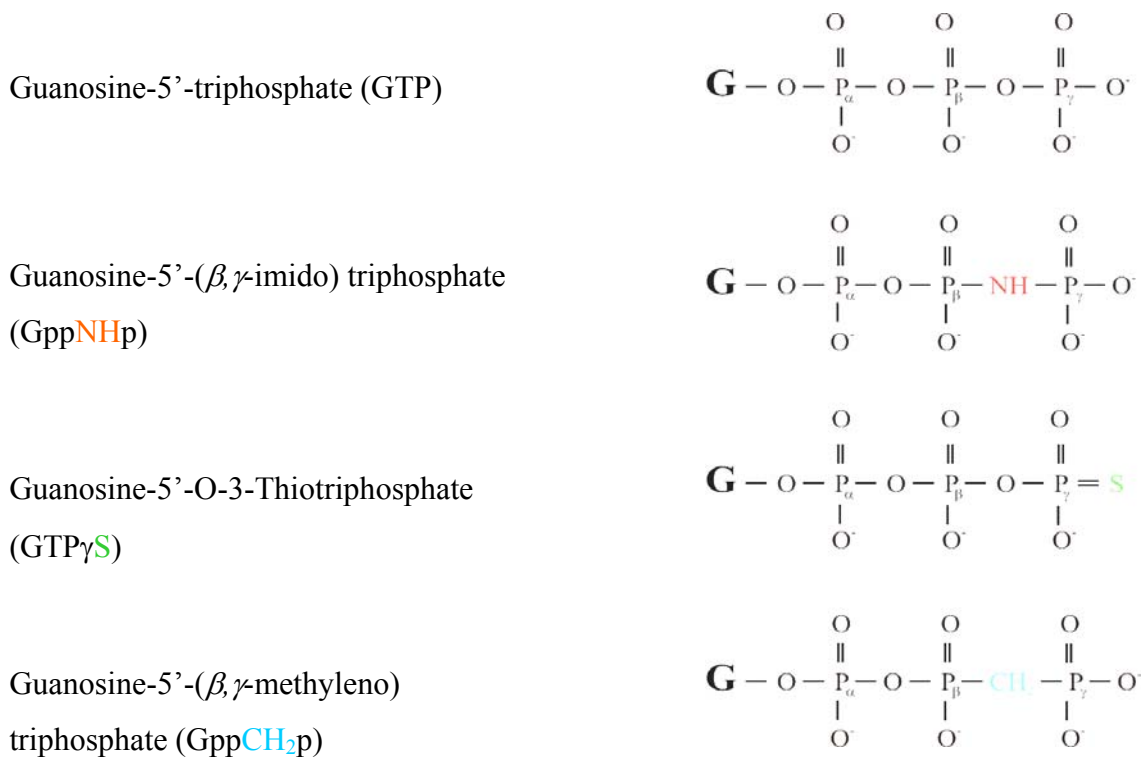


Figure 1.6 Frequently used triphosphates.

Structural studies show that the differences between Ras·GDP and Ras·GppNHp (see Figure 1.7) are confined to two small flexible areas which were denoted as switch I (residues 30-38, within loop L2 and $\beta 2$) and switch II (residues 60-76, within loop L4 and helix $\alpha 2$) [Milburn *et al.*, 1990].

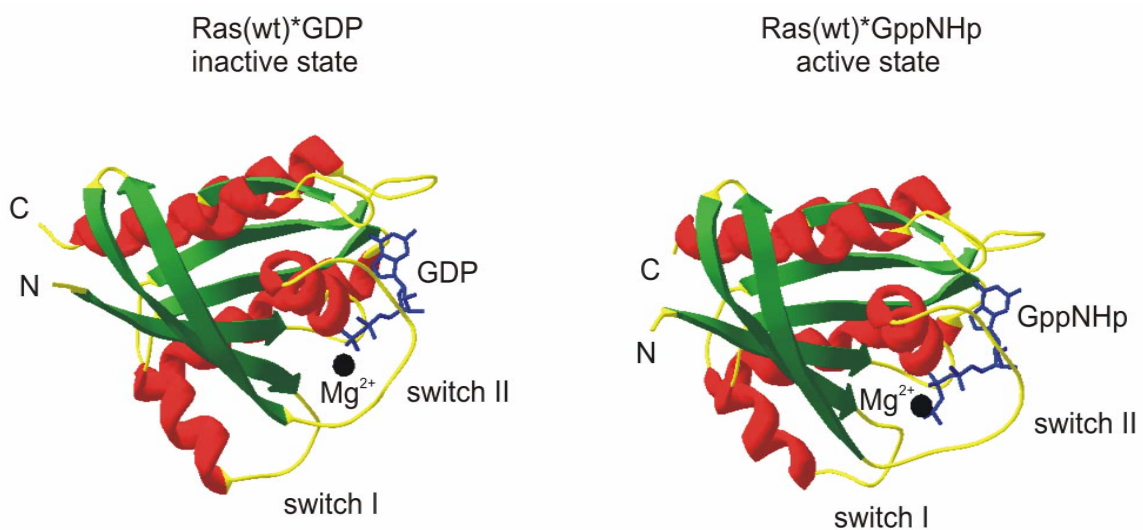


Figure 1.7 Schematic representation of GDP- and GppNHp-bound structures of Ras.

There are five acidic residues in switch I: Asp30, Glu31, Asp33, Glu37, and Asp38. These five residues create a negatively charged surface that interacts with GAPs. Originally, Gln61 in switch II was considered to be essential for GTP hydrolysis, but subsequent experiments and theoretical studies have excluded this model [Li *et al.*, 2004].

The determined structures showed how the conformational change is triggered since both switch regions are bound to the γ -phosphate through two invariant residues: switch I by Thr35 and switch II by Gly60. The conformational change can be described best as a loaded-spring mechanism where release of the γ -phosphate after GTP hydrolysis allows the two switch regions to relax into the conformation characteristic for the GDP-bound state (Figure 1.8).

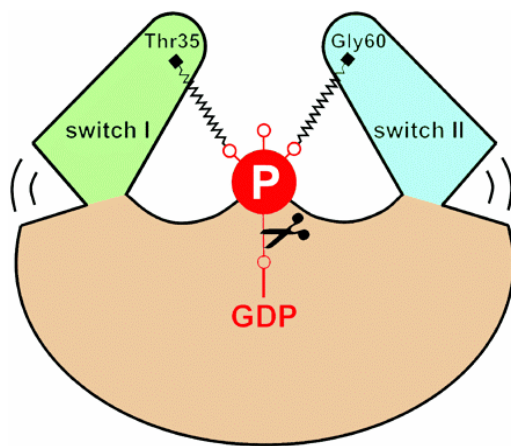


Figure 1.8 Schematic view of the switch mechanism where the switch I and II domains are bound to the γ -phosphate via the backbone NH groups of the conserved Thr and Gly residues (symbolized by springs in this figure). Release of the γ -phosphate group after GTP hydrolysis allows the switch regions to relax into a different conformation.

1.2 Goal of the Thesis

The switching process of Ras between the GTP-bound "on" state and the GDP-bound "off" state is accompanied by conformational changes in the switch I and switch II region. In the "on" state, hydrogen bonding occurs between the γ -phosphate of the nucleoside triphosphate and two conserved residues (Thr35 and Gly60 in Ras). Previous liquid-state ^{31}P NMR spectroscopic experiments have shown that the small GTPase Ras complexed with a metal ion (Mg^{2+}) and nucleoside triphosphates such as GppNHp [Geyer *et al.*, 1996; Spoerner *et al.*, 2001] exhibits an equilibrium between two conformational states in solution. Similar effects could be observed for another member of the Ras superfamily, Ran, complexed with Mg^{2+} -GTP [Geyer *et al.*, 1999]. One of these conformers, the so-called state 2, appears to be very similar to the conformation of Ras in the "on" state which is observed for Ras interacting

with effector proteins. That means, state 2 is stabilized by effector binding. In contrast, an "open", disordered conformation of the switch regions similar to the GDP-bound state is assumed for the other conformer, state 1 [Spoerner *et al.*, 2001]. The conserved threonine residue (Thr35 in Ras) located in switch I is then no longer coordinated to the Mg^{2+} ion. Most likely, the above-described hydrogen bond to the γ -phosphate group does also not exist in state 1.

Intriguingly, X-ray crystallographic studies have revealed only one single conformation for wild-type Ras complexed with GppNHp in the presence of Mg^{2+} (Ras(wt)· Mg^{2+} ·GppNHp) [Pai *et al.*, 1990]. The same is in principle true for Ras(wt)· Mg^{2+} ·GppCH₂p although a slightly different effector loop structure is observed for the four crystallographically inequivalent molecules in the unit cell [Brünger *et al.*, 1990]. The switch II region exhibits a relatively low electron density in the X-ray diffraction patterns for both complexes which may be considered as an indication for conformational disorder and/or the presence of internal thermal motions. The presence of the two conformations (states 1 and 2) in the crystalline samples could, however, be detected in initial solid-state ³¹P NMR spectroscopic studies of Ras(wt)· Mg^{2+} ·GppNHp microcrystals [Stumber *et al.*, 2002]. It is, furthermore, important to note that the conformational equilibrium is shifted towards the "open" state 1 for proteins with partial loss-of-function mutations of the totally conserved threonine residue (Thr35 in Ras) as it could be shown by liquid-state ³¹P NMR spectroscopy [Spoerner *et al.*, 2001]. The affinity of these effector loop mutants (partial loss-of-function mutants) such as Ras(T35S) or Ras(T35A) to various effector proteins is drastically decreased while the overall structure of the molecule is very similar to the wild-type. X-ray crystallography turned out to be unable of resolving the structure of the two switch regions for Ras(T35S) bound to the GTP-analog GppNHp [Spoerner *et al.*, 2001]. This is in line with the fact that the switch regions in state 1 - which is the preferred state of Ras(T35S) - could not be detected in Ras(wt) as well [Pai *et al.*, 1990; Brünger *et al.*, 1990].

Thus, X-ray crystallography fails to detect one of the two states. It also does not allow to study the mobility of individual molecules, motions of molecular groups or chemical exchange processes. Therefore, dynamic aspects of solid-state structures should be studied by solid-state NMR spectroscopy. Chemical exchange phenomena can be detected even if the system is in equilibrium. This is because NMR detects the molecular motion itself, rather than the numbers of molecules in different states. The aim of this work was to study the reason for the obvious contradiction between liquid-state NMR and X-ray crystallographic studies observed for the Ras protein and to correlate these results with the solid-state NMR data.

Furthermore, the effector loop mutants Ras(T35S) and Ras(T35A) were also studied especially with respect to intramolecular conformational changes and other thermal motions.

2. Principles and Techniques of Solid-State NMR

2.1. Internal Magnetic Interactions of ^{31}P Nuclei and their Hamiltonians

During the last three decades, ^{31}P NMR has made substantial contributions to our basic knowledge of biological structures and processes. Since the spin $\frac{1}{2}$ nucleus ^{31}P exhibits 100% abundance and a substantially high gyromagnetic ratio ($\gamma = 10.8394 \times 10^7 \text{ rad s}^{-1} \text{ T}^{-1}$) solid-state ^{31}P NMR combined with MAS (magic angle spinning), CP (cross-polarization), and high power decoupling has developed into a powerful tool for elucidating structure and dynamics in many biological solids [Bak *et al.*, 2001; McDowell *et al.*, 1996; Pinheiro *et al.*, 1994; Stumber *et al.*, 2002; van Dam *et al.*, 2000].

The ^{31}P nuclear spin interactions relevant for biological solids and their Hamiltonians will be discussed briefly below. The width of the nuclear magnetic resonance signals arises from so-called internal magnetic interactions. In particular, it is determined by the simultaneous influence of the chemical shift anisotropy (CSA) and the magnetic dipole-dipole interaction for spin $\frac{1}{2}$ nuclei. CSA arises from the nonspherical distribution of electrons in the environment, especially the phosphate group screening the external magnetic field spatially anisotropic. Phosphate groups have a relatively large CSA. Dipole-dipole interactions arise from the mutual magnetic coupling between neighbouring spins through space. In a rigid lattice, the dipolar interactions split the energy levels which usually results in a line broadening for multi-spin systems.

The state of a spin system and its response after a perturbation is given by both internal and external interactions. The external part (\hat{H}_{ext}) consists of the Zeeman interaction of the spins with the static magnetic field \mathbf{B}_0 (\hat{H}_0) and with a time dependent field $\mathbf{B}_1(t)$, (\hat{H}_1), induced by a radio-frequency (r.f.) pulse. The internal Hamiltonian (\hat{H}_{int}) describes the interaction of a spin with its surrounding and contains the chemical shift and the magnetic dipole-dipole interactions. The chemical shift anisotropy provides insight into the electronic structure and bonding, while the dipolar coupling offers access to the internuclear distances.

2.1.1 Zeeman Interaction

The external interactions can be given by the following Hamiltonian:

$$\hat{H}_{ext} = \hat{H}_0 + \hat{H}_1 \quad [2.1]$$

The coupling of a spin to an external static magnetic field, the nuclear Zeeman interaction, is described by:

$$\hat{H}_0 = -\boldsymbol{\mu} \cdot \mathbf{B}_0 = -\gamma \hat{I}_z B_0 = \omega_0 \hat{I}_z \quad [2.2]$$

where $\boldsymbol{\mu}$ is the nuclear magnetic moment, ω_0 the Larmor frequency at which the spin polarisation axis precesses around the external magnetic field, and \hat{I}_z the z component of the \hat{I} spin angular momentum operator.

The interaction of a spin with a r.f. field is:

$$\hat{H}_1 = -\boldsymbol{\mu} \cdot \mathbf{B}_1 \quad [2.3]$$

If the r.f. field is applied along the x -direction of the static laboratory frame (LF) the external part of the Hamiltonian for one spin is:

$$\hat{H}_{ext} = \omega_0 \hat{I}_z + \omega_1 \cos(\omega_{ref} t + \Phi_p) \hat{I}_x \quad [2.4]$$

where ω_{ref} is the spectrometer reference frequency at which the magnitude ω_1 of the r.f. field oscillates, \hat{I}_x the x component of the \hat{I} spin angular momentum operator, and Φ_p the phase of the r.f. pulse. It is useful to imagine that the r.f. field is a sum of two rotating components. Both components rotate in the xy -plane, at the same frequency but in opposite directions. One component rotates in the same sense as the spin precession. The other component rotates in the opposite sense to the Larmor frequency. It may be shown [Levitt, 2001] that this last component of the r.f. field has almost no influence on the motion of the spins and may, therefore, be neglected.

Thus, the external Hamiltonian is:

$$\hat{H}_{ext} = \omega_0 \hat{I}_z - \left(\frac{\omega_1}{2} \right) \left[\hat{I}_x \cos(\omega_{ref} t + \Phi_p) + \hat{I}_y \sin(\omega_{ref} t + \Phi_p) \right] \quad [2.5]$$

The factor $1/2$ arises because half of the r.f. amplitude is wasted to the component rotating in the opposite sense to Larmor frequency. \hat{I}_y is the y component of the \hat{I} spin angular momentum operator.

Note that the Hamiltonians are given in angular frequency units. The oscillatory time-dependence of the nuclear spin Hamiltonian can be removed by transforming it into a rotating frame (RF). In the RF, the relative Larmor frequency is given by $\omega_0 - \omega_{ref}$ and the Hamiltonian becomes time independent:

$$\hat{H}_{ext} = (\omega_0 - \omega_{ref}) \hat{I}_z - \left(\frac{\omega_1}{2} \right) (\hat{I}_x \cos \Phi_p + \hat{I}_y \sin \Phi_p) \quad [2.6]$$

For on resonance irradiations ($\omega_0 = \omega_{ref}$) and in RF the Hamiltonian becomes:

$$\hat{H}_{ext} = - \left(\frac{\omega_1}{2} \right) (\hat{I}_x \cos \Phi_p + \hat{I}_y \sin \Phi_p) \quad [2.7]$$

The external interactions are usually much larger than the internal interactions. In other words, the nuclear spins are more strongly coupled to the external apparatus than to their own molecular environment. Therefore, the internal interactions can be treated as first-order perturbations with respect to $\hat{H}_0 = \omega_0 \hat{I}_z$. In the high-field NMR of spin $1/2$ nuclei, the perturbation theory is equivalent with neglecting terms that do not commute with \hat{I}_z . The terms that commute with \hat{I}_z are denoted as secular terms. The neglected terms are called non-secular.

2.1.2 Chemical Shift Interaction

The external magnetic field \mathbf{B}_0 induces currents in the electron clouds of the molecule. The circulating molecular currents in turn generate a magnetic field. Thus, the interaction of the static magnetic field with the electronic environment induces a field at the site of the

nucleus. This interaction results in the so-called chemical shift, i.e. a deviation of the resonance frequency of a nucleus with respect to the Larmor frequency. The induced field is, to a very good approximation, linearly dependent on the applied magnetic field, and can be written:

$$\mathbf{B}_{\text{induced}} = \delta \mathbf{B}_0 \quad [2.8]$$

where δ is a dimensionless second rank tensor, the chemical shift tensor.

The truncated chemical shift Hamiltonian for a single spin is:

$$\hat{H}_{CS} = -\omega_0 \delta_{zz}^{LF} \hat{I}_z = -\gamma \hat{I}_z \delta_{zz}^{LF} B_0 \quad [2.9]$$

It leads to a slow precession of the magnetization with a frequency:

$$\omega_{CS} = -\omega_0 \delta_{zz}^{LF} \quad [2.10]$$

where δ_{zz}^{LF} is the zz element of the chemical shift tensor expressed in the LF. The tensor δ consists of a symmetric and an antisymmetric part. The antisymmetric part can be ignored because it produces no contribution to the frequency in equation [2.10] [Schmidt-Rohr *et al.*, 1994]. The symmetric part is characterized most conveniently in the coordinate system in which it is diagonal (PAS):

$$\omega_{CS} = -\omega_0 \mathbf{b}_0^{\text{PAS}} \delta \mathbf{b}_0^{\text{PAS}} \quad [2.11]$$

with the unit vector $\mathbf{b}_0 = \frac{\mathbf{B}_0}{B_0}$ along the field direction.

With \mathbf{b}_0 expressed in terms of its polar coordinates (θ, Φ) in the PAS and δ_{xx}^{PAS} , δ_{yy}^{PAS} , and δ_{zz}^{PAS} denoting the principal values of the chemical shift tensor in the PAS, equation [2.11] can be written as:

$$\omega_{CS} = \omega_0 \left[\delta_{xx}^{\text{PAS}} (\cos \Phi \sin \theta)^2 + \delta_{yy}^{\text{PAS}} (\sin \Phi \sin \theta)^2 + \delta_{zz}^{\text{PAS}} (\cos \theta)^2 \right] \quad [2.12]$$

One defines:

$$\begin{aligned}
\delta_x &= \delta_{xx}^{PAS} - \delta_{iso} \\
\delta_y &= \delta_{yy}^{PAS} - \delta_{iso} \\
\delta_z &= \delta_{zz}^{PAS} - \delta_{iso}
\end{aligned}
\tag{2.13}$$

with the isotropic chemical shift:

$$\delta_{iso} = \frac{1}{3}(\delta_{xx}^{PAS} + \delta_{yy}^{PAS} + \delta_{zz}^{PAS})
\tag{2.14}$$

By convention:

$$|\delta_{zz}^{PAS} - \delta_{iso}| > |\delta_{xx}^{PAS} - \delta_{iso}| > |\delta_{yy}^{PAS} - \delta_{iso}|
\tag{2.15}$$

The chemical shift anisotropy can be described by the anisotropy parameter, $\Delta\sigma$:

$$\Delta\sigma = \frac{1}{2}(\delta_{xx}^{PAS} + \delta_{yy}^{PAS}) - \delta_{zz}^{PAS}
\tag{2.16}$$

and the asymmetry parameter, η :

$$\eta = \frac{3}{2} \frac{\delta_{xx}^{PAS} - \delta_{yy}^{PAS}}{\Delta\sigma}
\tag{2.17}$$

The chemical shift Hamiltonian in terms of $\Delta\sigma$, η , θ , Φ , and using equation [2.12] and [2.13] is, therefore:

$$\hat{H}_{CS} = \left\{ \delta_{iso} - \frac{1}{3} \Delta\sigma [3 \cos^2 \theta - 1 - \eta \sin^2 \theta \cos(2\Phi)] \right\} \gamma B_0 \hat{I}_z
\tag{2.18}$$

2.1.3 Dipole-Dipole Interaction

A nuclear spin will also experience a local field due to the presence of neighbouring spins. The magnitude of this local field will depend on the distance between the nuclear spins and the direction of the internuclear vector with respect to the magnetic field direction.

The homonuclear dipolar coupling between two like spins \mathbf{I}_i and \mathbf{I}_j can be described as:

$$\hat{H}_D^{\text{II}} = \hat{\mathbf{I}}_i \mathbf{D}_{ij} \hat{\mathbf{I}}_j = \frac{\mu_0 \gamma_i \gamma_j \hbar}{4\pi r_{ij}^3} \left[\mathbf{I}_i \mathbf{I}_j - \frac{3}{r_{ij}^2} (\mathbf{I}_i \mathbf{r}_{ij})(\mathbf{I}_j \mathbf{r}_{ij}) \right] \quad [2.19]$$

\mathbf{D}_{ij} is the traceless symmetric coupling tensor, μ_0 the permeability of vacuum, \hbar the Planck constant divided by 2π , and r_{ij} the distance from i nucleus to j nucleus.

After truncation:

$$\hat{H}_D^{\text{II}} = \frac{\mu_0 \gamma_I^2 \hbar}{4\pi r_{ij}^3} \frac{1}{2} (1 - 3 \cos^2 \theta) (3 \hat{I}_{iz} \hat{I}_{jz} - \mathbf{I}_i \mathbf{I}_j) \quad [2.20]$$

$$\hat{H}_D^{\text{II}} = \frac{\mu_0 \gamma_I^2 \hbar}{4\pi r_{ij}^3} \frac{1}{2} (1 - 3 \cos^2 \theta) \left[2 \hat{I}_{iz} \hat{I}_{jz} - \frac{1}{2} (\hat{I}_1^+ \hat{I}_2^- + \hat{I}_1^- \hat{I}_2^+) \right] \quad [2.21]$$

where the raising operator, \hat{I}^+ , and the lowering operator, \hat{I}^- , are defined as:

$$\hat{I}^+ = \hat{I}_x + i \hat{I}_y \quad \hat{I}^- = \hat{I}_x - i \hat{I}_y \quad [2.22]$$

The homonuclear dipolar coupling constant, d_{II} , is defined as:

$$d_{\text{II}} = \frac{\mu_0 \gamma_I^2 \hbar}{4\pi r_{ij}^3} \quad [2.23]$$

Heteronuclear dipolar coupling of two different types of nuclei, I and S, is described by the Hamiltonian:

$$\hat{H}_D^{\text{IS}} = \hat{\mathbf{I}} \mathbf{D}_{\text{IS}} \hat{\mathbf{S}} \quad [2.24]$$

The truncated Hamiltonian of the heteronuclear dipolar couplings is given by:

$$\hat{H}_D^{IS} = \frac{\mu_0}{4\pi} \frac{\gamma_I \gamma_S \hbar}{r_{IS}^3} \frac{1}{2} (1 - 3 \cos^2 \theta) 2 \hat{I}_z \hat{S}_z \quad [2.25]$$

where \hat{S}_z is the z component of the \hat{S} spin angular momentum operator.

The heteronuclear dipolar coupling constant, d_{IS} , is defined as:

$$d_{IS} = \frac{\mu_0}{4\pi} \frac{\gamma_I \gamma_S \hbar}{r_{IS}^3} \quad [2.26]$$

2.1.4 Indirect Spin-Spin Interaction

The indirect spin-spin or J -coupling is of great importance in solution NMR. In solid-state NMR it can often be neglected. ^{31}P - ^{31}P J -couplings are usually smaller than one hundred Hz and are usually hidden under the dominating dipolar effects. Nevertheless, using certain pulse schemes the indirect spin-spin coupling can be observed. Unlike the chemical shift, the J -coupling is independent of the applied magnetic field.

The Hamiltonian of the indirect spin-spin coupling has the form:

$$\hat{H}_J = \gamma_i \gamma_j \sum_{i < j} \hat{\mathbf{I}}_i J_{ij} \hat{\mathbf{I}}_j \quad [2.27]$$

where J_{ij} is the spin-spin coupling tensor.

$$J_{ij} = J_{ij}^{iso} + J_{ij}^{aniso} \quad [2.28]$$

leading to

$$\hat{H}_J^{iso} = \gamma_i \gamma_j \sum_{i < j} J_{ij}^{iso} \hat{\mathbf{I}}_i \hat{\mathbf{I}}_j \quad [2.29]$$

and

$$\hat{H}_J^{aniso} = \gamma_i \gamma_j \sum_{i < j} \hat{\mathbf{I}}_i J_{ij}^{aniso} \hat{\mathbf{I}}_j \quad [2.30]$$

The term J_{ij}^{iso} is called the isotropic J -coupling, or the scalar coupling. The term scalar indicates that \hat{H}_J^{iso} is independent of molecular orientation. It should be noted that J_{ij}^{aniso} , the anisotropic J -coupling, is usually small and is often ignored. In any case it is very difficult to distinguish it from the direct dipolar coupling.

2.2. High Resolution NMR Techniques for Solid-State

The anisotropy of the chemical shift interaction and the dipolar coupling to many nuclei will, in general, cause broad resonance lines in solids. This results in spectral overlap and usually obscures chemical shift information. These problems can be overcome by manipulating the Hamiltonian in such way that the time average results in narrow lines. Three important techniques of high-resolution solid-state NMR, namely magic angle spinning (MAS), cross-polarization (CP), and heteronuclear dipolar decoupling are used throughout this thesis.

2.2.1 Magic Angle Spinning

The sensitivity and resolution of NMR spectra of solid samples may be improved significantly by magic angle spinning (MAS), i.e. rapid rotation of the sample about an axis tilted by the “magic angle” of $\theta_m = \arccos\left(\sqrt{\frac{1}{3}}\right) = 54.74^\circ$ with respect to the \mathbf{B}_0 field.

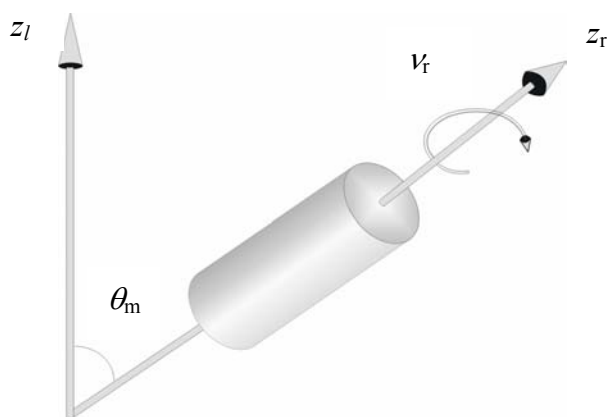


Figure 2. 1 Magic angle spinning of a rotor with the spinning frequency ν_r . A rotor reference frame (RRF) is defined such that the z_r axis coincides with the rotation axis.

The spatial rotation of the sample causes the orientation dependent anisotropic spin interactions, such as the chemical shift anisotropies and dipole-dipole interaction, to become time dependent and to be average out if the rotation frequency exceeds the largest coupling of the spin species considered.

The observed NMR signal:

$$f(t) = \exp(i\omega t) \quad [2.31]$$

subject to sample rotation acquires a time dependence $\omega(t)$. The signal must therefore be written:

$$f(t) = \exp\left[i \int_0^t \omega(t') dt'\right] \quad [2.32]$$

The rotation can be described conveniently in the rotor reference frame (RRF) where:

$$\omega(t) = \mathbf{b}_0^{\text{RRF}} \delta^{\text{RRF}} \mathbf{b}_0^{\text{RRF}} \gamma \mathbf{B}_0 \quad [2.33]$$

and $\mathbf{b}_0^{\text{RRF}}$ is the \mathbf{B}_0 direction in RRF.

In terms of Euler angles (α , β , γ) which characterize the relative orientation of PAS and RRF, the frequency formula [2.33] can be written as:

$$\omega(t) = C_1 \cos(\gamma + \omega_r t) + C_1 \cos(2\gamma + 2\omega_r t) + S_1 \sin(\gamma + \omega_r t) + S_2 \sin(2\gamma + 2\omega_r t) \quad [2.34]$$

where $\omega_r/(2\pi)$ is the spinning sample rate.

The C and S coefficients which depend on $\Delta\sigma$, η , α , and β are:

$$\begin{aligned} C_1(\alpha, \beta) &= \Delta\sigma \sqrt{2} \frac{1}{3} \sin 2\beta \left(1 + \frac{1}{3} \eta \cos 2\alpha\right) \\ C_2(\alpha, \beta) &= -\Delta\sigma \left[\frac{1}{3} \sin^2 \beta - \frac{1}{9} \eta (1 + \cos^2 \beta) \cos 2\alpha \right] \\ S_1(\alpha, \beta) &= -\Delta\sigma \eta \frac{2}{9} \sqrt{2} \sin \beta \sin 2\alpha \\ S_2(\alpha, \beta) &= -\Delta\sigma \eta \frac{2}{9} \cos \beta \sin 2\alpha \end{aligned} \quad [2.35]$$

For a single crystallite, the MAS signal is given by:

$$g(t) = \exp\left[i \int_0^t \omega(t') dt'\right] = \exp\{i[\phi(t) - \phi(0)]\} = \exp[i\phi(t)] \exp[-i\phi(0)] \quad [2.36]$$

The phase angle:

$$\phi(\alpha, \beta, \gamma + \omega_r t) = \int \omega(\alpha, \beta, \gamma + \omega_r t) dt \quad [2.37]$$

$$\phi(\alpha, \beta, \gamma + \omega_r t) = \frac{1}{\omega_r} \left[C_1 \sin(\gamma + \omega_r t) + \frac{C_2}{2} \sin(2\gamma + 2\omega_r t) - S_1 \cos(\gamma + \omega_r t) - \frac{S_2}{2} \cos(\gamma + \omega_r t) \right] \quad [2.38]$$

The full expression for $g(t)$, combining equations [2.36] and [2.38] is:

$$g(t) = \exp\left[\left(-\frac{i}{\omega_r}\right) \left(C_1 \sin \gamma + \frac{C_2}{2} \sin 2\gamma - S_1 \cos \gamma - \frac{S_2}{2} \cos \gamma \right)\right] \exp\left\{\left(\frac{i}{\omega_r}\right) \left[C_1 \sin(\gamma + \omega_r t) + \frac{C_2}{2} \sin(2\gamma + 2\omega_r t) - S_1 \cos(\gamma + \omega_r t) - \frac{S_2}{2} \cos(\gamma + \omega_r t) \right]\right\} \quad [2.39]$$

Defining a function:

$$f(\alpha, \beta, \gamma + \omega_r t) = \exp[i\phi(\alpha, \beta, \gamma + \omega_r t)] \quad [2.40]$$

one can express the time signal as:

$$g(t) = f^*(\alpha, \beta, \gamma + \omega_r t) f(\alpha, \beta, \gamma + \omega_r t) \quad [2.41]$$

As the signal is periodic with $t_r = \frac{2\pi}{\omega_r}$ according to the harmonic time dependences in equation [2.39], intensity can only appear at ω_r and its harmonics $N\omega_r$ in the Fourier transform. Figure 2.2 represents the simulated spectra of a powder showing the effect of MAS on the lineshape due to CSA of an $I = \frac{1}{2}$ spin nucleus.

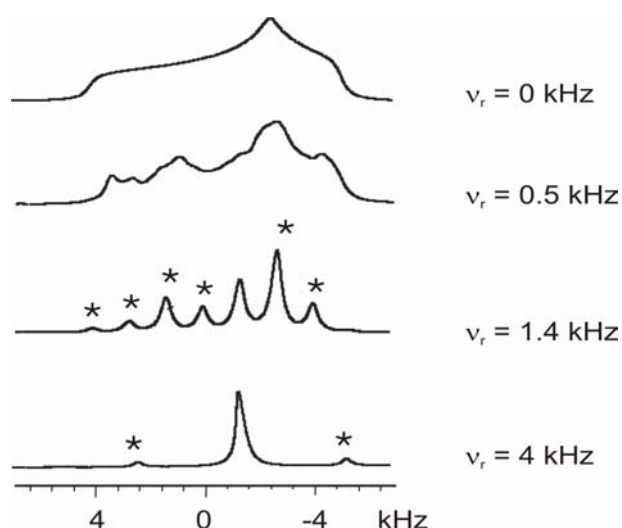


Figure 2. 2. The effect of MAS on the anisotropic linewidth due to CSA. Upon rotating sample, the static lineshape is seen to break up into a central line and spinning sidebands, separated by the rotor frequency. Spinning side bands are marked with asterisks.

2.2.2 Cross-polarization

For solid-state NMR of dilute spins (S), MAS is usually combined with the method of cross-polarization (CP). A sensitivity enhancement is obtained as a consequence of the transfer of polarization from an abundant nucleus (I) with a high gyromagnetic ratio, usually ^1H via a mutual flip-flop to the dilute spins (S). The approach is referred to as CP MAS NMR. Figure 2.3 shows the pulse sequence for the cross-polarization scheme followed by proton decoupling.

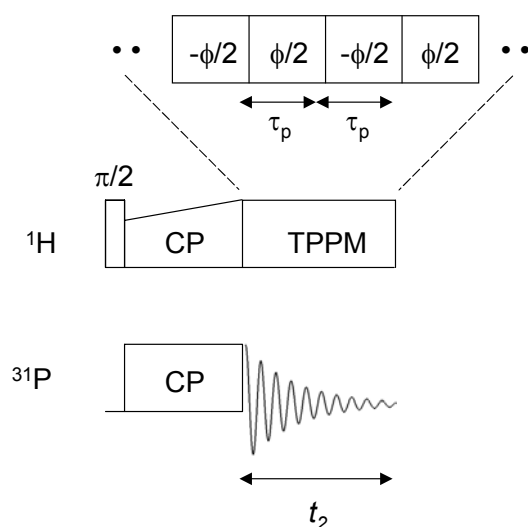


Figure 2.3 Pulse sequence for the CP MAS experiment with phase modulated TPPM decoupling on the ^1H channel during the acquisition of the ^{31}P FID.

In a heteronuclear CP experiment, the two spins, I and S (^{31}P in our case), are prepared with different polarizations. The flip-flop process can then equilibrate the I and S spin polarization. Hartmann and Hahn showed that energy balance could be maintained by the

irradiation of two r.f. fields with frequencies equal to the Zeeman frequencies of the I and S spins. The precession frequencies of the I and S spins in their respective rotating frames are given by:

$$\begin{aligned}\omega_{1I} &= \gamma_I B_{1I} \\ \omega_{1S} &= \gamma_S B_{1S}\end{aligned}\quad [2.42]$$

By adjusting the ratio $\frac{B_{1I}}{B_{1S}}$, the rotating frame Zeeman splitting of the I and S spins can be matched. This is known as Hartmann-Hahn condition:

$$\gamma_I B_{1I} = \gamma_S B_{1S}\quad [2.43]$$

When the spinning frequency exceeds both I-I and I-S dipolar interactions, the single Hartmann-Hahn condition splits into a series of new sideband matching condition:

$$\Delta = \omega_{1I} - \omega_{1S} = n\omega_r\quad [2.44]$$

where $\omega_r/2\pi$ is the sample spinning rate. An efficient CP is obtained only at the first and second-order sidebands ($n = \pm 1, \pm 2$).

The CP technique results in an enhancement of the magnetization of the S spins. The enhancement is proportional to the ratio of the two gyromagnetic ratios, $\frac{\gamma_I}{\gamma_S}$. The dynamics of a CP experiment can be treated by considering the I and S spins as thermodynamic reservoirs, for which a spin temperature is defined. According to Curie's law, the observable magnetization is proportional to the inverse temperature β . The I spin reservoir initially has a high inverse spin temperature, β_I , since the I spins are polarized. The initial S spin inverse temperature, β_S , is zero. Both reservoirs will lose energy to the lattice via rotating frame spin-lattice relaxation, characterized by spin-lattice relaxation rates $T_{1I\rho}^{-1}$ and $T_{1S\rho}^{-1}$. If the I and S spins are brought into contact, both reservoirs will approach the equilibrium with a rate constant T_{IS}^{-1} . Due to the many body character of the abundant I spin reservoir, fast I-I spin flip-flops will maintain a uniform spin temperature. Therefore, magnetization transfer is generally irreversible and non-oscillatory. However, a cross-polarization echo can be

generated whereby the polarization transferred to the S spins returns to the I spins [Ernst *et al.*, 1998]. The appearance of the echo indicates that cross-polarization is a deterministic unitary process that conserves quantum statistical entropy in contrast to the standard thermodynamic model in which entropy always increases. Therefore, the thermodynamic model should be applied with care even in the samples where the build-up and the decay of the magnetization can be approximated by multiexponential processes. In the thermodynamic description, the rate constant T_{IS}^{-1} is proportional to the I-S flip-flop probability and, therefore, to the sixth power of the inverse distance between I and S. T_{IS} can thus provide information on the proximity of I and S spins and can be determined by observing the S spin magnetization as a function of mixing time, i.e. the time for which the I and S reservoirs are brought into contact. The CP build-up curve is given by the following equation:

$$\beta_s(t) = \frac{1}{1-\lambda} \left\{ 1 - \exp\left[-\frac{(1-\lambda)t}{T_{IS}}\right] \right\} \left[\exp\left(-\frac{t}{T_{1\rho}}\right) \right] \beta_I(0)$$

$$\beta_I(t) = \left[\exp\left(-\frac{t}{T_{1\rho}}\right) \right] \beta_I(0)$$
[2.45]

where $\lambda = \frac{T_{IS}}{T_{1\rho}}$.

Equation [2.45] describe the case of extremely diluted S spins, with matched Hartmann-Hahn condition and with short $T_{1\rho}$ relaxation time.

2.2.3 Heteronuclear Dipolar Decoupling

Using the average Hamiltonian theory, the zeroth order Hamiltonian for two spins, I and S, under continuous wave (cw) decoupling is:

$$\overline{\hat{H}}^{(0)} = \omega_{CS}^S \hat{S}_z$$
[2.46]

and the first order average Hamiltonian:

$$\overline{\hat{H}}^{(1)} = \frac{(\omega_D^{IS})^2 + (\omega_{CS}^I)^2}{2\omega_1} \hat{I}_x + \frac{\omega_D^{IS} \omega_{CS}^I}{\omega_1} 2\hat{I}_x \hat{S}_z \quad [2.47]$$

ω_{CS}^S and ω_{CS}^I are defined as in equation [2.10] and ω_D^{IS} is the heteronuclear dipolar frequency. The first term in [2.47] commutes with the S spin subspace of the density operator and has no influence on the time evolution of the S spin. The second term, a cross term between the chemical shift tensor and the heteronuclear dipolar coupling tensor describing the second order recoupling between these tensors is the dominating term for isolated spin pairs. The flip-flop terms of the homonuclear dipolar coupling Hamiltonian lead to an additional modulation of the heteronuclear dipolar coupling which results in a broadening of the lines of the decoupled heteronuclear spin. If the decoupling field, ω_1 , is applied off resonance ($\Delta\omega \neq 0$; where $\Delta\omega = \omega_0 - \omega_{ref}$) the Hamiltonian in the tilted rotating frame is:

$$\hat{H} = -\omega_e \hat{I}_z + d_{IS} \hat{S}_z (\hat{I}_z \cos \theta - \hat{I}_x \sin \theta) \quad [2.48]$$

where:

$$\omega_e = \sqrt{\omega_1^2 + \Delta\omega} \quad [2.49]$$

$$\cos \theta = \frac{\Delta\omega}{\omega_e} \quad [2.50]$$

The effective homonuclear dipolar coupling does not appear in equation [2.48] since it vanishes at the magic angle. Nevertheless it leads to a broadening of the line of the decoupled heteronuclear spin because the second order recoupling is no longer quenched by the homonuclear spin flip-flop terms.

Going into a frame defined by $-\omega_e \hat{I}_z$ and using the average Hamiltonian theory, the average Hamiltonian of the IS coupling term to second order is given by:

$$\overline{\hat{H}}_{IS}^{(0)} = d_{IS} \cos \theta \hat{S}_z \hat{I}_z \quad [2.51]$$

$$\overline{\hat{H}}_{IS}^{(1)} = d_{IS}^2 \sin^2 \theta \frac{\hat{S}_z^2}{\omega_e} \left(\cos \theta \hat{I}_x - \frac{1}{2} \sin \theta \hat{I}_z \right) \quad [2.52]$$

$$\overline{\hat{H}}_{IS}^{(2)} = -\frac{d_{IS}^3}{2\omega_1^2} \hat{S}_z^3 \hat{I}_x \quad [2.53]$$

The first order average Hamiltonian, $\overline{\hat{H}}_{IS}^{(1)}$, commutes with the spin vector $\hat{\mathbf{S}}$, so only $\hat{H}_{IS}^{(0)}$ and $\overline{\hat{H}}_{IS}^{(2)}$ are relevant.

Off resonance, where $\Delta\omega \neq 0$, the decoupling efficiency, δ_S (roughly the relative S linewidth), goes as:

$$\delta_S \sim \cos\theta \quad [2.54]$$

On resonance, the dominant term is $\overline{\hat{H}}_{IS}^{(2)}$, and we expect:

$$\delta_S \sim \left(\frac{d_{IS}}{\omega_1}\right)^2 \quad [2.55]$$

i.e., the decoupling efficiency should increase (the S linewidth should decrease) inverse quadratically with ω_1 ($\delta_S \sim \frac{1}{\omega_1^2}$) for large ω_1 .

To remove all odd orders of the average Hamiltonian, therefore the second order recoupling term (see eq. [2.47]), symmetric pulse sequences can be employed. Two pulse phase modulated (TPPM) decoupling scheme consisting of pulses with flip angles β (usually around 180°) and alternating phases of $\pm\varphi$ ($\varphi = 15^\circ$) was used throughout this thesis. The zeroth order and first order average Hamiltonians are:

$$\overline{\hat{H}}^{(0)} = \omega_{CS}^S \hat{S}_z \quad [2.56]$$

$$\overline{\hat{H}}^{(1)} = \frac{2 \tan \varphi}{\pi} \left[\frac{(\omega_D^{IS})^2 + (\omega_{CS}^I)^2}{2\omega_1} \hat{I}_x + \frac{\omega_D^{IS} \omega_{CS}^I}{\omega_1} 2\hat{I}_x \hat{S}_z \right] \quad [2.57]$$

Comparing equation [2.57] with the result for cw decoupling [2.47] one realises that the residual second order coupling obtained under TPPM is $\frac{2 \tan \varphi}{\pi}$ smaller than for cw

decoupling. For $\varphi = 15^\circ$ this is a reduction of almost a factor of 6 (5.859) for the second order recoupling contribution to the line broadening.

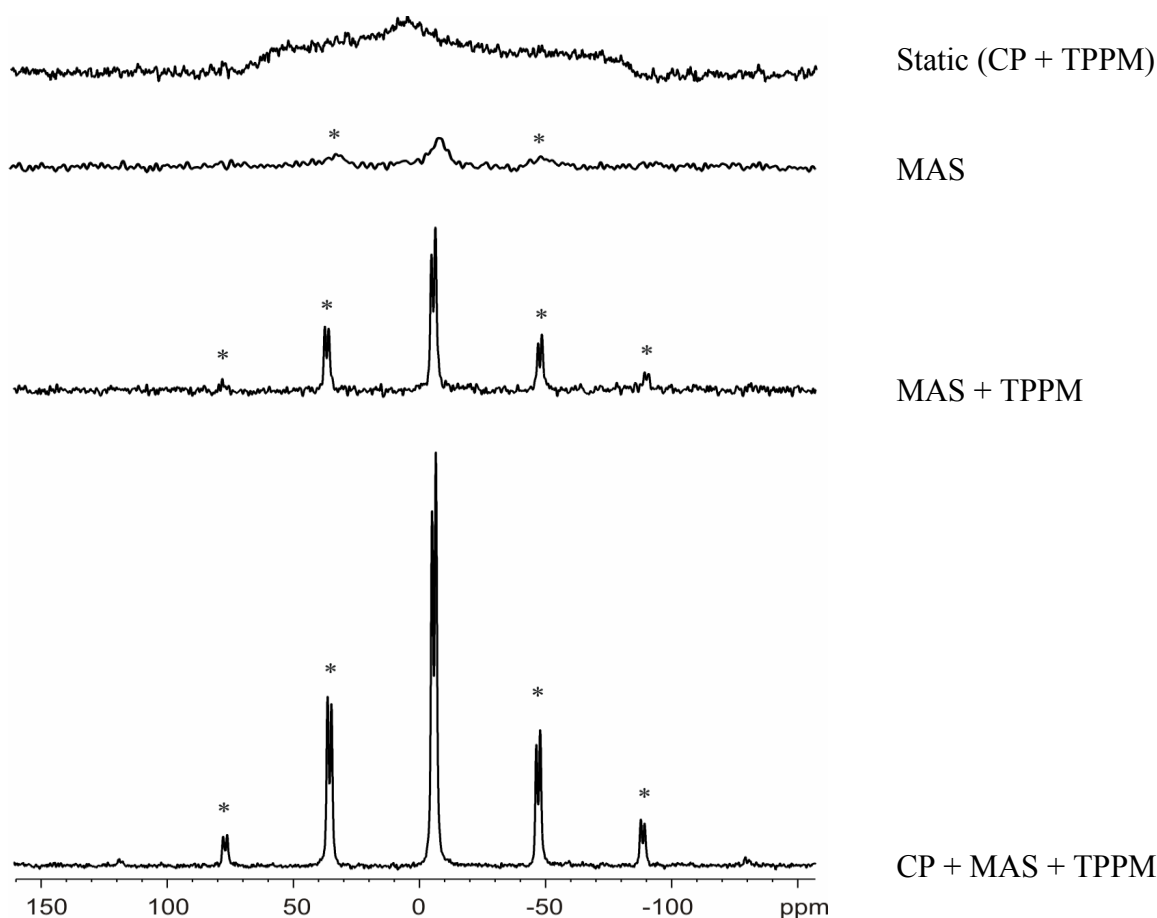


Figure 2.4 Experimental spectra of O-phospho-L-tyrosine. From top to bottom: static spectrum + CP + TPPM heteronuclear decoupling; MAS (no CP, no heteronuclear decoupling); MAS + TPPM heteronuclear decoupling; MAS + CP + TPPM heteronuclear decoupling ($\omega_r/(2\pi) = 5$ kHz, 16 scans).

Figure 2.4 shows the sensitivity and resolution of the ^{31}P NMR signal of O-phospho-L-tyrosine obtained by combining cross-polarization with magic angle spinning and heteronuclear decoupling techniques.

The NMR spectroscopic parameters of several unprotonated phosphates in inorganic materials are known [Hartmann *et al.*, 1994]. The phosphate structures may be characterized by the use of the Q^n group classification. The Q^n groups are basic structural units ($[\text{PO}_4]$ tetrahedra), where n is the number of other units attached to the unit in question. Different Q^n groups have different values for the ^{31}P chemical shift anisotropy [Grimmer, 1983; Duncan *et al.*, 1984; Un *et al.*, 1989; Grimmer *et al.*, 1997] (Table 2.1). The monophosphate groups (Q^0) typically possess smaller absolute values of the chemical shift anisotropy than other

polyphosphate groups. The chemical shift anisotropies of diphosphates, Q^1 , are always positive. The absolute values of the anisotropy parameters of ultraphosphates (Q^3) strongly exceeds the values for the other phosphate groups.

	δ_{iso} / ppm	$\Delta\sigma$ / ppm	η
monophosphates	-30 to 12	-60 to -8	0 to 1
diphosphates	-33 to 4	45 to 106	0.8 to 1
polyphosphates	-53 to -18	-214 to -106	0.3 to 0.8

Table 2.1 Typical ranges for ^{31}P NMR spectroscopic parameters in unprotonated phosphates. The following convention was used: $\delta_{iso} = 1/3(\delta_{xx} + \delta_{yy} + \delta_{zz})$, $\Delta\sigma = 1/2(\delta_{xx} + \delta_{yy}) - \delta_{zz}$, $\eta = 3/2 (\delta_{xx} - \delta_{yy})/\Delta\sigma$, $|\delta_{zz} - \delta_{iso}| > |\delta_{xx} - \delta_{iso}| > |\delta_{yy} - \delta_{iso}|$. Here, δ_{zz} , δ_{yy} , and δ_{xx} denote the principal values of the chemical shift tensor.

Protonated phosphates (phosphates with P-OH or hydrogen bonds) deviate significantly from the ^{31}P chemical shift anisotropy values of the unprotonated phosphates.

The chemical shift anisotropies of the monohydrogen monophosphates, $Q^0(\text{H}^1)$, range from 60 to 96 ppm [Hartmann *et al.*, 1994]. These values do not fall into the range of Q^0 groups but into the range characteristic for Q^1 groups. $Q^0(\text{H}^1)$ groups possess P- O_T bonds (O_T , terminating oxygen atom) and P-OH bonds. The average bond length $r_{\text{P-O}}$ of P-OH bonds is clearly larger than that of P- O_T bonds. However, the bond length of P-OH bonds are comparable to those of P-O-P bridging bonds in diphosphates and polyphosphates [Hartmann *et al.*, 1994]. Grimmer [1978] developed a relationship between the chemical shift anisotropy and the P-O bond length as follows:

$$\Delta\sigma / \text{ppm} = A \left(r_{\text{P-O}} / \text{\AA} \right) + B \quad [2.58]$$

where A and B were determined empirically. Equation [2.58] has as its basis the idea that a decrease in bond length indicates a higher π -bond order [van Wazer, 1956], and that increased π -bonding leads to an increase in the chemical shift anisotropy. Due to the correlation between chemical shift anisotropies and the π -bond in equation [2.58] it is obvious that the chemical shift anisotropies were caused by similar π -bonding states of the $Q^0(\text{H}^1)$ groups and of the Q^1 groups. The asymmetry parameters of the monohydrogen monophosphates exhibit value from 0.3 to 0.9.

The ^{31}P chemical shift anisotropies of dihydrogen monophosphates, $\text{Q}^0(\text{H}^2)$, range from -117 to -86 ppm and from -106 to -72 ppm while the asymmetry parameters from 0.2 to 1 [Hartmann *et al.*, 1994]. The isotropic chemical shifts of the dihydrogen- and monohydrogen monophosphates are smaller than the isotropic chemical shifts of unprotonated monophosphates.

The ^{31}P chemical shift anisotropies of dihydrogen diphosphates, $\text{Q}^1(\text{H}^1)$, vary from -180 to -83 ppm. The chemical shift anisotropies of the $\text{Q}^1(\text{H}^1)$ groups and Q^1 groups differ in sign and amount. Furthermore, the chemical shift anisotropies observed for $\text{Q}^1(\text{H}^1)$ groups are within the range of values typical for Q^2 groups. The asymmetry parameters for these groups range from 0 to 0.2. The isotropic shifts of the dihydrogen diphosphates agree well with those of the corresponding unprotonated diphosphates [Hartmann *et al.*, 1994].

Several authors have tried to create a unified theoretical foundation for ^{31}P isotropic chemical shifts in all classes of phosphorus compounds [Muller *et al.*, 1956; Parks, 1957]. According to Letcher *et al.* [1966], the ^{31}P isotropic chemical shift, δ (referenced to 85 % phosphoric acid):

$$\delta = -C\Delta\chi_x + k\Delta n_\pi + A\Delta\theta \quad [2.59]$$

is dominated by three terms affected by structural variations, where $\Delta\chi_x$ is the electronegativity in the P-X bond, Δn_π the change in the π -electron overlap, $\Delta\theta$ the change in the P-X-P σ -bond angle, and C, k, and A are constants. For phosphorylated compounds Letcher and van Wazer [1966] conclude that changes in the σ -bond angles make a negligible contribution to the ^{31}P isotropic chemical shift while electronegativity effects predominate. Gorenstein [1977] demonstrates for a large number of systems that the decrease in the P-O-P bond angle in the PO_4 tetrahedra leads to downfield ^{31}P isotropic chemical shifts. This observation was associated with changes in hybridisation resulting from the bond angle changes [Gorenstein, 1975].

The use of ^{31}P solid-state NMR to organic phosphates is limited by the relatively poor resolution of the spectra. Better sensitivity and resolution are achieved by employing different solid-state NMR methods (MAS, CP, heteronuclear decoupling). Table 2.2 summarizes ^{31}P chemical shift anisotropies and asymmetry parameter of several biological compounds.

First solid-state ^{31}P NMR spectroscopic studies of the Ras protein were carried out recently in order to clarify the discrepancies between the results of X-ray diffraction studies on crystalline proteins and liquid-state ^{31}P NMR measurements [Stumber *et al.*, 2002].

Surprisingly, the resolution of the solid-state ^{31}P NMR spectra is comparable with the liquid-state ^{31}P NMR spectra. The signal-to-noise ratio of the solid-state ^{31}P NMR spectra even exceeds that of the liquid-state ^{31}P NMR spectra measured with the same amount of sample within the same measurement time.

	$\Delta\sigma$ / ppm	η	ref.
NaDNA	147	0.65	van Dam <i>et al.</i> , 2000
LiDNA	139	0.64	Song <i>et al.</i> , 1997
B and C forms of DNA	160	n.m.	Odahara <i>et al.</i> , 1994
Dipalmitoylphosphatylcholin	-163	0.8	Griffin <i>et al.</i> , 1978
Urea-phosphoric acid	-60	n.m.	Herzfeld <i>et al.</i> , 1978
Filamentous bacteriophage	163	n.m.	DiVerdi <i>et al.</i> , 1981
CL, DOPC, DOPE	-140	0	Pinheiro <i>et al.</i> , 1994

Table 2.2 NMR spectroscopic parameters of some crystalline biological compounds. CL = cardiolipin, DOPC = dioleoylphosphatidylcholine, DOPE = dioleoylphosphatidylethanolamine. The following convention was used: $\delta_{\text{iso}} = 1/3(\delta_{\text{xx}} + \delta_{\text{yy}} + \delta_{\text{zz}})$, $\Delta\sigma = 1/2(\delta_{\text{xx}} + \delta_{\text{yy}} - \delta_{\text{zz}})$, $\eta = 3/2 (\delta_{\text{xx}} - \delta_{\text{yy}})/\Delta\sigma$, $|\delta_{\text{zz}} - \delta_{\text{iso}}| > |\delta_{\text{xx}} - \delta_{\text{iso}}| > |\delta_{\text{yy}} - \delta_{\text{iso}}|$. Here, δ_{zz} , δ_{yy} , and δ_{xx} denote the principal values of the chemical shift tensor. n.m. indicates that the corresponding values could not be measured.

The resolution of liquid-state ^{31}P NMR spectra of proteins is determined by the transverse relaxation rate, R_2 , which can be written as:

$$R_2 = R_2^{\text{CSA}} + R_2^{\text{DD}} \quad [2.60]$$

where R_2^{CSA} and R_2^{DD} denote the contributions due to the ^{31}P chemical shift anisotropy and ^{31}P - ^1H heteronuclear magnetic dipole-dipole interaction, respectively. Other contributions such as J -coupling or homonuclear ^{31}P - ^{31}P magnetic dipole-dipole interaction can be neglected. For proteins of a molecular weight, M , exceeding 10 kDa dissolved in water at room temperature, the correlation time, τ_C , for molecular reorientation is higher than 5 ns. At external magnetic fields, B_0 , exceeding 10 T, the product of the ^{31}P Larmor frequency, ω_I , and τ_C fulfills the condition $(\omega_I\tau_C)^2 \gg 1$ and the two contributions to the relaxation rates can be written as:

$$R_2^{\text{CSA}} = \frac{4}{45} (\omega_I \Delta\sigma)^2 \left(1 + \frac{1}{3} \eta^2 \right) \tau_C \quad [2.61]$$

$$R_2^{DD} = \frac{1}{5} \left(\frac{\mu_0}{4\pi} \right)^2 \gamma_I^2 \gamma_S^2 \hbar^2 r^{-6} \tau_C \quad [2.62]$$

For $\Delta\sigma = 150$ ppm and $\eta = 0.5$, the average values observed for the ^{31}P NMR signals of Ras(wt)·Mg²⁺·GppCH₂p ($M = 19$ kDa) and at a ^{31}P resonance frequency of 202.46 MHz ($B_0 = 11.74$ T), a CSA relaxation rate R_2^{CSA} of 31 s⁻¹ is estimated according to equation [2.61]. Assuming a distance of 0.2 nm between ^{31}P and its next nearest ^1H neighbour (^{31}P -O- ^1H), a dipolar relaxation rate R_2^{DD} of 2.5 s⁻¹ is expected. Obviously, relaxation due to chemical shift anisotropy is the leading term in equation [2.60]. Therefore, the resolution of liquid-state ^{31}P NMR spectra of proteins decreases at increasing field strengths. The resolution of ^{31}P MAS NMR spectra is determined by the residual linewidth, i.e. the full width at half maximum of the central line of the MAS spectrum. Chemical shift anisotropy and heteronuclear ^{31}P - ^1H magnetic dipole-dipole interaction are the dominating line broadening interactions (see above). Although both interactions are inhomogeneous, homonuclear magnetic dipole-dipole interaction among the ^1H nuclei, a homogeneous interaction, influences the residual linewidth. Therefore, efficient heteronuclear ^1H decoupling has to be applied in order to minimize this influence.

3 Materials and Methods

3.1 Materials

Bacterial strains:

/Escherichia Coli/ CK600K supE, hsdM⁺, hsdR⁻, kan^R; Hoffmann-Berling, Heidelberg

Standard:

Protein standard SDS7 (66/45/36/29/24/20, 1/14, 2kDa) Sigma, Deisenhofen

Chemicals:

Bacto tryptone	Becton Dickinson and Company, Le Pont de Claix, France
Bacto yeast extract	Becton Dickinson and Company, Le Pont de Claix, France
NaCl	Merck, Darmstadt
Ampicillin	GERBU, Biotechnik Gaiberg
Kanamycin	Haybad, UK
IPTG	GERBU, Biotechnik Gaiberg
Tris	Merck, Darmstadt
MgCl ₂	Merck, Darmstadt
CaCl ₂	Merck, Darmstadt
PEG 400	Amersham international, USA
PEG 1500	Fluka, Buchs, Switzerland
DTE	GERBU, Biotechnik Gaiberg
NaN ₃	Merck, Darmstadt
Alkaline phosphatase	Roche Diagnostic, Mannheim
DNase	Roche Diagnostic, Mannheim
Lysozym	Merck, Darmstadt
GDP	Aldrich, Steinheim
GppNHp	Aldrich, Steinheim
GTPγS	Aldrich, Steinheim
GppCH ₂ p	Aldrich, Steinheim
Adamantane	Jansen Chimica, Beerse, Belgium

Glycine	Merck, Darmstadt
Pb(NO ₃) ₂	Merck, Darmstadt
O-Phospho-L-Serine	Sigma, Steinheim
O-Phospho-L-Threonine	Sigma, Steinheim
O-Phospho-L-Tyrosine	Sigma, Steinheim
NaH ₂ PO ₄ ·H ₂ O	Merck, Darmstadt

3.2 Preparation of Protein Samples

3.2.1 Ras expression, Purification, and Exchange of Nucleotide

Wild-type and mutants of truncated human Ras (residues 1-166) were expressed in *Escherichia coli* CK600K using a ptac vector and purified as described before by Tucker *et al.* [1986]. 10 l of Luria Bertani (LB: 10 g/l Bacto-Trypton, 5g/l Yeast extract, 10 g/l NaCl) medium together with 100 mg/l ampicillin and 25 mg/l kanamycin were incubated over night with 100 ml culture. The incubation took place at 310 K and 160 rpm in an INFORS AG shaker (Bottmingen, Switzerland). After an absorption value of 0.8 was reached (after 3-4 hours), the protein expression was induced by 1 mM IPTG. The culture was centrifuged at 1870 g (Beckman J-6B) after one day and the bacterial pellet was dissolved into 150 ml buffer (40 mM Tris/HCl pH 7.6, 0.5 mM EDTA, 0.1 M PMSF) and stored at 253 K. The cell dissociation in the defrozen bacterial suspension was initiated by adding 1 mg/ml Lysozym. After 30 minutes incubation at 277 K, 7 ml 6% sodium-deoxycholat were added. After another 30 minutes, 2 ml 1 M MgCl₂ and 20 mg DNase were given to the cell suspension and incubated at 277 K for further 30 minutes. Because many cells require some sort of mechanical disruption process to open them, sonication, i.e. breaking open cells through the use of ultrasonic waves, was also employed. Once the cells have been broken the crude lysate was centrifuged. After one hour centrifugation at 18500 g (JA 25.50 Beckman centrifugation system) the cell fragments were sedimented and the clear supernatant was given to a DEAE (diethylaminoethyl) ion exchange column (500 ml volume) after its equilibration with a C/2 buffer (64 mM Tris/HCl pH 7.6, 10 mM MgCl₂, 2 mM DTE). The column was washed again one time volume of the column with C/2 buffer. The proteins were then eluted from the column by passing a solution containing a gradually increasing concentration of salt onto the top of the column. A volume of 4 l salt gradient (0-300 mM NaCl in C/2 buffer) was used and

the proteins collected in the fractions eluted from the bottom of the column. 20 ml protein solution/fraction were collected. The fractions were analysed by sodium dodecyl sulfate-polyacrylamide gel electrophoresis (SDS-PAGE). The gel composed of the resolving gel mixture 15% (10 ml): 2.4 ml H₂O, 15 ml 30% acrylamide, 7.5 ml resolving-gel buffer (1.5 M Tris/Cl pH 8.8), 150 µl 20% SDS, 150 µl 20% ammoniumpersulfate (APS), 120 µl TEMED (tetramethylethylenediamine) and of the stacking gel mixture 5% (10 ml): 6.9 ml H₂O, 1.7 ml 30% acrylamide, 1.25 ml stacking gel buffer (1M Tris/Cl pH 6.8), 50 µl 20% SDS, 50 µl 20% APS, 10 µl TEMED was cast as a thin rectangular slab in which several protein samples treated with SDS could be simultaneously analysed in parallel lanes. The buffer, which is the same in both, reservoir and the gel, has a pH such that the molecules have net negative charges and migrate to the anode. A direct current of 80 A was passed through the gel for a sufficient time (40 minutes) to separate the molecular components into a series of discrete components. The proteins embedded gel was then removed from its holder and stained with Coomassie Blue Dye (90 ml methanol, 90 ml water, 20 ml acetic acid, 250 mg Coomassie Brilliant Blue). Upon staining, the proteins absorbed the pigment and appeared as a discrete band after destaining with: 70% water, 20% acetic acid, 10% ethanol (Figure 3. 1). A marker protein (SDS7) was run for comparison.

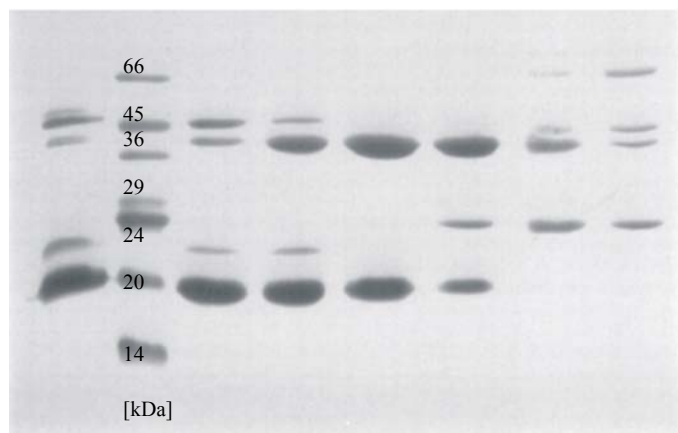


Figure 3.1 Photograph of the SDS polyacrylamide gel of Ras(T35A)·Mg²⁺·GDP. 20 µl protein from the 86th to the 110th fraction collected from a DEAE ion exchange column were run in parallel lanes. The second left lane contains the molecular weight standard (SDS7).

After gel electrophoresis, the Ras protein fractions (usually between the 86th and the 115th fraction) were collected and concentrated with an Amicon concentrator. The Ras protein was further purified using gel filtration chromatography. The column in this technique consists of beads of a hydrated, sponge like material containing pores that span a relatively narrow size range of molecular dimensions. Molecules with molecular masses ranging below the exclusion limit of a gel pore will elute from the gel in the order of the molecular masses, with the largest eluting first. A G75 Sephadex column (330 ml volume, Amersham Pharmacia, Freiburg) was equilibrated with buffer D (64 mM Tris/HCl pH 7.6, 400 mM NaCl, 10 mM

MgCl₂, 2 mM DTE, 0.1 mM GDP). By SDS-PAGE the fractions containing Ras were identified. Normally the Ras protein eluted after about 200 ml. The fractions were concentrated to a protein concentration of 23-40 mg/ml.

GDP, which binds very tightly to Ras was replaced by the slowly hydrolysing GTP analogue GppNHp, GTP γ S, GppCH₂p as shown by John *et al.* [1990]. 100-200 μ M Ras GDP were given in 50 mM Tris/HCl pH 7.6, 2 mM DTE, and 200 mM (NH₄)₂SO₄. The wanted analogue (two times excess in comparison with GDP) together with alkaline phosphatase (2 U/mg protein) were added. After one night incubation at 277 K, free nucleotide and phosphate were removed by gel filtration using Tris buffer (50 mM Tris/HCl pH 7.6, 10 mM MgCl₂, 2mM DTE). The Ras protein in complex with the different GTP analogues eluted from the column (122 ml volume, Superdex G75, Amersham Pharmacia, Freiburg) after about 60 ml. The final purity of the proteins was > 95% as judged from SDS-PAGE. The concentration and nature of protein-bound nucleotide was analysed with C18 reverse-phase high performance liquid chromatography (HPLC; the HPLC buffer: 100 mM K₂HPO₄/KH₂PO₄ pH 6.5, 10 mM tetrabutylammonium bromide, 7% acetonitrile) and determined with a calibrated detector and integrator (Beckman). The protein solution was sink in liquid nitrogen and stored at 193 K.

3.2.2 Ras Crystallization

Commercially available proteins are almost always offered as lyophilized powders. Although the proteins in a lyophilized powder might be properly folded, it is to be expected that the conformation of side chains will be quite variable. Each molecule will then have a slightly different shift for each chemically equivalent site because they are rendered magnetically inequivalent by this structural heterogeneity. Therefore, the linewidth for lyophilized proteins is usually not narrow enough to provide high resolution spectra by NMR spectroscopy. An alternative for the solid-state NMR spectroscopic studies is protein crystallization. Crystalline materials are also found to provide higher stability than the lyophilized samples. While X-ray crystallography requires large defect-free crystals, smaller crystals are just as useful in solid-state NMR as large crystals. Anyway, crystallization of large proteins is difficult, unpredictable, and not to be ventured by easily frustrated researchers.

For this thesis, crystals of Ras(wt)·Mg²⁺·GppNHp, Ras(T35S)·Mg²⁺·GppNHp, Ras(T35A)·Mg²⁺·GppNHp, Ras(wt)·Mg²⁺·GTP γ S, Ras(T35S)·Mg²⁺·GTP γ S,

Ras(T35A)·Mg²⁺·GTPγS, Ras(wt)·Mg²⁺·GppCH₂p, Ras(T35S)·Mg²⁺·GppCH₂p, Ras(T35A)·Mg²⁺·GppCH₂p were grown using the sitting drop method (3 Well Spot Plate, Hampton Research). The plates were sealed with a transparent tape and incubated in the dark at 291 K. A quantity of 20 to 40 mg protein was needed for acquiring NMR spectra of sufficient quality.

Crystallization of Ras(wt)·Mg²⁺·GppNHp

15 μl 50 mM Tris/HCl pH 7.6, 10 mM MgCl₂, 5 mM dithioerithriol, 56% polyethylene glycol 400 were given to 15 μl of 1.5 mM protein solution in each small cavity of the 3 well spot plate. Crystals growth time: 1-2 days.

Crystallization of Ras(wt)·Mg²⁺·GTPγS

15 μl 64 mM Tris/HCl pH 7.6, 10 mM MgCl₂, 1 mM dithioerithriol, 1 mM NaN₃, 40% polyethylene glycol 1500, and 3 μl of 0.1 M spermine were given to 15 μl of 1.8 mM protein solution. Crystals growth time: 5-6 days.

Crystallization of Ras(wt)·Mg²⁺·GppCH₂p

15 μl 64 mM Tris/HCl pH 7.6, 10 mM MgCl₂, 1 mM dithioerithriol, 1 mM NaN₃, 60% polyethylene glycol 1500 were given to 15 μl of 2 mM protein solution. Big crystals grew after 2-3 days. Smaller crystals of Ras(wt)·Mg²⁺·GppCH₂p were obtained in the same interval of time from 15 μl 64 mM Tris/HCl pH 7.6, 10 mM MgCl₂, 1 mM dithioerithriol, 1 mM NaN₃, 50% polyethylene glycol 400 mixed with 15 μl of 2 mM protein.

Crystallization of Ras(T35S)·Mg²⁺·GppNHp and Ras(T35A)·Mg²⁺·GppNHp

15 μl 100 mM Tris/HCl pH 7.6, 20 mM CaCl₂, 5 mM dithioerithriol, 25% polyethylene glycol 1500 were given to 15 μl of 2 mM protein solution together with 3 μl of 0.1 M spermine. Crystals growth time: 4-5 days.

Crystallization of Ras(T35S)·Mg²⁺·GTPγS and Ras(T35S)·Mg²⁺·Gpp CH₂p

15 μl in 64 mM Tris/HCl pH 7.6, 10 mM CaCl₂, 1 mM dithioerithriol, 1 mM NaN₃, 60% polyethylene glycol 1500, and 3 μl of 0.1 M spermine were given to 15 μl of 1.8 mM protein solution. Crystals growth time: 4-5 days.

Crystallization of $Ras(T35A) \cdot Mg^{2+} \cdot GTP\gamma S$ and $Ras(T35A) \cdot Mg^{2+} \cdot GppCH_2p$

15 μ l 64 mM Tris/HCl pH 7.6, 10 mM $CaCl_2$, 5 mM dithioerithriol, 60% polyethylene glycol 1500, and 3 μ l of 0.1 M spermine were given to 15 μ l of 2 mM protein solution. Crystals growth time for $Ras(T35A) \cdot Mg^{2+} \cdot GTP\gamma S$: 1 day. Crystals growth time for $Ras(T35A) \cdot Mg^{2+} \cdot GppCH_2p$: 2-3 days.

The resulting crystals were mixed with their mother liquor in the spot plates and collected in 2 ml safe-lock tubes (Eppendorf tubes). They were centrifuged at 13 rpm in a Biofuge pico (Heraeus Instruments) at 277 K. The crystals settled down at the bottom of the safe-lock tubes. The mother liquor was partially removed and the crystals were collected and deposited in a 2.5 mm rotor. The rotor filled with protein was stored in refrigerator at 277 K.

3.3 NMR Methods

3.3.1 EXSY (EXchange SpectroscopY) and 1H Spin Diffusion

Two dimensional (2D) NMR spectroscopy is a valuable method for the study of spin exchange processes such as those resulting from chemical exchange and spin diffusion. The pulse sequence for the 2D exchange NMR experiment in solution was developed by Jeener *et al.* [1979]. The analogous solid-state NMR experiment, introduced by Szeverenyi *et al.* [1982], is given in Figure 3.2.

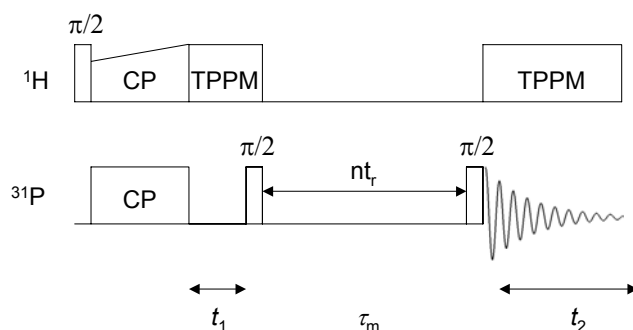


Figure 3.2 Pulse sequence for the 2D exchange experiment or proton driven spin diffusion.

First, transverse ^{31}P magnetization is created via cross-polarization resulting in spin locked ^{31}P magnetization in the xy -plane. Then, the spins are allowed to precess freely during the evolution time, t_1 . During this time, the dilute spins (^{31}P) are subjected to the Zeeman interaction under the influence of the ^{31}P chemical shift Hamiltonian, proton decoupling, and sample rotation about the magic angle. This evolution period, represented by the time interval t_1 , occurs under conditions in which the interaction Hamiltonian is identical to the Hamiltonian during the detection period, t_2 .

The mixing period is the interval which allows for exchange between the ^{31}P spins. One possibility is chemical exchange. A particular ^{31}P spin experiences a chemical shift change as the result of relocation into a new environment in the molecular or crystal framework. Another possibility is spin diffusion that may occur between adjacent spins. Spin diffusion is induced by the dipolar interaction of nuclear spins and leads to a transfer of magnetization between neighboring spins (i and j). Because of the $1/r_{ij}^6$ distance dependence of the spin diffusion rate [Schmidt-Rohr *et al.*, 2001], magnetization transfer is restricted to close nuclei. In principle, it is difficult to discriminate exchange resulting from conformational changes and from magnetization transfer mediated by ^{31}P - ^{31}P spin diffusion. The transition probability for ^{31}P spin diffusion processes, or more precisely between two ^{31}P nuclei with an isotropic chemical shift difference $\Delta\omega$, is given by:

$$P(t) = \frac{1}{2}[1 - \cos(\Delta\omega t)](\omega_D / \Delta\omega)^2 \quad [3.1]$$

where ω_D is the ^{31}P - ^{31}P coupling frequency. It is evident that the magnetization transfer (with proton decoupling) becomes inefficient if the ^{31}P - ^{31}P dipolar coupling is smaller than the difference $\Delta\omega$ of the resonance frequencies.

In perturbation theory the transition probability becomes:

$$P(t) = \frac{1}{2}\pi g_0^{\text{AB}} (\Delta\omega)\omega_D^2 t \quad [3.2]$$

where g_0^{AB} is the zero quantum lineshape which is determined by the ^1H - ^{31}P couplings and has a width corresponding to the average ^1H - ^{31}P couplings.

In natural spin diffusion, i.e. without proton decoupling, ^1H - ^{31}P dipolar couplings can produce a resonance shift that cancels the isotropic chemical shift difference $\Delta\omega$ and thus makes ^{31}P spin diffusion possible. In this manner, the protons drive the ^{31}P spin diffusion. Note that proton driven spin diffusion does not involve a transfer of magnetization via protons, the transfer occurs through space from ^{31}P to ^{31}P .

Thus, without decoupling the transition probability of two exchanging nuclei having the same resonance frequency is low because the proton local fields causes a large spread in the ^{31}P resonance frequencies. The probability increases when the spread is narrowed by incomplete proton decoupling. If the nuclei have different chemical shifts, complete proton decoupling quenches the probability of spin diffusion.

The second $\pi/2$ pulse returns the magnetization back to the transverse plane before acquisition (t_2) under TPPM decoupling.

The measured 2D NMR spectrum represents the correlation function between the NMR resonance frequencies ω_1 before and ω_2 after an exchange time τ_m . Any exchange process that couples different resonance frequencies ω_1 and ω_2 will manifest itself by off diagonal peaks in the 2D spectrum. In order to suppress off diagonal peaks resulting from the reorientation of the rotor, the mixing time was chosen as an integer multiple of the rotor period, t_r .

3.3.2 PMLG (Phase Modulated Lee-Goldburg)

Accurate and precise measurements of the heteronuclear correlations (HETCOR) between dilute spins and abundant spins (^1H) are complicated by the strong homonuclear ^1H - ^1H dipolar couplings. A variety of multiple pulse sequences, including WAHUHA (Waugh-Huber-Haeberlen), MREV-8 (Mansfield-Rhim-Elleman-Vaughan, 8 pulses per cycle), BR-24 (Borum-Rhim, three partly nested MREV-8), DUMBO (decoupling using mind-boggling optimization), FSLG (frequency switched Lee-Goldburg), PMLG (phase modulated Lee-Goldburg) can be applied during the t_1 interval of conventional 2D experiments to suppress homonuclear dipolar couplings while the heteronuclear dipolar couplings are effecting the evolution of the dilute spin magnetization generated by cross-polarization. In PMLG [Vinogradov *et al.*, 1999] experiments line narrowing is accomplished by a series of m pulses with well defined phases. Throughout this thesis, the CP MAS PMLG experiment was used to measure heteronuclear correlation spectra. The pulse program is shown in Figure 3.3a.

The sequence starts with a magic angle preparation pulse ($\theta_m = 54.74^\circ$) that puts the ^1H polarization along the magic angle with respect to the static magnetic field, along z axis. After ^1H excitation, the protons are allowed to evolve for a time t_1 under PMLG irradiation (ω_1) to suppress the ^1H homonuclear dipolar couplings. Frequency switching in the PMLG sequence was accomplished using a linear phase ramp. The phase ramp consists of a train of phase values incremented at $10^\circ (= \Delta\alpha)$ steps. A basic unit in the phase file consists of phase

angles of $0^\circ \dots 208^\circ$ and $28^\circ \dots -180^\circ$. The duration of each basic unit was synchronized with two 360° pulses around the PMLG effective field.

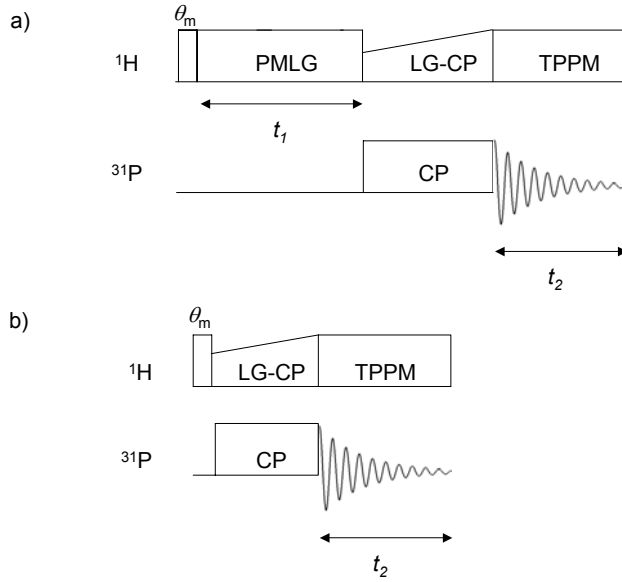


Figure 3.3 a) Pulse sequence used for the 2D PMLG ^1H - ^{31}P heteronuclear correlation spectra with LG-CP.

b) Pulse sequence used to optimized the CP condition.

Following the PMLG sequence, LG-CP (Lee-Goldburg cross-polarization) is applied to transfer the magnetization from the protons to the phosphorus. The LG irradiation suppresses the ^1H homonuclear dipolar interactions while CP enhances the ^{31}P signal. It was shown that at high spinning sample rates, $\omega_r/2\pi$, an effective polarization transfer takes place when $\omega_{eff,I} - \omega_{1S} = n\omega_r$, where $\omega_{eff,I} = \sqrt{\omega_{1I}^2 + \Delta\omega_{LG}^2}$ [3.3]

$$\omega_{1I} = -\gamma_I B_{1I} \quad [3.4]$$

and:
$$\Delta\omega_{LG} = \omega_{1I} \tan^{-1} \theta_m \quad [3.5]$$

$$\omega_{1S} = -\gamma_S B_{1S} \quad [3.6]$$

$$n = \pm 1, \pm 2$$

The ^{31}P nuclei were locked on resonance in the xy -plane with a r.f. intensity optimized experimentally using a 1D LG-CP experiment (see Figure 3.3b). The ^{31}P free induction decays were recorded during t_2 under TPPM decoupling. A 2D ^{31}P - ^1H HETCOR spectrum contains the ^{31}P resonances in the direct dimension correlated with the ^1H resonances in the indirect dimension.

The efficiency of the PMLG decoupling was optimized using adamantane. After properly setting all experimental parameters, the J_{CH} couplings could be resolved in 1D ^{13}C spectrum collected with PMLG decoupling during data acquisition (Figure 3.4).

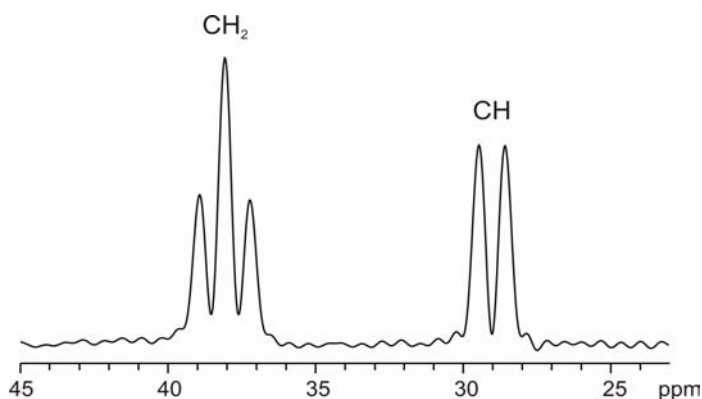


Figure 3.4 ^{13}C spectrum of adamantane (natural abundance) under PMLG decoupling. Conditions are: $\omega_r/2\pi = 5$ kHz, $n_s = 1024$, $T_{\text{CP}} = 6$ ms, $\omega_1 = 83$ kHz, $m = 20$, $\Delta\alpha = 10^\circ$.

The combined effect of strong homonuclear dipolar interactions between the abundant protons in solid-state and the small proton chemical shift dispersion limits the resolution in the ^1H solid-state NMR spectrum. Different lines in a simple MAS spectrum are, therefore, often not resolved. Spectral resolution is improved using a 2D ^1H - ^1H correlation experiment (see Figure 3.5) where PMLG decoupling is used in the t_1 dimension [Vinogradov *et al.*, 1999].

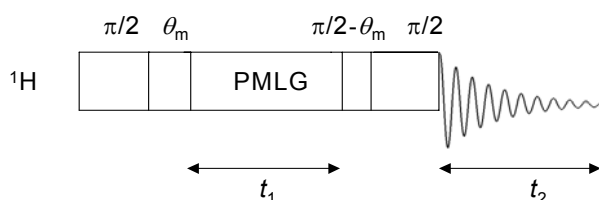


Figure 3.5 Pulse sequence used for 2D ^1H - ^1H correlation experiment.

The initial magnetization, created by two pulses as shown in Figure 3.5, evolves in a plane perpendicular to the direction of the effective chemical shift Hamiltonian. During the evolution period t_1 , ^1H homonuclear dipolar couplings are suppressed due to PMLG decoupling. The $\pi/2 - \theta_m$ pulse transfers the precession plane to a plane perpendicular to the xy -plane. After a $\pi/2$ pulse, the proton signal is acquired during the detection period t_2 . The indirect dimension of such 2D ^1H - ^1H correlation experiments is the highly resolved spectrum while the direct dimension yields the normal ^1H MAS NMR spectrum.

2D ^1H - ^1H correlation spectra were referenced externally. In indirect dimension, the CH_2 line of glycine was set to 2.6 ppm (Figure 3.6). The direct dimension was referenced using silicone rubber (0 ppm).

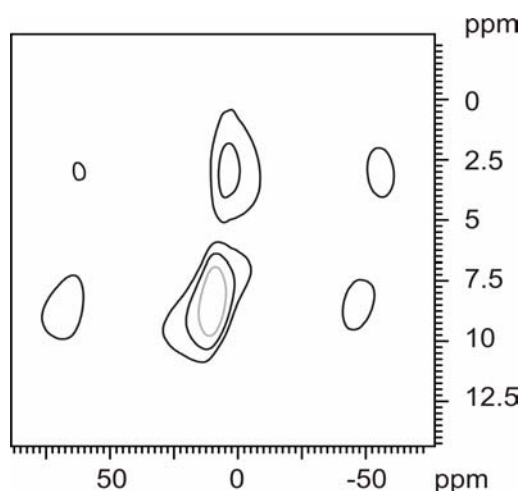


Figure 3.6 Two-dimensional ^1H - ^1H correlation spectrum of glycine (contour plot). ($\omega_r/2\pi = 16$ kHz, $n_s = 1$, θ_m length = $1.82 \mu\text{s}$, $\omega_1 = 83$ kHz, $m = 20$, $\Delta\alpha = 10^\circ$).

3.3.3 Refocused INADEQUATE (Incredible Natural Abundance Double QUAntum Transition Experiment)

In solid-state NMR, *through-bond* J -couplings are usually several orders of magnitude smaller than the broadening associated with anisotropic interactions such as through-space dipolar coupling and the chemical shift anisotropy. Nevertheless, an INADEQUATE experiment - analogous to the liquid-state experiment - has been proposed to determine the *through-bond* carbon-carbon connectivities in solid-state NMR [Lesage *et al.*, 1997]. Recently, the presence of a ^{15}N - ^{15}N J -coupling across a hydrogen bond was detected [Brown *et al.*, 2002]. A better alternative to determine *through-bond* connectivities is refocused INADEQUATE [Lesage *et al.*, 1999], an INADEQUATE-type experiment. It was shown that the refocused INADEQUATE experiment allows an unambiguous determination of the ^{31}P - ^{31}P oxygen mediated J -coupling in crystalline and disordered phosphates [Fayon *et al.*, 2002; Fayon *et al.*, 2003].

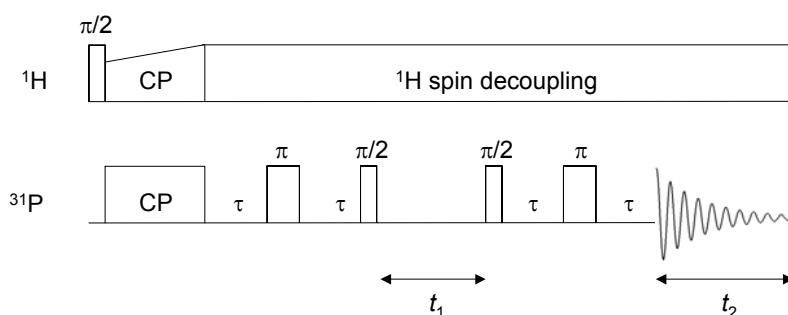


Figure 3.7 Pulse sequence for solid-state refocused INADEQUATE.

The pulse program of the refocused INADEQUATE experiment creates two principal signal components: S_0 from molecules with isolated ^{31}P nuclei and S_2 from molecules with coupled ^{31}P nuclei. The discrimination between S_0 and S_2 relies on phase cycling. As a result, the signal originating from S_0 cancels while the weak signals from molecules with coupled ^{31}P survive. The pulse sequence applied throughout this thesis is shown in Figure 3.7. After cross-polarization, the ^{31}P magnetization evolves during the delay 2τ under the isotropic homonuclear J -coupling Hamiltonian. The ^{31}P - ^{31}P homonuclear dipolar couplings are removed by fast magic angle spinning while the chemical shift anisotropy is refocused by the π pulse. The double quantum (DQ) coherence (which is not a measurable magnetization) created by the first $\pi/2$ pulse evolves during t_1 at the sum of the single quantum (SQ) frequencies of the two spins, $\omega_{DQ} = \omega_{SQ}^A + \omega_{SQ}^B$. Unfortunately, the DQ coherence cannot be detected directly. It needs to be reconverted into detectable SQ coherence. The last $\pi/2$ pulse reconverts the DQ coherence into an anti-phase transverse coherence. This anti-phase component is converted back during the second τ - π - τ delay into an in-phase signal before detection. In the refocused INADEQUATE SQ - DQ experiment, the resonances of two coupled phosphorus atoms occur at the common DQ frequency in indirect dimension and are correlated with the SQ frequency of each peak in the direct dimension. The maximum transfer of magnetization into DQ coherence is $\tau = 1/(4J_{P-P})$ and is zero for $\tau = 1/(2J_{P-P})$.

3.3.4 Rotational Resonance

Almost all the techniques used in solid-state NMR for structural studies utilize the high spectral resolution provided by MAS. This technique also averages the dipolar coupling between low γ nuclei (^{15}N , ^{13}C , ^{31}P). However, the observation of these interactions is often important for structural studies. Methods for the selective reintroduction of the desired couplings (“recoupling” techniques) are, therefore, of essential importance.

The rotational resonance technique [Raleigh *et al.*, 1988, Levitt *et al.*; 1990; Costa *et al.*, 2003] can be used to reintroduce to the homonuclear dipole-dipole coupling in spin pairs. In magic angle spinning experiments on samples containing dilute homonuclear spin pairs, rotational resonance occurs when the sample spinning rate is adjusted such that the condition $n \times \nu_r = \Delta\nu$ is fulfilled. Here, $\Delta\nu$ is the frequency distance between the considered signals, ν_r is the sample spinning rate and n is a small integer. Under these conditions, MAS does not completely average the dipolar interaction. Line broadening and splitting can be observed for

sufficiently strong dipolar couplings. The rotational resonance spectra presented within the present thesis were acquired using the common CP MAS experiment (Figure 3.8).

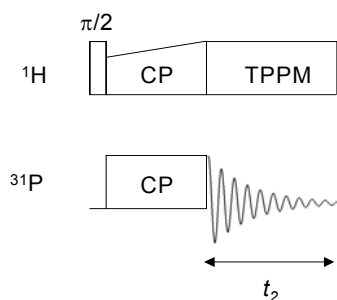


Figure 3.8 The pulse sequence for rotational resonance spectral lineshape measurements.

Simulations of the lineshape reveal the distance between the coupled spins since the measured through space dipole-dipole coupling constant (d_{II}) only depends on fundamental constants and the inverse third power of the internuclear distance (see equation [2.23]).

3.3.5 Temperature Calibration

For a higher sensitivity of the NMR experiments, especially for biological compounds, high-speeds MAS is required. MAS produces a speed-dependent heating of the sample. This heating is caused by the friction between the rotor and the gas flow. Accurate temperature measurement inside the sample is, therefore, not trivial. Variable temperature (VT) MAS NMR spectroscopy is of great importance for the study of molecular dynamics. Since temperature control is crucial for VT MAS experiments, the actual sample temperature needs to be measured internally. For the determination of the real sample temperature, the temperature isotropic shift of the ^{207}Pb resonance of lead nitrate $\text{Pb}(\text{NO}_3)_2$ [Ferguson *et al.*, 1995; Bielecki *et al.*, 1995] was used.

3.3.5.1 2.5 mm ZrO_2 rotor

The slope of the calibration curve for the chemical shift thermometer based on the ^{207}Pb resonance of lead nitrate for the 2.5 mm ZrO_2 is 0.56 ppm/K over the temperature range of 268-297 K [see also Ferguson *et al.*, 1995].

The dependence of the observed isotropic ^{207}Pb chemical shift of $\text{Pb}(\text{NO}_3)_2$ on the sample spinning rate, ν_r , at room temperature ($T = 293\text{K}$) is shown in Figure 3.9.

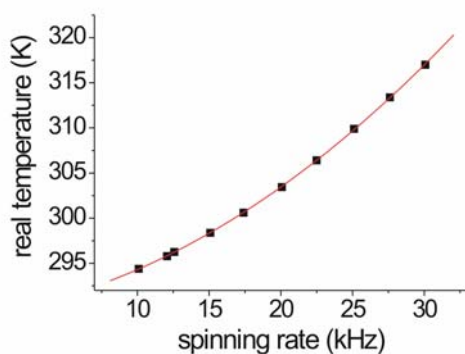


Figure 3.9 Real sample temperature versus sample spinning rate (2.5 mm ZrO₂ rotor at a set temperature of 293 K).

Increasing sample spinning rates give rise to an increase in sample temperature. Plotting the real sample temperature T vs. ν_r (Figure 3.9) gave a quadratic dependence of the type [Langer *et al.*, 1999]:

$$\frac{T}{K} = 288.94 + 0.3098 \cdot \frac{\nu_r}{\text{kHz}} + 0.0208 \cdot \left(\frac{\nu_r}{\text{kHz}} \right)^2 \quad [3.7]$$

The fitted quadratic dependence clearly indicates that the main factor affecting the temperature within the sample is not the spinning rate itself, but predominantly the kinetic energy of the rotor surface, a part that is converted into heat, as well as the bearing pressure used for spinning.

In Figure 3.10 the real sample temperature T (as derived from the isotropic ²⁰⁷Pb chemical shift) is plotted versus the set temperature T_b of the bearing gas at a sample spinning rate of 8 kHz.

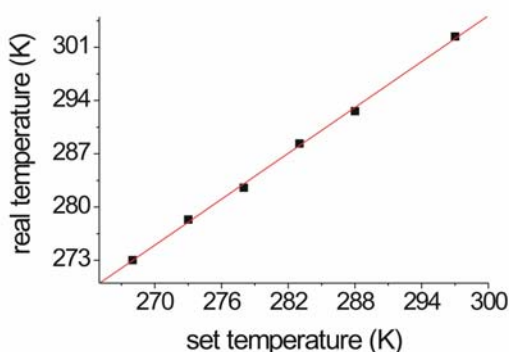


Figure 3.10 Calculated real lead nitrate temperature versus the bearing gas temperature (2.5 mm ZrO₂ rotor at $\nu_r = 8$ kHz).

The data fit to the function:

$$\frac{T}{K} = 1.095 + 1.005 \cdot \frac{T_b}{K} \quad [3.8]$$

3.3.5.2 4 mm ZrO₂ rotor

The dependence of the observed isotropic ²⁰⁷Pb chemical shift of Pb(NO₃)₂ on the sample spinning rate, ν_r , at room temperature ($T = 293\text{K}$) is shown in Figure 3.11. An increase in sample temperature is observed with increasing sample spinning rate.

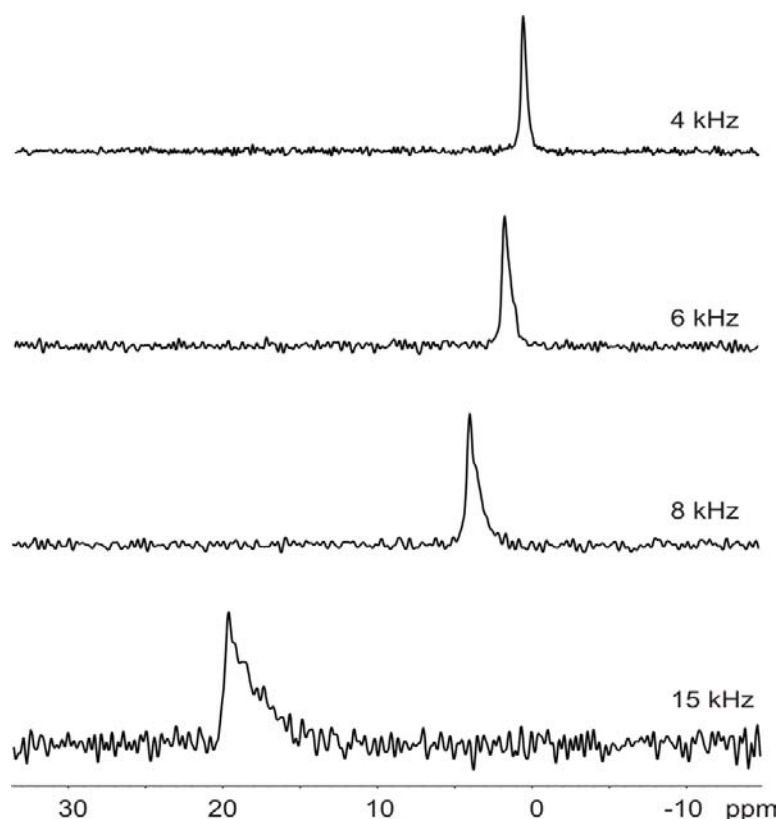


Figure 3.11 ²⁰⁷Pb spectra of lead nitrate obtained at sample spinning rates from 4 to 15 kHz for a 4 mm ZrO₂ rotor. The sample temperature rises with increasing sample spinning rate.

Brus [2000] reported that the temperature gradient along the rotor axis can be relatively large and it depends on the temperature of the air used for sample spinning. Furthermore, the end of the sample tends to be closer to the gas flow inlet than its center. For the observation of the temperature gradient, we analyzed the shape of the isotropic ²⁰⁷Pb signal of lead nitrate. The distribution of the chemical shift directly indicates the distribution of the temperature within the sample. As the basis for comparison of lineshapes and thus for determination of temperature gradient, we choose the signal of lead nitrate measured at 4 kHz. The halfwidth of this Lorentzian signal was only 0.48 ppm. Dramatic changes of the signal lineshape were observed with increasing sample spinning rate. It is known now that the

change of temperature about 1 K causes the change of the isotropic ^{207}Pb NMR chemical shift of lead nitrate of about 0.775 ppm [Ferguson *et al.*, 1995]. From the distribution of the chemical shift at 15 kHz we can estimate the temperature difference within the sample of ca. 4 K.

The dependence of the observed isotropic ^{207}Pb chemical shift of $\text{Pb}(\text{NO}_3)_2$ on the sample spinning rate, ν_r , at room temperature ($T = 293\text{K}$) is shown in Figure 3.12.

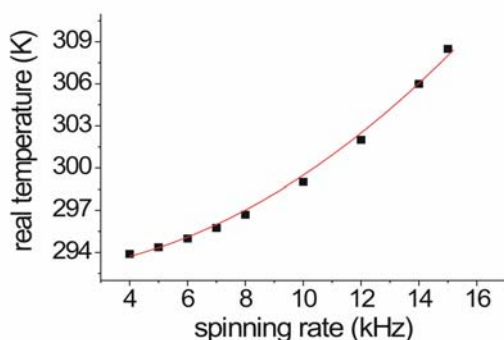


Figure 3.12 Real sample temperature versus the sample spinning rate for lead nitrate in a 4 mm ZrO_2 rotor at a set temperature of 293 K.

A satisfactory fit to the experimental data was obtained using a second order polynomial:

$$T/K = 292.59 + 0.108 \cdot \nu_r/kHz + 0.06 \cdot \left(\nu_r/kHz\right)^2 \quad [3.9]$$

Different VT MAS measurements were carried out at 5 kHz.

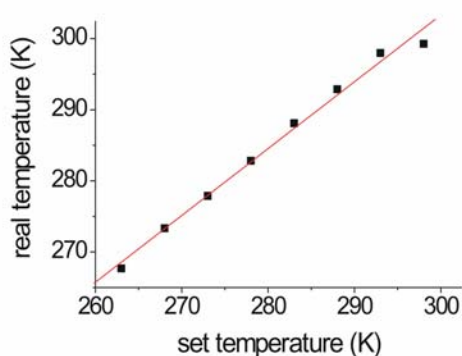


Figure 3.13 Calculated real lead nitrate temperature versus the air flow temperature in a 4 mm ZrO_2 rotor at $\nu_r = 5$ kHz.

In Figure 3.13, the real sample temperature T (as derived from the isotropic ^{207}Pb chemical shift) is plotted versus the set air flow temperature.

The data fit to a straight line:

$$T/K = 1.0187 + 1.0125 \cdot T_a/K \quad [3.10]$$

where T_a is the temperature of the air flow applied to the rotor.

4. Results and Discussion

4.1 Solid-State ^{31}P NMR Spectroscopy of Phosphorylated Amino Acids

Liquid-state ^{31}P NMR spectroscopy is extensively used to study phosphorylated peptides and proteins [Tanokur *et al.*, 1999; Brauer *et al.*, 1981; Geyer *et al.*, 1996; Kumon *et al.*, 1996]. Triggered by methodical advances, solid-state ^{31}P NMR spectroscopy currently gains increasing importance for the characterisation of phosphate-binding peptides and proteins [Bak *et al.*, 2001; McDowell *et al.*, 1996; Pinheiro *et al.*, 1994; Stumber *et al.*, 2002]. It could be shown that solid-state ^{31}P NMR spectroscopy is capable of detecting slow conformational changes of the molecules in the crystalline state [Stumber *et al.*, 2002]. A major problem of such studies, however, is the relatively low amount of sample available. In contrast, sufficient amounts of crystalline phosphorylated amino acids such as O-phospho-L-serine, O-phospho-L-threonine, and O-phospho-L-tyrosine (further abbreviated by P-Ser, P-Thr, and P-Tyr, respectively) are commercially available.

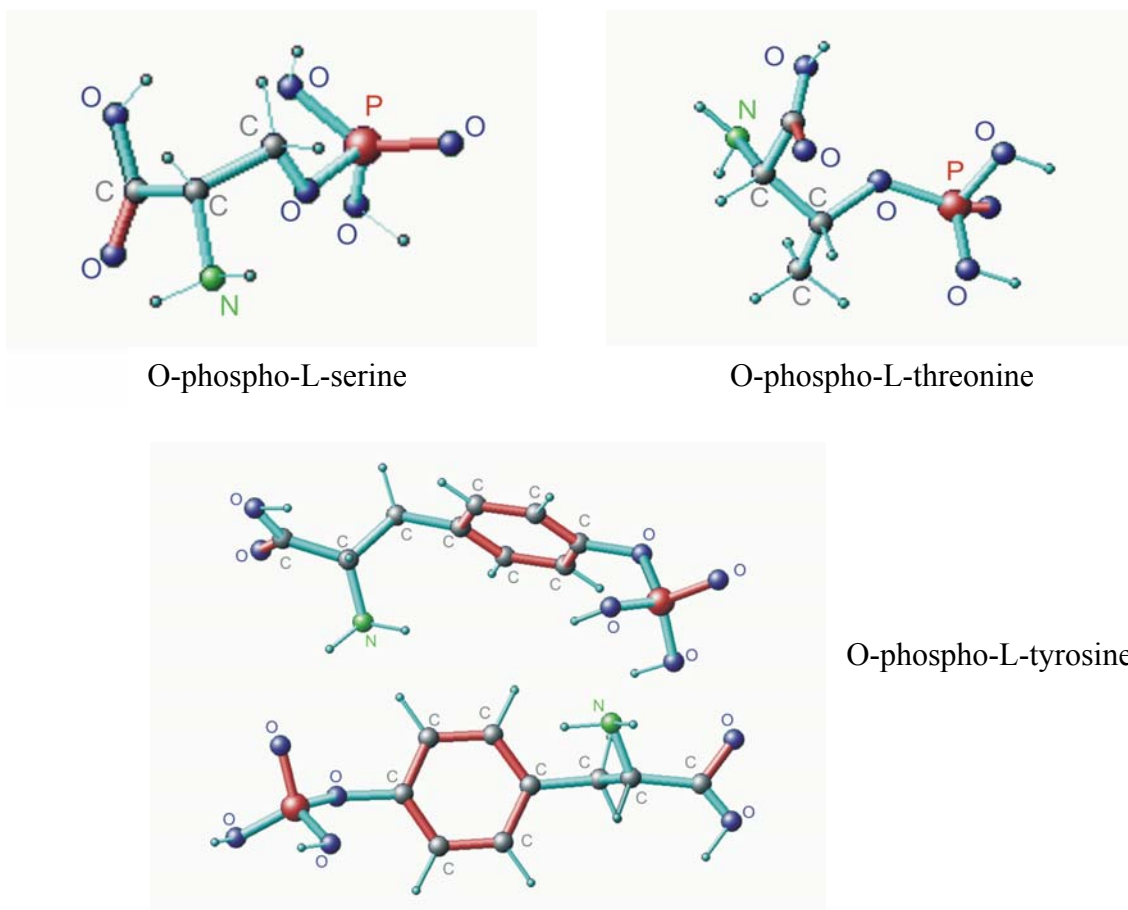


Figure 4.1 The molecular structure of P-Ser, P-Thr, and P-Tyr.

These substances can be used as model compounds in order to design and optimise solid-state ^{31}P NMR experiments to study phosphorylated peptides and proteins. By combining cross-polarization (CP) [Hartmann *et al.*, 1962; Pines *et al.*, 1972, Pines *et al.*, 1973] with magic angle spinning (MAS) [Andrew *et al.*, 1958; Lowe, 1959] and heteronuclear spin-spin decoupling techniques [Bennet *et al.*, 1995], highly resolved spectra can be obtained.

While the X-ray structures of P-Ser [Bryndal *et al.*, 2002] and P-Thr [Maniukiewicz *et al.*, 1996] reveal one unique molecular conformation within the unit cell, P-Tyr [Suga *et al.*, 1998] exhibits two different conformations of equal population (Figure 4.1). Two different torsion angles defining the orientation of the phosphate group with respect to the aromatic ring exists.

Conventional one-dimensional CP MAS experiments performed on all samples (see also Potrzebowski *et al.*, 2003) are in complete agreement with the crystallographic data.

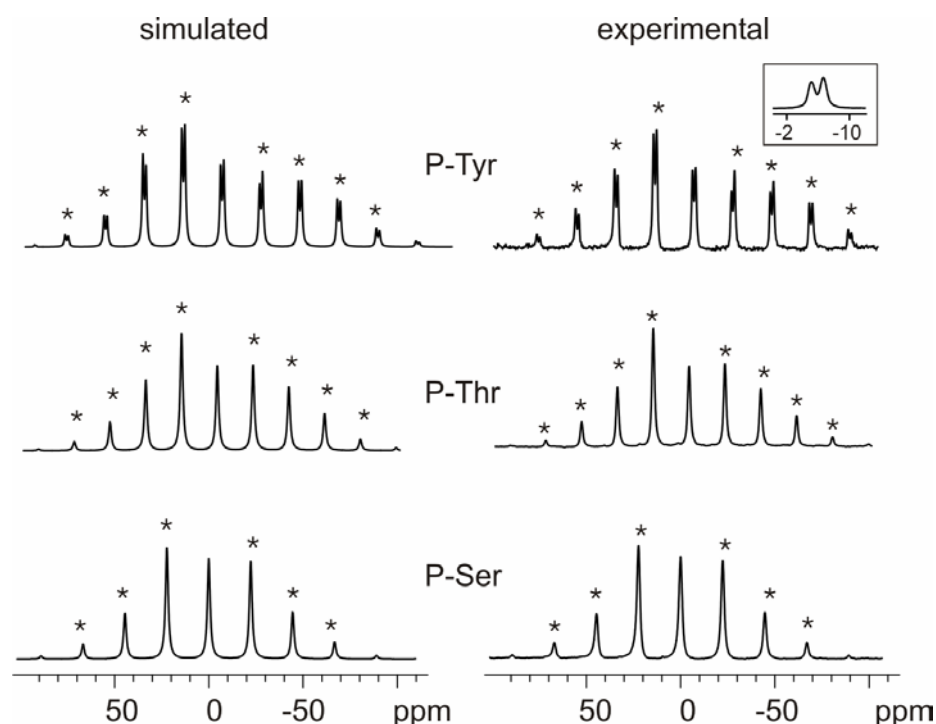


Figure 4.2 Experimental and simulated ^{31}P $\{^1\text{H}\}$ CP MAS spectra of P-Tyr ($\omega_r/(2\pi) = 2.32$ kHz), P-Thr ($\omega_r/(2\pi) = 2.2$ kHz), and P-Ser ($\omega_r/(2\pi) = 2.36$ kHz) in the presence of TPPM decoupling applied to the protons. 16 scans with a recycle delay of 4 s were added. Lorentzian broadening of 30 Hz was applied. The inset shows that the P-Tyr central peak splits into two signals. Spinning side bands are marked with asterisks.

Simulation (Figure 4. 2) of the spinning sideband patterns using the SIMPSON software [Bak *et al.*, 2000] allows to determine the values for the chemical shift anisotropy, $\Delta\sigma$, and the

asymmetry parameter, η (see Table 4.1). Values for δ_{iso} , $\Delta\sigma$, and η were published recently [Potrzebowski *et al.*, 2003] and are in reasonable agreement with the data determined here.

Compound	δ_{iso} / ppm (± 0.1 ppm)	$\Delta\sigma$ / ppm (± 3 ppm)	η (± 0.1)
P-Ser	0.3	85.5	0.9
P-Thr	-4.5	105	0.8
P-Tyr (peak 1)	-5.1	117	0.7
(peak 2)	-6.6	124.5	0.6

Table 4.1 Chemical shift parameters of phosphorylated amino acids in solid-state. All isotropic chemical shifts, δ_{iso} , and chemical shift anisotropies, $\Delta\sigma$, are given in ppm relative to 85% H_3PO_4 . The asymmetry parameter, η , is dimensionless. The following convention is used: $\delta_{\text{iso}} = 1/3(\delta_{\text{xx}} + \delta_{\text{yy}} + \delta_{\text{zz}})$, $\Delta\sigma = 1/2(\delta_{\text{xx}} + \delta_{\text{yy}}) - \delta_{\text{zz}}$, $\eta = 3/2 (\delta_{\text{xx}} - \delta_{\text{yy}})/\Delta\sigma$, $|\delta_{\text{zz}} - \delta_{\text{iso}}| > |\delta_{\text{xx}} - \delta_{\text{iso}}| > |\delta_{\text{yy}} - \delta_{\text{iso}}|$. Here, δ_{zz} , δ_{yy} , and δ_{xx} denote the principal values of the chemical shift tensor.

The repetition time in the CP MAS experiments is dictated by the longitudinal relaxation time, T_1^{H} , of the ^1H nuclei serving as the source of magnetization in the CP experiment. As determined by a standard cross-polarization inversion-recovery pulse sequence, T_1^{H} of P-Ser (148 ms) is much shorter than that of ^{31}P ($T_1^{\text{P}} = 64$ s). The same is true for P-Thr ($T_1^{\text{H}} = 70$ ms, $T_1^{\text{P}} = 25$ s) and P-Tyr (T_1^{H} (peak1) = 35 ms, T_1^{H} (peak2) = 45 ms, T_1^{P} (peak1) = 16 s, T_1^{P} (peak2) = 19 s; for the identification of peak1 and 2 see Table 4.1). The CP build-up time, T_{IS} , is correlated with the strength of the ^1H - ^{31}P dipole coupling. P-Ser and P-Thr exhibit larger T_{IS} values (250 μs and 150 μs , respectively) than P-Tyr (75 μs). The two phosphorus sites in P-Tyr behave very similar (see Figure 4.3 and Table 4.2).

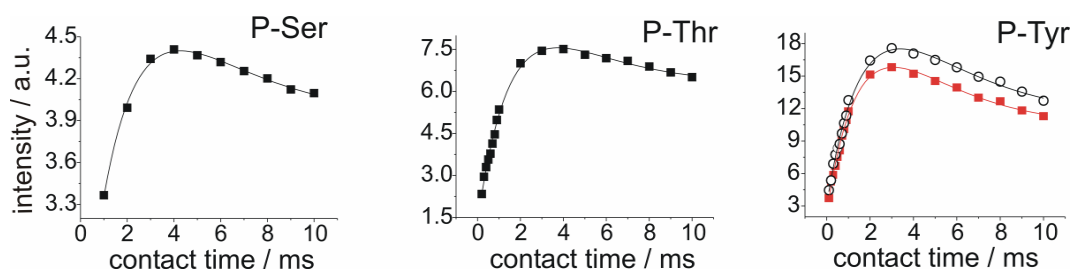


Figure 4.3 Variation of the ^{31}P cross-polarization signal, I_{CP} , as a function of contact time. $T_{1\text{p}}^{\text{H}}$ and T_{IS} were determined from these CP build-up curves. They could be described by equation [2.45].

The optimum CP contact time, T_{CP} , is determined by both T_{IS} and the longitudinal relaxation time of ^1H in the rotating frame, $T_{1\rho}^H$. T_{CP} was found to amount to 4 ms for P-Ser and P-Thr and to 3 ms for P-Tyr (Figure 4.3). The $T_{1\rho}^H$ values determined here for P-Ser, P-Thr, and P-Tyr are shorter than the values typically found in non-phosphorylated amino acids and peptides [Mehring, 1983; Andrew *et al.*, 1974; Gu *et al.*, 1996; Wang *et al.*, 1999; Bouchard *et al.*, 1998]. The relaxation times are summarized in Table 4.2.

Compound	T_1^P / s ($\pm 5\%$)	T_1^H / ms ($\pm 5\%$)	$T_{1\rho}^H$ / ms ($\pm 10\%$)	T_{IS} / μs ($\pm 10\%$)	T_{CP} / ms ($\pm 10\%$)
P-Ser	64	148	57	250	4
P-Thr	25	70	27	150	4
P-Tyr (peak 1)	16	35	12	75	3
(peak 2)	19	45	12	75	3

Table 4.2 NMR parameters of phosphorylated amino acids in solid-state.

Solid-state NMR is capable of extracting quantitative information about molecular motions such as conformational exchange. A series of 2D exchange experiments (EXSY, [Jeneer *et al.*, 1979; Szeverenyi *et al.*, 1982]) was carried out for P-Tyr in order to study a possible conformational exchange between the two different states of the molecule. The 2D EXSY spectrum of P-Tyr shows off diagonal peaks.

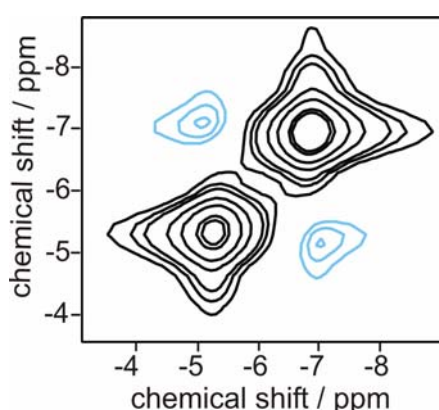


Figure 4.4 Experimental 2D EXSY ^{31}P MAS NMR spectrum of P-Tyr at a mixing time of 50 ms, a recycle delay of 0.3 s and 512 t_1 increments (4 scans). The sample spinning rate was 10 kHz. The cross-polarization contact time was set to 2.8 ms. TPPM decoupling was used during t_1 and the data acquisition at a decoupling field strength corresponding to 47 kHz.

Smaller cross-peaks relative to the diagonal peaks show up already at ca. 20 ms mixing time. The presence of cross-peaks (see Figure 4.4) proves the existence of an exchange during the mixing time which may arise from conformational changes as well as from magnetization transfer mediated by ^{31}P - ^{31}P spin diffusion [Edzes *et al.*, 1984]. Under

magic angle spinning, however, secular contributions to the ^{31}P - ^{31}P magnetic dipole interaction are suppressed as long as the sample spinning rate is large compared to the ^{31}P - ^{31}P coupling constant [Ernst, 2003]; a condition that is fulfilled in our experiments.

Proton driven spin diffusion can be suppressed by heteronuclear decoupling provided the decoupling field strength is high enough [Edzes *et al.*, 1984; Levitt *et al.*, 1990]. This could be proven by the variation of the decoupling field strength (see Figure 4.5a). The pronounced increase of the average cross-peak intensity, I_{AB} , i.e. the decrease of I_{AA}/I_{AB} for a decoupling field strength below ca. 30 kHz (0.6 a.u.) shows that spin diffusion significantly influences the spectra for low decoupling field strengths. Here, I_{AA} denotes the averaged intensity of the diagonal peaks. For sufficiently high decoupling field strengths (> 30 kHz), however, the influence of spin diffusion is obviously suppressed. It is, therefore, concluded that the cross-peaks observed in our 2D exchange spectra indicate the presence of slow conformational exchange rather than proton driven spin diffusion which predominates in the absence of proton decoupling [Potrzebowski *et al.*, 2003]. This interpretation is supported by an additional experiment: A raise in temperature increases the rate of exchange (see Figure 4.5b), which is not expected for spin diffusion.

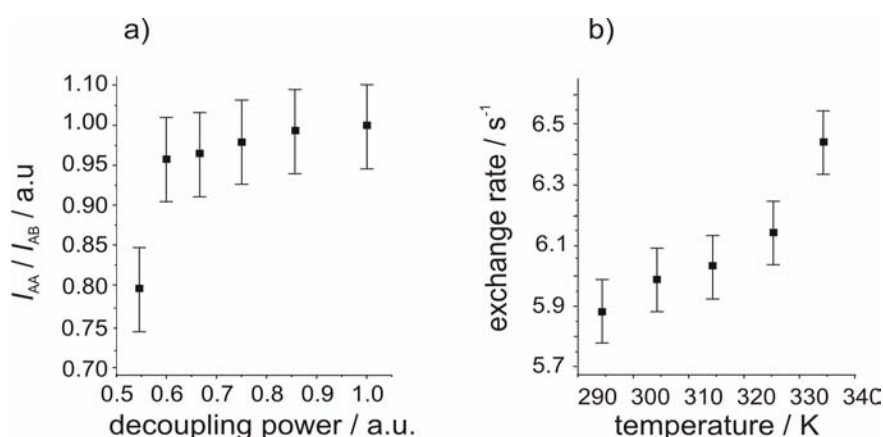


Figure 4.5 (a) Normalized ratio I_{AA}/I_{AB} of the averaged diagonal peak intensity, I_{AA} , and the averaged cross-peak intensity, I_{AB} , as a function of the normalized proton decoupling field strength. The decoupling field strength was varied up to a maximum value corresponding to $\omega_1/(2\pi) = 47$ kHz (1 a.u.). The mixing time was set to 0.4 s. (b) Dependence of the exchange rate, k , on the temperature.

The transfer of longitudinal magnetization between the two spin sites was monitored as a function of τ_m (Figure 4.6). The rate constant is determined as the slope of the plot I_{AB}/M_j^0 vs. τ_m . M_j^0 represents the equilibrium z magnetization of nuclei in site j ($j=A, B$). A value of

6 s^{-1} was obtained for the conformational exchange between the two different molecular conformations at 302 K.

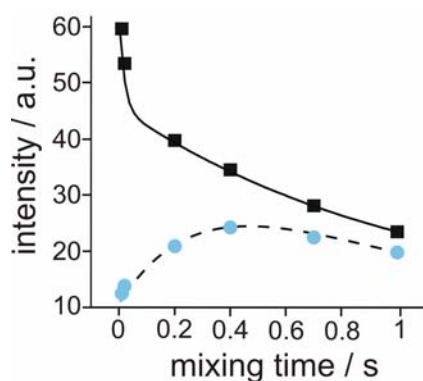


Figure 4.6 Longitudinal magnetization transfer curves of P-Tyr for τ_m up to 1 s. The lines come from a fit to equations:

$$I_{AA}(\tau_m) = I_{BB}(\tau_m) = \frac{1}{4} \frac{\tau_m}{T_1} (1 + e^{-k\tau_m})$$

$$I_{AB}(\tau_m) = I_{BA}(\tau_m) = \frac{1}{4} \frac{\tau_m}{T_1} (1 - e^{-k\tau_m})$$

The combined effect of strong homonuclear dipolar interactions between the abundant protons in solid-state and the small proton chemical shift dispersion limits the resolution in the ^1H NMR solid-state spectrum. Spectral resolution can be obtained using a 2D ^1H - ^1H correlation experiment where PMLG decoupling is used in the t_1 dimension [Vinogradov *et al.*, 1999]. The 2D ^1H - ^1H correlation experiment was applied to the phosphorylated amino acids. 1D ^1H high speed MAS NMR spectra of P-Ser, P-Thr, and P-Tyr were published [Potrzebowski *et al.*, 2003]. Compared with these spectra, substantially improved resolution is obtained in the indirect dimension of the ^1H - ^1H correlation spectra. Figure 4.7 shows the contour plots of the 2D ^1H - ^1H correlation spectra of the three phosphorylated amino acids.

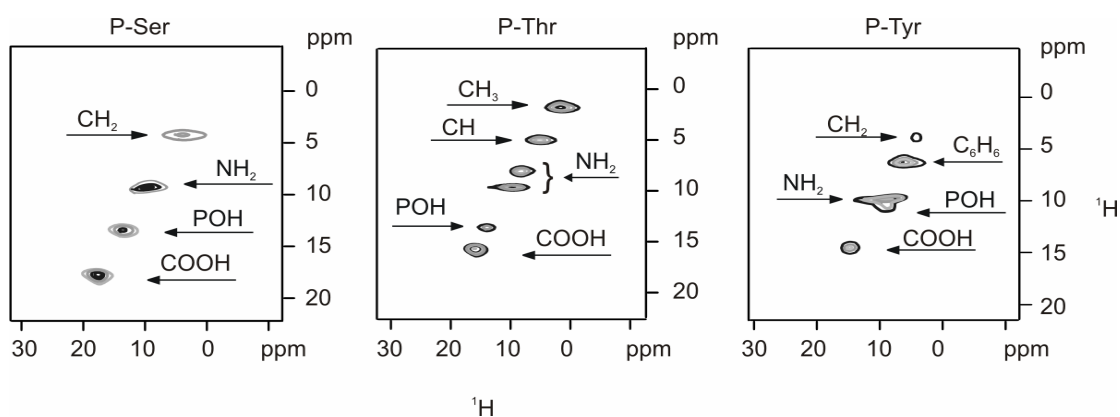


Figure 4.7 Contour plots of 2D ^1H - ^1H correlation spectra of P-Ser, P-Thr, and P-Tyr with magic angle spinning at 16 kHz, 512 t_1 increments and 4 scans per t_1 value. The assignment is indicated.

In agreement with Potrzebowski *et al.* [2003] we assign the peaks as shown in Table 4.3.

	P-O-H...O-P	C-O-H...O-P	N-H...O-P	CH	CH ₂	CH ₃	C ₆ H ₆
	$\delta_{\text{iso}} / \text{ppm}$						
P-Ser	13.6	17.7	8.5	-	3.8	-	-
P-Thr	13.9	15.9	8.2;9.6	5.1	-	1.6	-
P-Tyr	10.9	14.5	9.8	-	4	-	5.8

Table 4.3 ^1H isotropic chemical shifts of P-Ser, P-Thr, and P-Tyr extracted from 2D ^1H - ^1H correlation spectra.

The most straightforward way to obtain improved proton resolution is by exploiting the large chemical shift of a second type of nucleus (^{31}P) or of the heteronuclear dipolar couplings (^1H - ^{31}P) in 2D correlation spectroscopy. Therefore, having obtained indirectly resolved proton spectra it is possible to perform 2D ^1H - ^{31}P HETCOR experiments. Figure 4.8 shows the 2D spectra of P-Ser, P-Thr, and P-Tyr where cross-peaks appear at the proton and ^{31}P isotropic chemical shifts for each pair of coupled spins of the ^1H - ^{31}P pairs of the three phosphorylated amino acids. In order to precisely assign the closest protons, the classical approach is to use short contact times. But this option decreases the intensity of the signals and is thus time consuming. An alternative is to transfer ^1H magnetization under Lee-Goldburg condition (LG-CP). Using LG-CP transfer, which quenches ^1H spin diffusion, the cross-peaks observed for our samples at a mixing time of 2 ms correspond to the neighbouring protons of the considered ^{31}P nucleus.

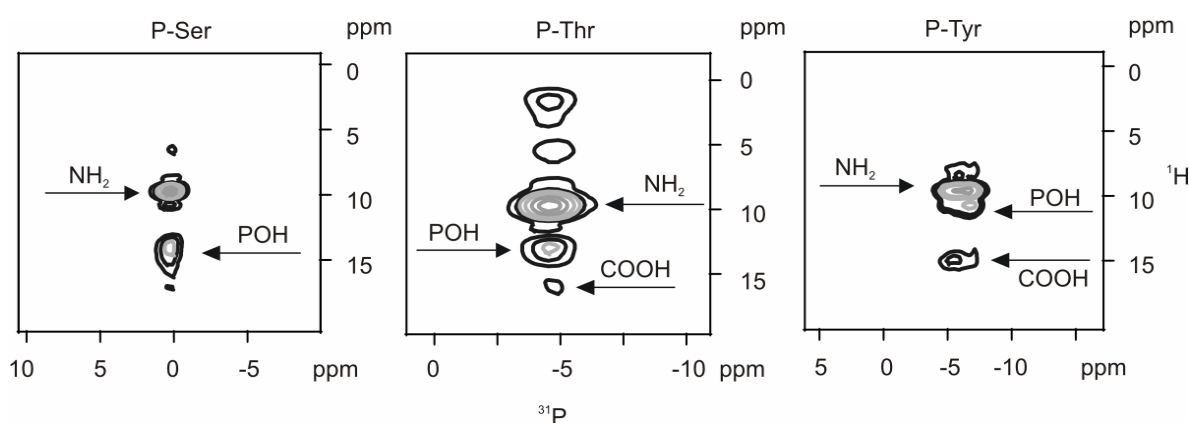


Figure 4.8 Contour plots of 2D PMLG decoupled ^1H - ^{31}P heteronuclear dipolar correlation spectra of P-Ser, P-Thr, and P-Tyr. The data were obtained at a sample spinning rate of 16 kHz, 512 t_1 increments, 1 scan per t_1 value and with a LG-CP mixing time of 2 ms.

The hydrogen bond distances in phosphorylated amino acids were reported in papers dealing with the X-ray analysis of these compounds [Bryndal *et al.*, 2002; Maniukiewicz *et al.*, 1996; Suga *et al.*, 1998]. In each case, the hydrogen bond involves the phosphate,

carboxyl, and amino groups. The assignment of the ^1H signals in 2D ^1H - ^{31}P HETCOR spectra of P-Ser, P-Thr, and P-Tyr is shown in Table 4.4.

	P-O-H \cdots O-P		C-O-H \cdots O-P		N-H \cdots O-P	
	$\delta_{\text{iso}}/\text{ppm}$	distance / \AA	$\delta_{\text{iso}}/\text{ppm}$	distance / \AA	$\delta_{\text{iso}}/\text{ppm}$	distance / \AA
P-Ser	14	2.55	17	2.49	9.4	2.78
P-Thr	12.7	2.52	15.7	2.53	9.5	2.82
P-Tyr	10.7	2.65	14.9	2.58	9.5	2.73

Table 4.4 ^1H isotropic chemical shifts of phosphorylated amino acids measured from the 2D ^1H - ^{31}P HETCOR spectra together with hydrogen bond distances in P-Ser, P-Thr, and P-Tyr.

Based on the assignment of the 2D ^1H - ^1H correlation spectra of the phosphorylated amino acids, the assignment for the ^{31}P - ^1H HETCOR spectra was straightforward. Note that the ^1H signals of to P-O-H \cdots O-P do not exhibit identical chemical shifts in the different compounds; the same is valid for C-O-H \cdots O-P. This is due to the well known dependence of the ^1H NMR chemical shift on the hydrogen bond distance. Longer hydrogen bonds give rise to smaller isotropic chemical shifts [Potrzebowki *et al.*, 2003; Brunner *et al.*, 1998; Harris *et al.*, 1988]. The signal at 9.4 ppm was assigned to the ^1H NMR signals of the amino groups.

The build-up curves of the 9.4 ppm signals in the 2D ^1H - ^{31}P LG-CP HETCOR spectra of P-Ser, P-Thr, and P-Tyr do not exhibit characteristic oscillations. The hydrogen bond distance between ^{31}P and the corresponding ^1H of the amino group could, therefore, not be measured [Bertani *et al.*, 1998]. The distance is, however, known from the X-ray studies (see Table 4.4). It was shown [van Rossum *et al.*, 2000] that oscillations in the cross-polarization dynamics cannot be observed for distances exceeding 2 \AA . Nevertheless, the CP build-up times were determined and compared with the total values obtained from the build-up curves of ordinary ^{31}P $\{^1\text{H}\}$ CP MAS experiments [Iuga *et al.*, 2004]. T_{IS} values of 169 μs , 146 μs , and 70 μs for P-Ser, P-Thr, and P-Tyr were determined from build-up curves of the cross-peak at the ^1H chemical shift of 9.4 ppm. These values are shorter than the total T_{IS} extracted from CP experiments. This behaviour is due to the influence of other protons (apart from H-N) to the total T_{IS} .

4.2 Solid-State ^{31}P NMR Spectroscopy of Ras $\cdot\text{Mg}^{2+}\cdot\text{GppCH}_2\text{p}$

4.2.1 Solid-State ^{31}P NMR Spectroscopy of Ras(wt) $\cdot\text{Mg}^{2+}\cdot\text{GppCH}_2\text{p}$

The ^{31}P NMR spectrum of triphosphates bound to proteins shows three resonance lines, corresponding to the α -, β -, and γ -phosphate group of the complexed nucleotide. Figure 4.9 exhibits the ^{31}P $\{^1\text{H}\}$ CP MAS NMR spectra of Ras(wt) $\cdot\text{Mg}^{2+}\cdot\text{GppCH}_2\text{p}$ at different temperatures. The central line of the ^{31}P $\{^1\text{H}\}$ CP MAS NMR spectrum of Ras(wt) $\cdot\text{Mg}^{2+}\cdot\text{GppCH}_2\text{p}$ contains three well-resolved signals at chemical shifts of -12.8, 7.3, and 18.8 ppm (303 K). A temperature decrease to 273 K does not lead to protein denaturation, since the original spectrum is restored after raising the temperature back to 303 K.

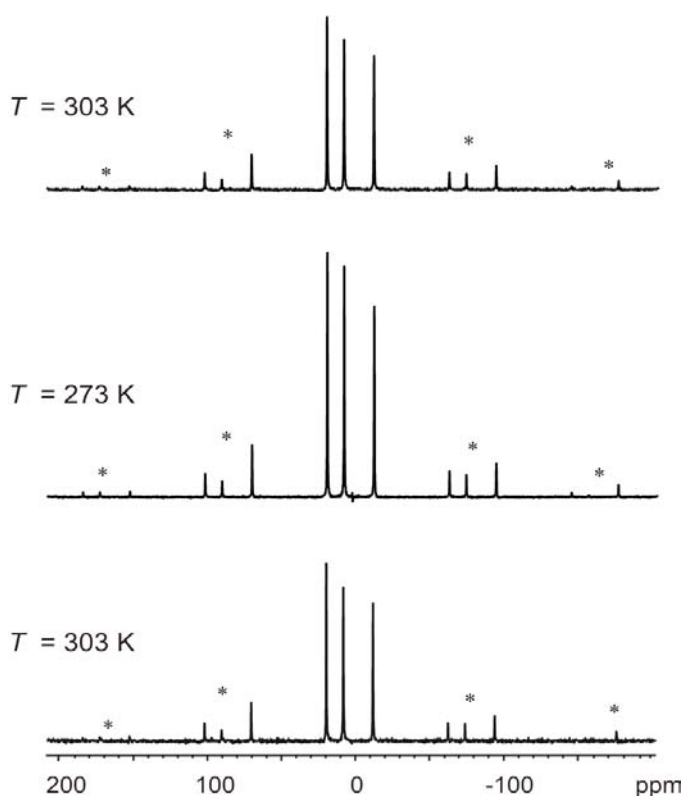


Figure 4.9 1D ^{31}P $\{^1\text{H}\}$ CP MAS spectra of Ras(wt) $\cdot\text{Mg}^{2+}\cdot\text{GppCH}_2\text{p}$ at different temperatures: Top: 303 K, Middle: 273 K, Bottom: 303 K (after cooling down the sample to 273 K). Spinning side bands are marked with asterisks. The spectra (128 k scans) were recorded at 10 kHz sample spinning rate using TPPM decoupling. The recycle delay was 0.5 s and the cross-polarization mixing time was set to 3 ms.

In a common ^{31}P $\{^1\text{H}\}$ CP MAS experiment, the recycle delay is one of the most important parameters to be set. It must be at least 5 times the T_1^{H} value, the latter time being required for the nuclei to regain the equilibrium in magnetization. Although a relatively high amount of crystalline Ras protein was available (36 mg), the acquisition of a ^{31}P $\{^1\text{H}\}$ CP MAS NMR spectrum required a measurement time of about 20 hours even under optimised conditions. Therefore, it was impossible to determine the proton T_1 of the protein in a decent

experimental time. We showed, however, that phosphorylated amino acids: P-Ser, P-Thr, and P-Tyr could be used as model compounds for the study of the Ras protein. Using the T_I^H values determined for these phosphorylated amino acids, we set the recycle delay for the acquisition of the Ras protein spectra to 0.5 ms. The choice of the best contact time for the polarization transfer between ^1H and ^{31}P is essential for obtaining reproducible and quantitative ^{31}P $\{^1\text{H}\}$ CP MAS NMR spectra. The optimum contact time (T_{CP}) should ensure that - under the applied experimental conditions - the signal intensity is maximum. We have measured spectra at variable contact times in order to determine T_{CP} . The observed build-up curves are shown in Figure 4.10. Based on these measurements, an optimum contact time of 3 ms was chosen.

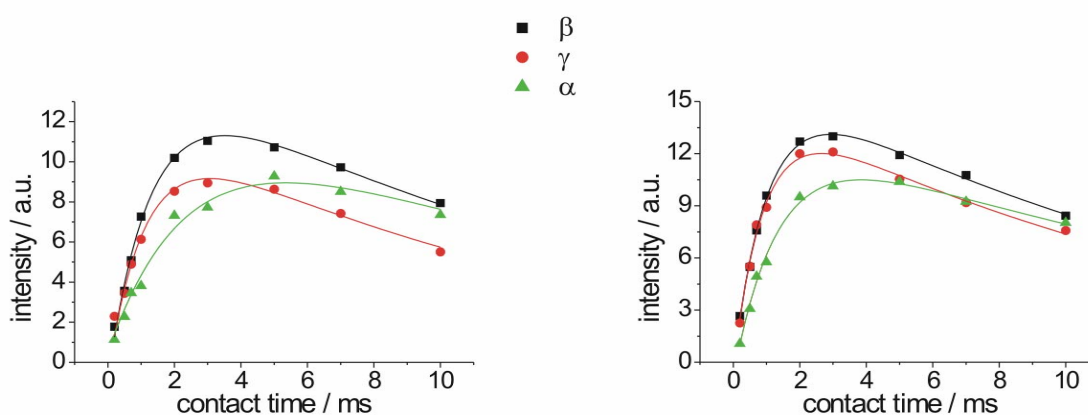


Figure 4.10 Variation of the intensity of the ^{31}P $\{^1\text{H}\}$ cross-polarization MAS signals, I_{CP} , of Ras(wt)·Mg $^{2+}$ ·GppCH $_2$ p at $T = 303$ K (left) and $T = 273$ K (right) as function of contact time. The solid lines represent a fit to the equation:

$$I_{CP} \sim (1 - \lambda)^{-1} (1 - e^{-(1 - \lambda)t/T_{IS}}) e^{-t/T_{1\rho}^H} \quad \text{with } \lambda = T_{IS}/T_{1\rho}^H$$

Comparison with liquid-state ^{31}P NMR measurements carried out on the pure nucleotide at various pH allowed us to unequivocally assign the signal at -12.8 ppm to the phosphorus atom P_α in the α -phosphate group. The assignment of the remaining two signals corresponding to the γ - and β -phosphate group (P_γ and P_β), however, turned out to be more complicated since their chemical shift could be shown to be strongly pH-dependent in the liquid-state. Therefore, a rotational resonance experiment [Levitt *et al.*, 1990; Raleigh *et al.*, 1988; Feng *et al.*, 1999] was carried out on the crystalline samples in order to determine the distance between P_α and the other two phosphorus sites. The corresponding spectra are shown in Figure 4.11 and Figure 4.12.

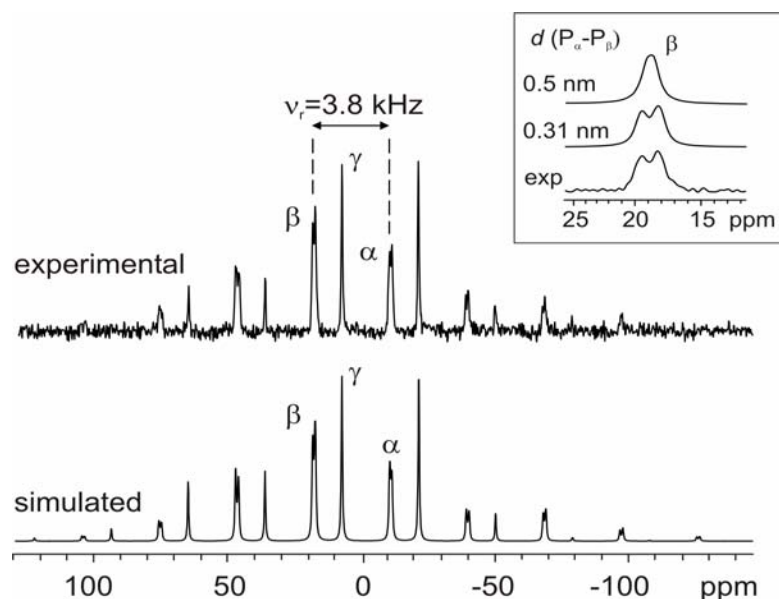


Figure 4.11 ^{31}P $\{^1\text{H}\}$ CP MAS NMR rotational resonance spectrum of Ras(wt)·Mg $^{2+}$ ·GppCH $_2$ p measured at 303 K (88 k scans). The $n = 1$ rotational resonance condition is fulfilled for the two signals at -12.8 and 18.8 ppm as indicated. The spectrum simulated for a P_α - P_β distance $d(\text{P}_\alpha$ - $\text{P}_\beta) = 0.31$ nm is shown at the bottom. The inset exhibits the signal at 18.8 ppm simulated for $d(\text{P}_\alpha$ - $\text{P}_\beta) = 0.5$ nm and 0.31 nm (top) as well as the experimental spectrum (bottom).

The isotropic chemical shift difference between P_α and the signal at 18.8 ppm amounts to 31.6 ppm which corresponds, in a magnetic field of $B_0 = 7.4$ T, to a frequency difference of 3841 Hz. In our experiments, n was set to 1. Therefore, the sample spinning rate was set to 3841 Hz. There are two major effects due to the reintroduction of the through-space ^{31}P - ^{31}P dipolar coupling. First, signals exhibit splittings or broadenings. Second, there is a rotor-driven exchange of longitudinal magnetization between spin sites. These two effects provide alternative routes for the estimation of the dipolar couplings, and hence internuclear distances. The direct observation of the spectral peakshape is simpler. The rotational resonance spectrum of Ras(wt)·Mg $^{2+}$ ·GppCH $_2$ p shows a doublet pattern. The distance between P_α and the phosphorus site giving rise to the signal at 18.8 ppm was determined by lineshape analysis using the SIMPSON software [Bak *et al.*, 2000]. It amounts to 0.31 ± 0.02 nm in agreement with the distance of 0.29 nm expected for the distance between P_α and P_β according to the X-ray structure [Brünger *et al.*, 1990].

In contrast, no signal splitting but a 50 Hz broadening (see Figure 4.12) is observed when the rotational resonance condition is fulfilled for the lines at -12.8 ppm (P_α) and at 7.3 ppm. The first rotational resonance condition being matched the sample spinning rate was set to 2440 Hz. By lineshape analysis, a distance of 0.5 ± 0.02 nm was determined in agreement

with the distance of 0.517 nm expected for the distance between P_α and P_γ according to the X-ray structure [Brünger *et al.*, 1990]. It is, therefore, concluded that the signal at 18.8 ppm must be due to P_β while the signal at 7.3 ppm is assigned to P_γ .

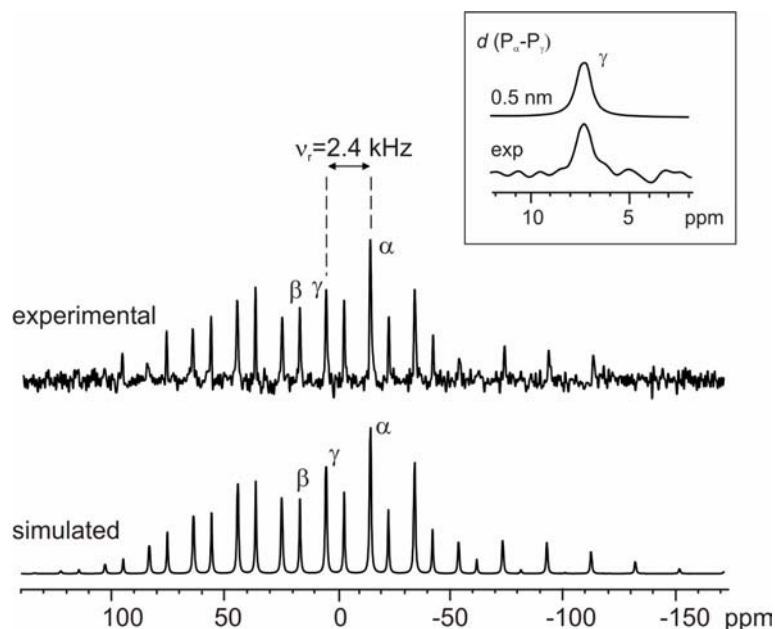


Figure 4.12 ^{31}P $\{^1\text{H}\}$ CP MAS NMR rotational resonance spectrum of Ras(wt)·Mg $^{2+}$ ·GppCH $_2$ p measured at 303 K. The $n = 1$ rotational resonance condition is fulfilled for the two signals at -12.8 and 7.3 ppm as indicated. The spectrum simulated for a P_α - P_γ distance $d(P_\alpha$ - $P_\gamma) = 0.5$ nm is shown at the bottom. The inset exhibits the signal at 7.3 ppm simulated for $d(P_\alpha$ - $P_\gamma) = 0.5$ nm (top) as well as the experimental spectrum (bottom). 52 k scans were acquired.

In order to prove that the assignment of the α -, β -, and γ - signals in the ^{31}P $\{^1\text{H}\}$ CP MAS NMR spectrum of Ras(wt)·Mg $^{2+}$ ·GppCH $_2$ p is correct, we employed the most common experiment to obtain homonuclear correlation spectra, i.e. the proton driven spin diffusion experiment [Szevereny *et al.*, 1982]. Spin diffusion is induced by the dipolar interaction of nuclear spins and leads to a transfer of magnetization between neighbouring spins by flip-flop processes which drive the involved spins towards thermal equilibrium. Because of the $1/r_{ij}^6$ distance dependence of the spin diffusion rate [Schmidt-Rohr *et al.*, 2001], magnetization transfer is restricted to close nuclei. In this spin diffusion 2D experiment, no radio frequency field is present during the mixing time on the proton channel. The 2D proton driven spin diffusion ^{31}P chemical shift correlation spectra of Ras(wt)·Mg $^{2+}$ ·GppCH $_2$ p is given in Figure 4.13. For a mixing time of 4 ms, cross-peaks appear between the peaks at -12.8 ppm and 18.8 ppm indicating a close vicinity of these nuclei and therefore an assignment of the latter peak to the β -phosphate group of GppCH $_2$ p. This is in agreement with the above-described rotational resonance experiments. The different intensities of the cross-peaks between the γ -

and β -phosphate signals and between α - and β -phosphate signals are to be expected. The reason is that the rate constant for spectral spin diffusion between two phosphorus sites having isotropic chemical shifts corresponding to δ_{1iso} and δ_{2iso} is proportional to $(\delta_{1iso} - \delta_{2iso})^{-2}$ [Suter *et al.*, 1982].

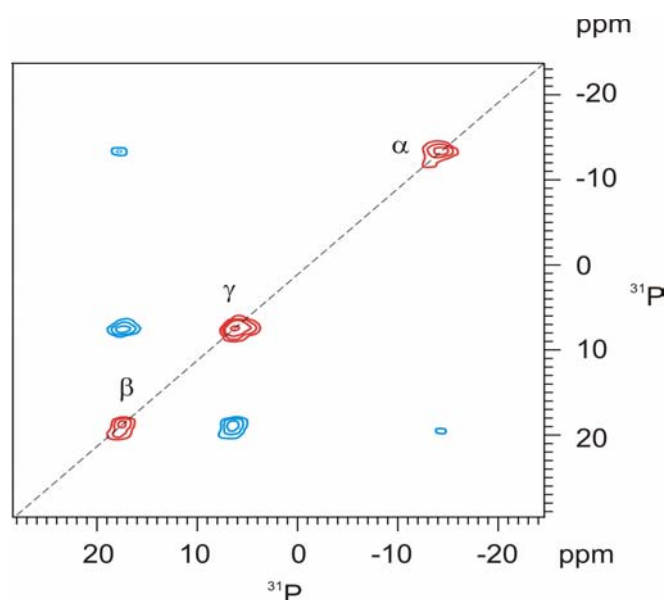


Figure 4.13 ^1H driven spin diffusion spectrum of Ras(wt)·Mg $^{2+}$ ·GppCH $_2$ p with a mixing time of 4 ms. The sample spinning rate was 10 kHz; recycle delay: 0.5 s; mixing time: 3 ms. 2200 scans were acquired for each of the 256 increments in t_1 .

Further evidence for the resonance assignment of the NMR spectra of Ras(wt)·Mg $^{2+}$ ·GppCH $_2$ p came from refocused INADEQUATE experiments [Lesage *et al.*, 1999]. Recently Fayon *et al.* [2002] demonstrated that an oxygen mediated J -coupling could be observed in solid-state NMR of inorganic phosphates. Liquid-state NMR of pure GppCH $_2$ p revealed values of 26 Hz and 8.9 Hz for $J(\text{P}_\alpha\text{-O-P}_\beta)$ and $J(\text{P}_\beta\text{-O-P}_\gamma)$ [Spoerner, *Biochemistry*, accepted]. These values are significantly smaller than the linewidth (50-60 Hz) and do, therefore, not lead to a doublet splitting in the 1D ^{31}P $\{^1\text{H}\}$ CP MAS spectra. Figure 4.14 shows the refocused INADEQUATE spectrum of crystalline Ras(wt)·Mg $^{2+}$ ·GppCH $_2$ p. The $\text{P}_\alpha\text{-O-P}_\beta$ connectivity is clearly indicated by two correlation peaks in the spectrum. In contrast, the $\text{P}_\beta\text{-O-P}_\gamma$ connectivity does not give rise to cross-peaks. This is due to the small efficiency of DQ coherence excitation for the small J -coupling value. The degree of conversion into DQ coherence is maximum for $\tau = 1/(4J)$, where 2τ is the delay under which ^{31}P magnetization evolves under the isotropic homonuclear J -coupling Hamiltonian [Lesage *et al.*, 1999]. Delays of 5 ms for Ras(wt)·Mg $^{2+}$ ·GppCH $_2$ p were employed as a compromise between the efficiency of excitation of the DQ coherence and the loss of signal due to relaxation during long delays.

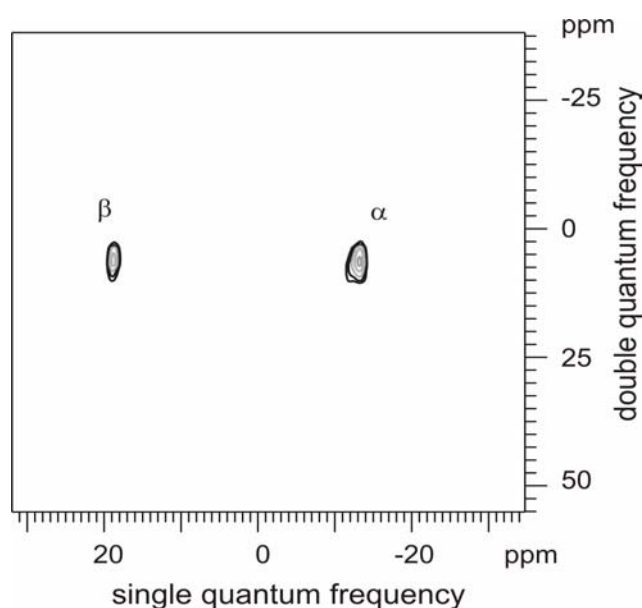


Figure 4.14 ^{31}P 2D refocused INADEQUATE spectrum of Ras(wt)·Mg $^{2+}$ ·GppCH $_2$ p at a sample spinning rate of 10 kHz. 64 increments (6900 scans each) were collected with a τ delay (synchronized with the sample spinning rate) set to 5 ms. Quadrature detection was achieved using the TPPI method. The recycle delay was 0.5 s and the CP mixing time was 3 ms.

Information about the internuclear distance between two spins can be deduced from the strength of the heteronuclear (^1H - ^{31}P) dipolar interaction. Having optimised the PMLG decoupled ^1H - ^{31}P LG-CP HETCOR experiment for phosphorylated amino acids, its application to Ras(wt)·Mg $^{2+}$ ·GppCH $_2$ p is straightforward. The 2D spectrum with the chemical shift of phosphorus nuclei in the direct dimension correlated with their dipolar coupled neighbouring protons in the indirect dimension is shown in Figure 4.15. The overall sensitivity is good, due to high sample spinning rate ($\omega_r/(2\pi) = 16$ kHz).

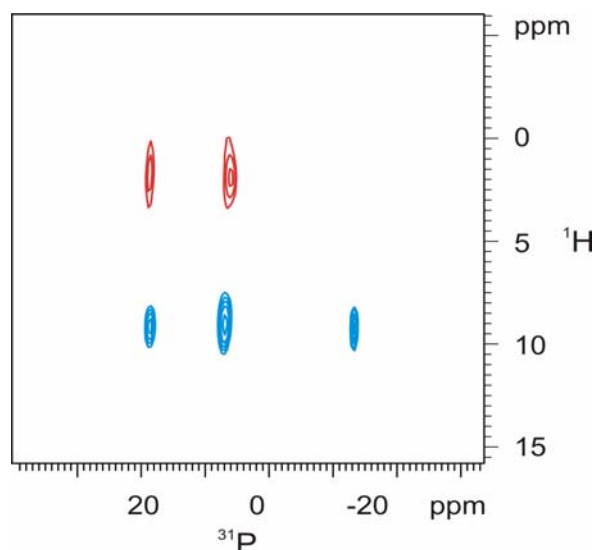


Figure 4.15 Contour plot of PMLG decoupled ^1H - ^{31}P LG-CP HETCOR spectrum of Ras(wt)·Mg $^{2+}$ ·GppCH $_2$ p recorded at a sample spinning rate of 16 kHz. The data were obtained with a LG-CP contact time of 2 ms and 128 t_1 increments (2300 scans each).

Two proton lines are resolved. The PMLG was performed very efficiently during t_1 . The limitation for obtaining spectra with a higher resolution for ^1H was the time required for such measurements and, therefore, the small number of points in t_1 . The detected correlations are due to ^1H nuclei closely neighbored to ^{31}P nuclei.

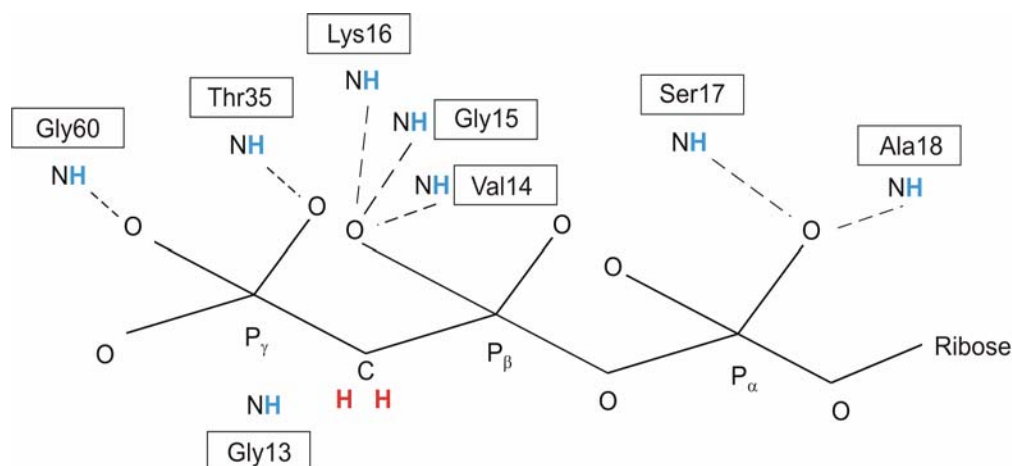


Figure 4.16 Schematic drawing of the nucleotide surrounded by several amino acid residues. ^1H nuclei of the several NH groups form hydrogen bonds with the phosphate groups of the nucleotide. These give rise to cross-peaks in the ^1H - ^{31}P LG-CP HETCOR spectrum of Ras(wt)·Mg $^{2+}$ ·GppCH $_2$ p.

Correlations between P_β and P_γ of Ras(wt)·Mg $^{2+}$ ·GppCH $_2$ p and protons are observed at 9 ppm and 2.2 ppm ^1H chemical shift. We assign the peak at 9 ppm to hydrogen bonded protons of the NH groups of the protein backbone with the phosphate groups. The 2.2 ppm peak is assigned to the ^1H nuclei of the CH $_2$ group of the GppCH $_2$ p nucleotide. P_α shows only one correlation peak with the hydrogen atoms of the NH group of the protein backbone (see Figure 4.16).

As shown in Figure 4.9, we have measured ^{31}P $\{^1\text{H}\}$ CP MAS NMR spectra of Ras(wt)·Mg $^{2+}$ ·GppCH $_2$ p at different temperatures. In Figure 4.17, only the central lines of the spectra are presented together with an image of the crystals used for our measurements. If the sample is cooled down to 273 K, the signals do not split into two or more components. However, the presence of the two different states, 1 and 2, in Ras(wt)·Mg $^{2+}$ ·GppCH $_2$ p could be shown by liquid-state ^{31}P NMR spectroscopy [Spoerner *et al.*, *Biochemistry*, accepted]. It is, therefore, assumed that the exchange between these two states is fast in the crystalline sample even at 273 K. Apart from the two biologically relevant states 1 and 2 which can be adopted by the molecule, four crystallographically inequivalent positions exist within the unit cell of the Ras(wt)·Mg $^{2+}$ ·GppCH $_2$ p crystals (see Figure 4.18). The crystallographically inequivalent molecules in Ras(wt)·Mg $^{2+}$ ·GppCH $_2$ p exhibit slightly different conformations of the effector loop for these various positions. This may lead to a distribution of the isotropic ^{31}P NMR chemical shift and occasionally to an exchange between the different conformations which complicates the study of the exchange process between the biologically relevant states 1 and 2.

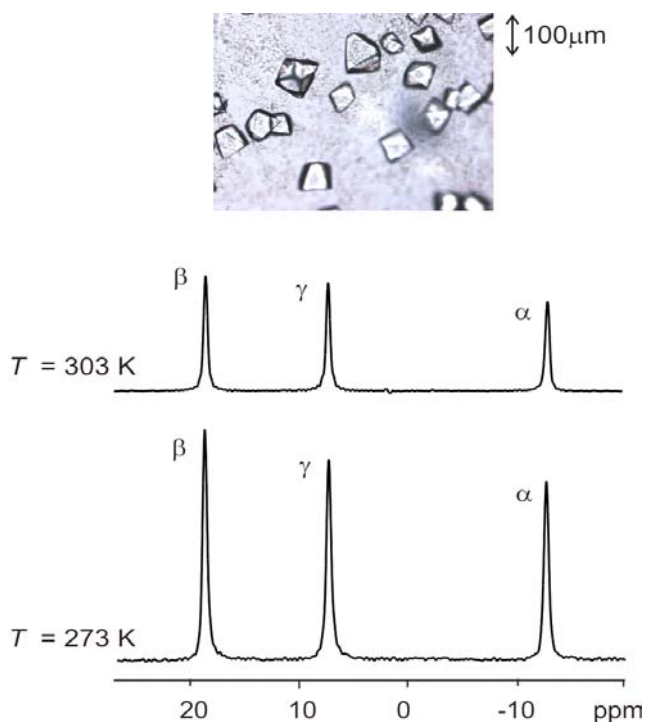


Figure 4.17 Central lines of ^{31}P $\{^1\text{H}\}$ CP MAS NMR spectra of Ras(wt)·Mg $^{2+}$ ·GppCH $_2$ p measured at 303 K and 273 K. The inset shows a microscopic image of characteristic microcrystallites used for our measurements.

This hypothesis is in line with the observation of an increasing residual linewidth (full width at half maximum) of the ^{31}P MAS NMR signals at decreasing temperature. If the temperature decreases from 303 K to 273 K, the lines broaden from 40 - 50 Hz up to 60 - 70 Hz (Table 4.5). This behaviour can be explained by the slowing rate of conformational exchange. Differences in the isotropic chemical shift are then no longer averaged out to zero which results in the observed line broadening.

T /K	linewidth / Hz		
	P $_{\alpha}$	P $_{\beta}$	P $_{\gamma}$
303	55	49	50
273	67	55	61

Table 4.5 Linewidth values of the signals corresponding to the α -, β -, and γ -phosphate group of Ras(wt)·Mg $^{2+}$ ·GppCH $_2$ p in ^{31}P $\{^1\text{H}\}$ CP MAS NMR spectra.

The ^{31}P NMR signals of crystalline proteins are broadened by two dominating internal magnetic interactions, namely the chemical shift anisotropy and the heteronuclear magnetic dipole-dipole-interaction between ^{31}P and neighbouring ^1H nuclei. These two interactions are effectively suppressed by the combined application of MAS and heteronuclear TPPM decoupling. The influence of the homonuclear magnetic dipole-dipole interaction [Raiford *et al.*, 1997] among the ^{31}P nuclei upon the residual linewidth can be assumed to be suppressed

as well since the ^{31}P - ^{31}P dipolar coupling constant of ca. 700 Hz corresponding to a ^{31}P - ^{31}P distance of ca. 0.3 nm is small compared to the applied sample spinning rates (6 or 10 kHz). The contribution of J -coupling to the residual linewidth is expected to be independent of the temperature within the considered temperature range. The distribution of the isotropic chemical shift (“static disorder”) must be assumed to be another major source of residual linewidth.

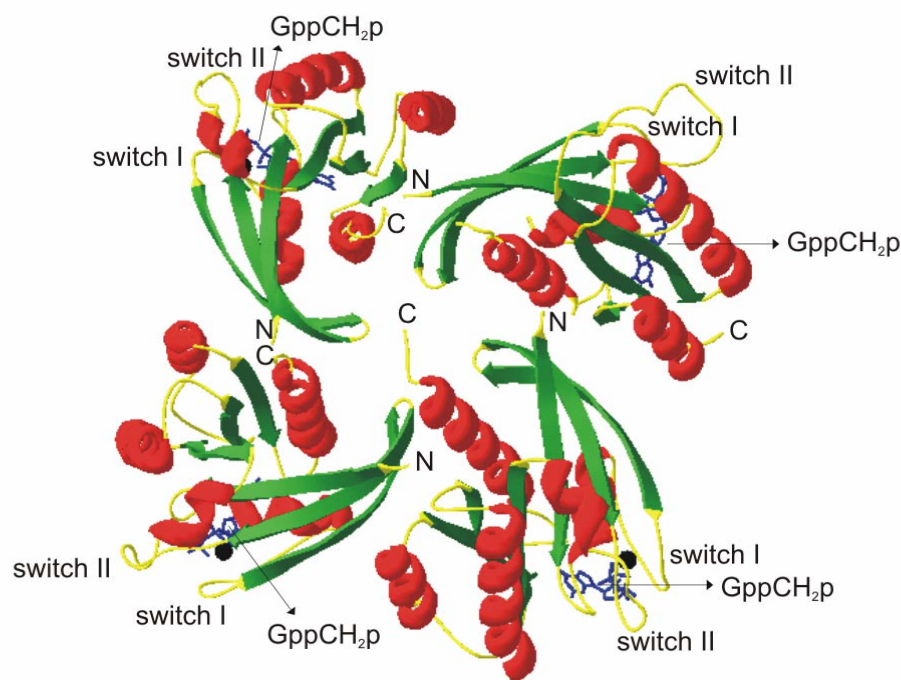


Figure 4.18 Ribbon plot of Ras(wt)·Mg²⁺·GppCH₂p with the switch regions as shown. The nucleotide is represented in blue, the Mg²⁺ ions are black balls. The N and C termini of the polypeptide chains are indicated.

The presence of rapid thermal motions such as conformational exchange in Ras(wt)·Mg²⁺·GppCH₂p is further corroborated by a pronounced temperature dependence of the CP build-up time, T_{1S} (Figure 4.10 and Table 4.6). T_{1S} shortens by about 50% if Ras(wt)·Mg²⁺·GppCH₂p is cooled down to 273 K. This behaviour indicates the presence of thermal motions in Ras(wt)·Mg²⁺·GppCH₂p which become slower and/or restricted in amplitude if the samples are cooled. Unfortunately, the samples cannot be cooled below 273 K since they have to be filled into the MAS rotor together with their mother liquor; a limitation which probably prevents us from resolving the different states in Ras(wt)·Mg²⁺·GppCH₂p. It must, therefore, be stated that the study of the exchange between the biologically relevant states 1 and 2 is complicated by the presence of other fast motions

(“dynamic disorder”), e.g., conformational exchange between the four different states in Ras(wt)·Mg²⁺·GppCH₂p microcrystals. If these thermal motions and exchange processes are fast on the NMR time scale, a narrow signal appears at the average chemical shift. Decreasing temperatures should then result in an increasing residual linewidth due to the slowing thermal motions and conformational exchange processes; a behaviour which was indeed observed (see above).

Figure 4.19 shows the 1D ³¹P {¹H} CP MAS solid-state NMR spectrum of Ras(wt) complexed with GppCH₂p at $\omega_r/(2\pi) = 6$ kHz and at room temperature together with its simulated spectrum. The spectrum presents even at this low sample spinning rate good resolution showing the three resonance lines corresponding to α -, β -, and γ -phosphate groups of the nucleotide.

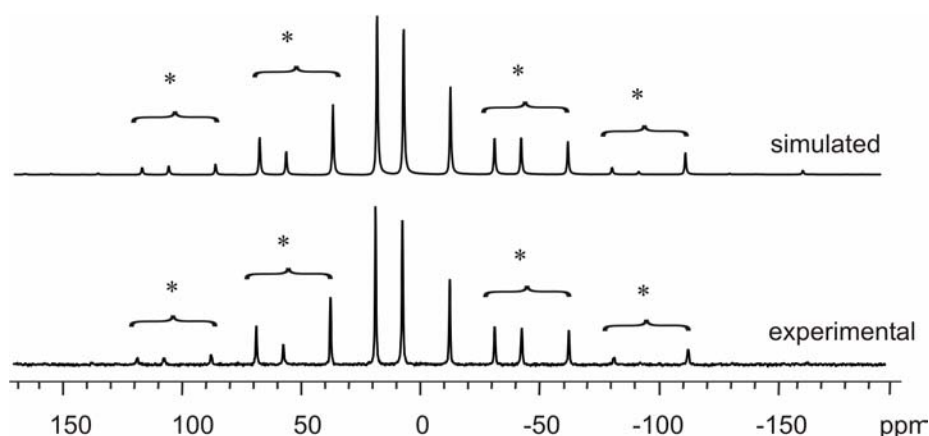


Figure 4.19 Experimental and simulated ³¹P {¹H} CP MAS NMR spectrum of Ras(wt)·Mg²⁺·GppCH₂p ($\omega_r/(2\pi) = 6$ kHz) at $T = 303$ K in the presence of TPPM decoupling applied to ¹H (160 k scans with a recycle delay of 0.5 s).

	$\delta_{\text{iso}} / \text{ppm}$ (± 0.1 ppm)	$\Delta\sigma / \text{ppm}$ (± 3 ppm)	η (± 0.1)	$T_{\text{IS}} / \mu\text{s}$ ($\pm 10\%$)	$T_{1\rho}^{\text{H}} / \text{ms}$ ($\pm 10\%$)
α (303 K)	-12.8	195	0.3	208	9
α (273 K)	-13.1	195	0.3	124	16
β (303 K)	18.8	114	1	104	13
β (273 K)	18.6	114	1	67	15
γ (303 K)	7.3	-124.5	0.2	133	11
γ (273 K)	7.2	-124.5	0.2	67	13.6

Table 4.6 NMR spectroscopic parameters of crystalline Ras(wt)·Mg²⁺·GppCH₂p measured at 303 K and 273 K.

The following convention is used: $\delta_{\text{iso}} = 1/3(\delta_{\text{xx}} + \delta_{\text{yy}} + \delta_{\text{zz}})$, $\Delta\sigma = 1/2(\delta_{\text{xx}} + \delta_{\text{yy}}) - \delta_{\text{zz}}$, $\eta = 3/2(\delta_{\text{xx}} - \delta_{\text{yy}})/\Delta\sigma$, $|\delta_{\text{zz}} - \delta_{\text{iso}}| > |\delta_{\text{xx}} - \delta_{\text{iso}}| > |\delta_{\text{yy}} - \delta_{\text{iso}}|$. Here, δ_{zz} , δ_{yy} , and δ_{xx} denote the principal values of the chemical shift tensor. T_{IS} and $T_{1\rho}^{\text{H}}$ were determined from the CP build-up curves.

Simulation of the spinning sideband patterns using the SIMPSON software allows to determine the values for the chemical shift anisotropy, $\Delta\sigma$, and the asymmetry parameter, η (see Table 4.6).

4.2.2 Ras Effector Loop Mutants in the GppCH₂p-Bound State

Ras in the GTP-bound form is able to bind to effector proteins. This binding is essential for the transmission of the signal to the nucleus. It was reported that the replacement of Gly12 by any other amino acid except for proline renders the protein oncogenic [Franken *et al.*, 1993]. Mutations of Gly12 are the most common oncogenic mutations in human tumors. They turn Ras into its oncogenic form since it loses its intrinsic as well as GAP accelerated activity. This results in a high concentration of Ras·GTP leading to a permanent, unregulated activation of the downstream targets and thus to an uncontrolled cell growth. Together with mutations of some other genes, the cell becomes transformed which finally results in tumor growth.

Throughout this thesis we focused our interest to two partial loss-of-function mutants: Ras(T35S) and Ras(T35A).

All known Ras genes encode an identical stretch of nine amino acids in the amino-terminal (amino acids 32-40) that undergoes a major conformational shift when Ras binds to GTP. Intriguingly, certain mutations in this region (called the effector loop) eliminate the ability of Ras to bind and activate known downstream effectors. Therefore, such mutants are useful to study the biological effect of suppressing one of the signal branches emerging from Ras. The effector loop mutations affect GTP binding and hydrolysis only slightly [Spoerner, Ph.D thesis]. It is generally believed that T35S activates the Raf initiated MAP kinase cascade [Herrmann *et al.*, 1996; Schmidt *et al.*, 2000] which leads to transcriptional activation but does not stimulate membrane ruffling and DNA synthesis [Joneson *et al.*, 1996]. T35S mutant, in the context of the activating mutation G12V in the mammalian cells, has an attenuated ability to induce foci, producing approximately 20-fold fewer foci per μg of DNA than Ras(G12V) alone [White *et al.*, 1995]. Akasaka *et al.* [1996] have demonstrated the responsibility of point mutations in the Ras effector loop to distinguish between different effectors. Here, significant differences in the recognition mechanism by which Raf, Byr2, and adenylyl cyclase associate with Ras were observed. The Ras mutant T35S was shown to have reduced affinity to RalGDS and Byr2 as well [Spoerner *et al.*, 2001].

The replacement of Thr35 in oncogenic Ras by alanine blocks the transformation [Herrmann *et al.*, 1994]. Ras(T35A) was pressure loaded into PC12 cells which can be induced to differentiate by oncogenic Ras. T35A did not induce neurite outgrowth. It was concluded that the protein is probably not oncogenic, because it has been shown that oncogenic transformation of fibroblasts and neurite induction in PC12 cells are always correlated [Sassone-Corsi *et al.*, 1989]. Furthermore, it was reported [Feig *et al.*, 1988] that T35A has no biological effect on NIH 3T3 cells.

Liquid-state ^{31}P NMR spectroscopy showed that the effector loop of the partial loss-of-function mutants T35S and T35A adopt a similar conformation as in state 1 of wild-type Ras while state 2 is not populated significantly. Since effector binding induces state 2, it most likely corresponds to a rather well defined conformation, where the OH of the Thr35 coordinates the Mg^{2+} ion while its methyl packs against the effector loop and where Tyr32 is close to the phosphates [Geyer *et al.*, 1996; Spoerner *et al.*, 2001].

4.2.2.1 Solid-State ^{31}P NMR Spectroscopy of Ras(T35S) $\cdot\text{Mg}^{2+}\cdot\text{GppCH}_2\text{p}$

The ^{31}P solid-state NMR spectrum of Ras(T35S) $\cdot\text{Mg}^{2+}\cdot\text{GppCH}_2\text{p}$ exhibits two resonance lines for the β -phosphate group (16.11 ppm and 17.31 ppm) and single sharp lines for the α - and γ -phosphate groups.

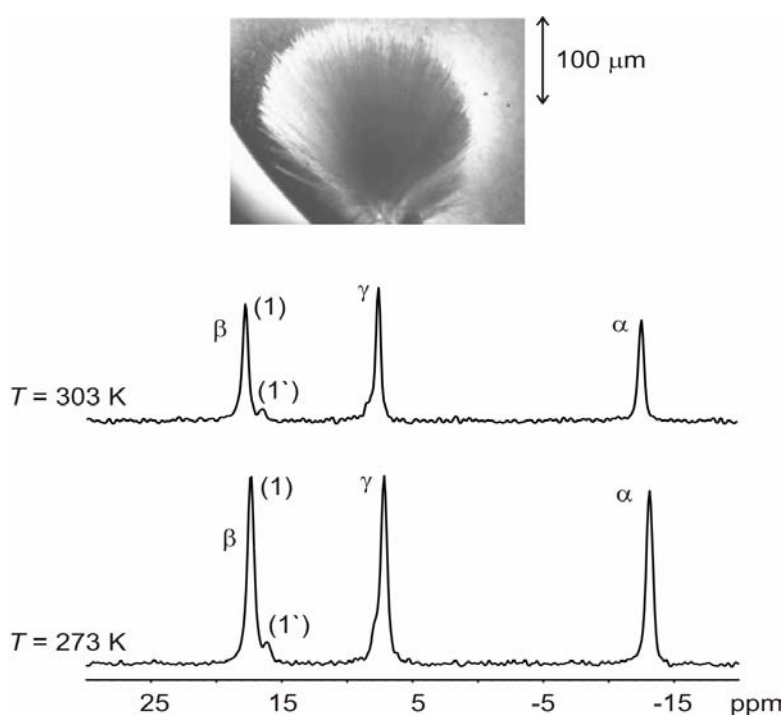


Figure 4.20 Top: Microscopic image of characteristic Ras(T35S) $\cdot\text{Mg}^{2+}\cdot\text{GppCH}_2\text{p}$ microcrystallites grown in a sitting drop. Bottom: ^{31}P $\{^1\text{H}\}$ CP MAS NMR spectra of Ras(T35S) $\cdot\text{Mg}^{2+}\cdot\text{GppCH}_2\text{p}$ measured at 303 K and 273 K. Only the central lines are shown.

The relative intensities of the two signals due to P_{β} behave like 1 : 10. In contrast to the behaviour of the signals due to states 1 and 2 in the wild-type protein, however, even an increase of the temperature up to 313 K does not result in fast exchange between the two states in Ras(T35S) (Figure 4.20).

The residual linewidth observed for Ras(T35S)·Mg²⁺·GppCH₂p at high temperature (61 Hz for α -, $\beta(1)$ -, and γ - resonance) is smaller than the linewidth at 273 K (85 Hz for α -, $\beta(1)$ -, and γ - resonance). This fact can be explained by the presence of internal motions of the protein molecule (“dynamic disorder”) of Ras(T35S)·Mg²⁺·GppCH₂p at room temperature. Decreasing temperatures should then result in an increasing residual linewidth due to the slowing thermal motions; a behaviour which was detected (as mentioned before). Ras(T35S)·Mg²⁺·GppCH₂p could be crystallized for the first time. X-ray diffraction on the complex was not yet performed.

Figure 4.21 shows the ³¹P {¹H} CP MAS spectra for 303 K and 273 K. The values for the chemical shift anisotropy and the asymmetry parameters along with the isotropic chemical shift values extracted from these spectra are given in Table 4.7.

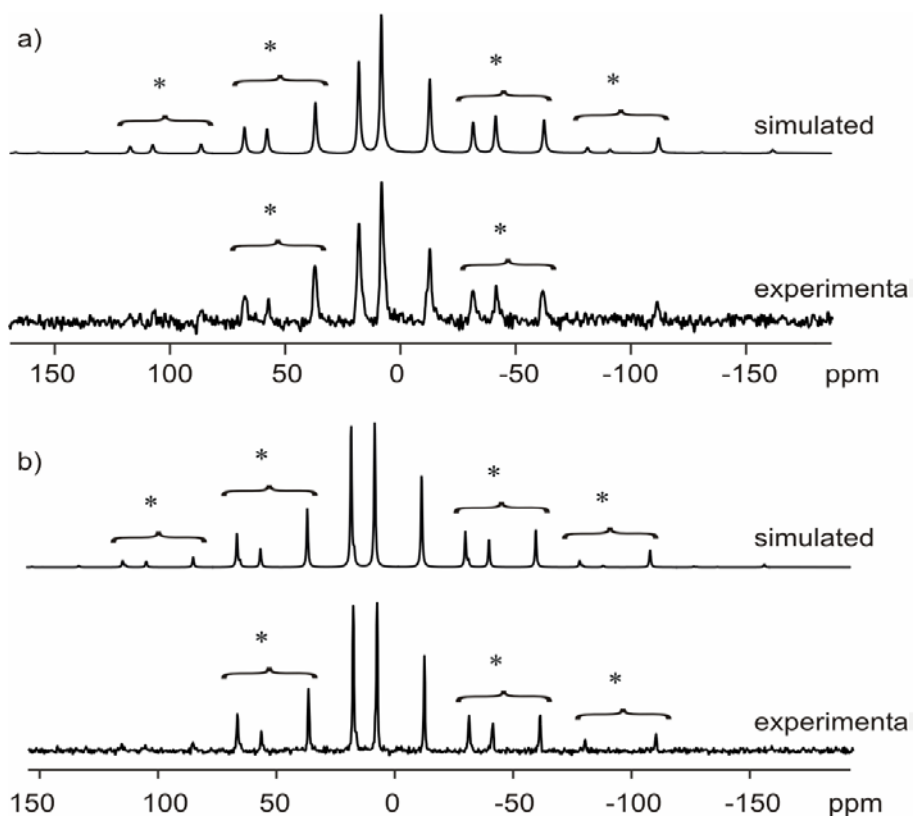


Figure 4.21 Simulated and experimental ³¹P {¹H} CP MAS NMR spectrum of Ras(T35S)·Mg²⁺·GppCH₂p measured at 303 K with 64 k scans (a) and at 273 K with 128 k scans (b).

The sample spinning rate was 6 kHz, the recycle delay was 0.5 s, and the cross-polarization mixing time was set to 3 ms.

		$\delta_{\text{iso}} / \text{ppm}$ ($\pm 0.1 \text{ ppm}$)	$\Delta\sigma / \text{ppm}$ ($\pm 3 \text{ ppm}$)	η (± 0.1)
α (303 K)		-12.6	180	0.6
α (273 K)		-13.1	171	0.7
β (303 K)	(1')	16.4	n.m.	n.m.
β (303 K)	(1)	17.8	-134	0.8
β (273 K)	(1')	16.1	-165	0.9
β (273 K)	(1)	17.3	-114	1
γ (303 K)		7.6	-125	0.4
γ (273 K)		7.2	-110	0.6

Table 4.7 NMR spectroscopic parameters of crystalline Ras(T35S) \cdot Mg²⁺ \cdot GppCH₂p measured at 303 K and 273 K. n.m. indicates that the corresponding values could not be measured.

4.2.2.2 Solid-State ³¹P NMR Spectroscopy of Ras(T35A) \cdot Mg²⁺ \cdot GppCH₂p

The T35A mutant, another partial loss-of-function mutant [White *et al.*, 1995], again shows single resonance lines for the α - and γ -phosphate groups. The signal of P _{β} splits into two lines at 17.31 ppm and 16.11 ppm. The ³¹P {¹H} CP MAS NMR spectra of Ras(T35A) \cdot Mg²⁺ \cdot GppCH₂p at different temperatures are shown in Figure 4.22.

The ³¹P {¹H} CP MAS NMR spectrum was acquired initially at room temperature. In order to find possible different conformations the spectrum was next acquired at low temperature. When the temperature was increased again, the initial spectrum was recovered, meaning that the protein was not denatured by cooling. The relative intensities of the two signals of the β -phosphate group behave like 1 : 12. This observation is in agreement with the liquid-state ³¹P NMR spectrum [Spoerner, unpublished results]. The mutant protein molecules preferentially exist in the "open" state 1 in the liquid-state. State 1 may represent a fixed conformation or an equilibrium of conformational substates in fast exchange on the NMR time scale. There is no information about different substates since we were the first to crystallize Ras(T35A) \cdot Mg²⁺ \cdot GppCH₂p. The residual linewidth observed for γ -phosphate of Ras(T35A) \cdot Mg²⁺ \cdot GppCH₂p at high temperature (61 Hz) is smaller than the linewidth at 273 K (85 Hz). The linewidth of the α - and β -phosphate group has the same value at low and high temperature (73 Hz). This would possibly indicate that γ -phosphate changes its position while the other phosphate groups remain unchanged. This supposition is sustained by the fact that in

state 1 the alanine residue replacing the Thr35 residue is no longer coordinated to the Mg^{2+} ion and that the hydrogen bond to the γ -phosphate group also does not exist.

Similar to the case of Ras(T35S) an increase of the temperature up to 313 K does not result in fast exchange between the two states in Ras(T35A) (Figure 4.22). The splitting of the P_γ -signal in Ras(T35S) and the splitting of the P_β -signal in Ras(T35A) may be due to intermolecular contacts. Another explanation would be the partial replacement of Mg^{2+} ions by Ca^{2+} . In contrast to the wild-type protein samples, the mutant protein crystallization necessarily requires the addition of $CaCl_2$ to the solution which may result in a partial exchange of Mg^{2+} by Ca^{2+} . Independent of this question and of the final assignment of the small signals at 16.1 ppm in both mutants, however, it can be stated that the conformational exchange between the biologically relevant states 1 and 2 observed in the wild-type protein does not occur for the effector loop mutants. The spectra of these mutants turned out to be temperature-independent in the considered range between 273 and 313 K. Within this context, it is also interesting to note that the habit of the crystallites is strongly influenced by the described effector loop mutations (see the characteristic microcrystallites photographs of Ras(T35S) and Ras(T35A) shown as insets in Figure 4.20 and Figure 4.22).

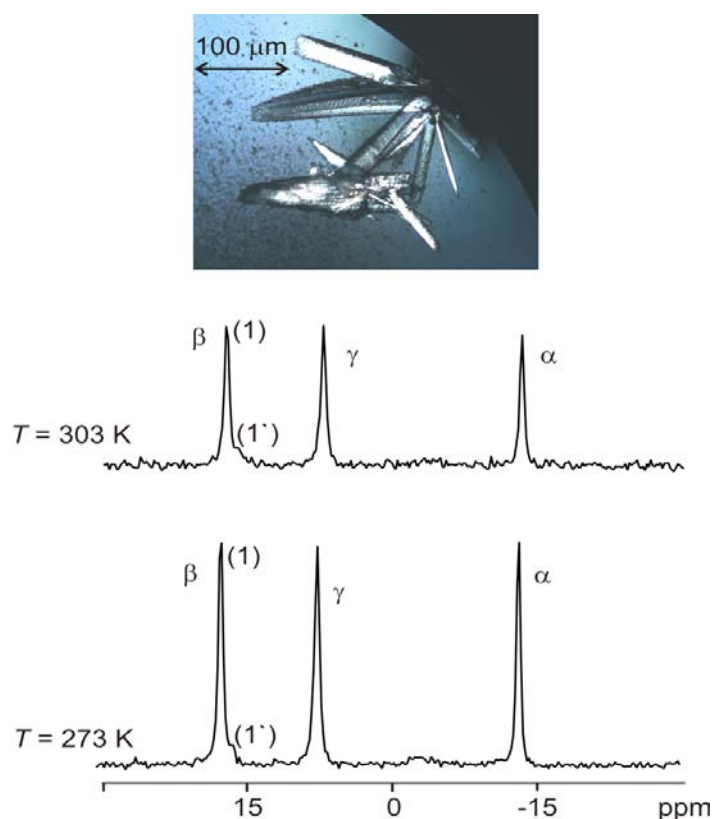


Figure 4.22 The microscopic image (top) of characteristic Ras(T35A)· Mg^{2+} ·GppCH₂p microcrystallites used for the solid-state ^{31}P $\{^1H\}$ CP MAS NMR measurements. ^{31}P $\{^1H\}$ CP MAS NMR spectra of Ras(T35A)· Mg^{2+} ·GppCH₂p measured at 303 K and 273 K. Only the central lines are shown.

By reducing the sample spinning rate in the ^{31}P $\{^1H\}$ CP MAS NMR experiment from 10 kHz used in the initial measurements to 6 kHz one obtained bigger intensities of the second order

spinning sidebands (Figure 4.23). The intensity of the spinning sidebands are related to the chemical shift anisotropy and provide an opportunity to recover the chemical shift parameter. They were obtained by lineshape simulation using the SIMPSON computer program and are given in Table 4.8.

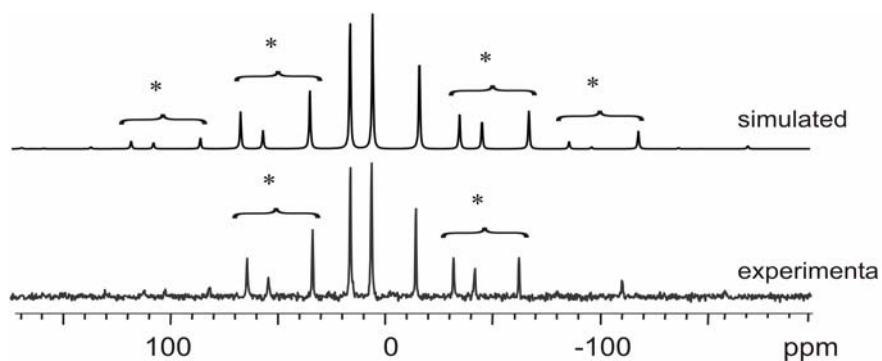


Figure 4.23 Simulated and experimental ^{31}P $\{^1\text{H}\}$ CP MAS NMR spectrum of Ras(T35A)·Mg $^{2+}$ ·GppCH $_2$ p at 273 K ($\omega_r/(2\pi) = 6$ kHz) in the presence of TPPM decoupling applied to protons. The signal is after 128 k scans with a recycle delay of 0.5 s.

	$\delta_{\text{iso}} / \text{ppm}$ (± 0.1 ppm)	$\Delta\sigma / \text{ppm}$ (± 3 ppm)	η (± 0.1)
α (303 K)	-13.2	171	0.6
α (273 K)	-13.4	n.m.	n.m.
β (303 K) (1')	16.1	n.m.	n.m.
β (303 K) (1)	17.3	-120	1
β (273 K) (1')	15.9	n.m.	n.m.
β (273 K) (1)	17.1	n.m.	n.m.
γ (303 K)	7.3	-110	0.2
γ (273 K)	7.3	n.m.	n.m.

Table 4.8 NMR spectroscopic parameters of crystalline Ras(T35A)·Mg $^{2+}$ ·GppCH $_2$ p measured at 303 K and 273 K. n.m. indicates that the corresponding values could not be measured.

In summary, solid-state ^{31}P NMR spectroscopy on mutants Ras(T35S) and Ras(T35A) showed that the mutant protein molecules preferentially exist in the "open" state 1 which makes the nucleotide more accessible to the interaction with water and other molecules in the crystallites. This is in agreement with ^{31}P liquid-state NMR spectra of Ras mutants which show that the equilibrium is shifted such that the mutants occur predominantly in the non-bonding conformation, namely state 1 (see Figure 4.24).

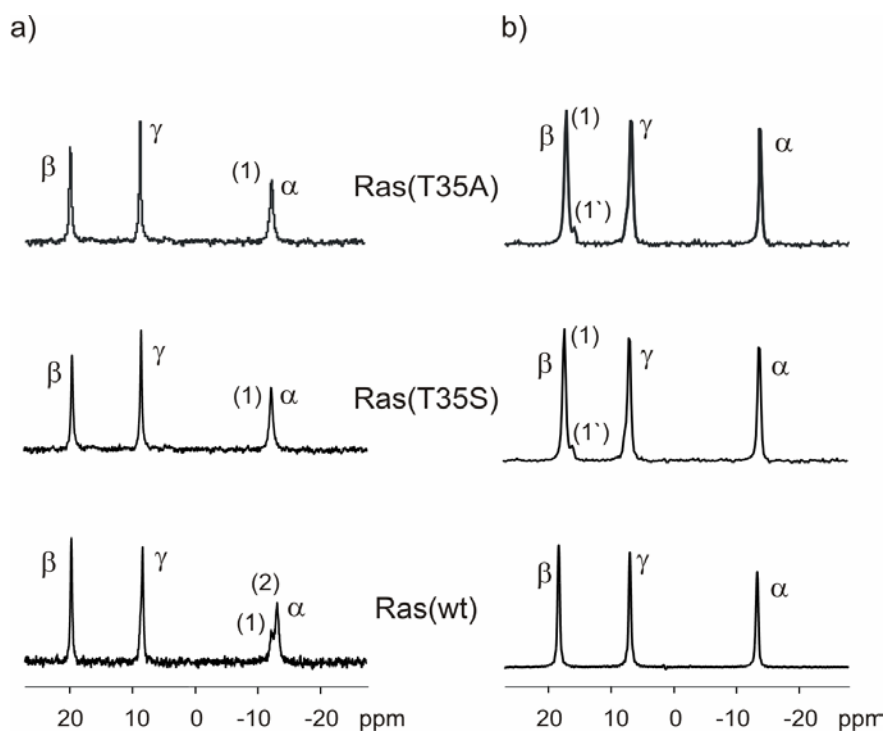


Figure 4.24 Liquid-state ^{31}P NMR (a) and solid-state ^{31}P $\{^1\text{H}\}$ CP MAS NMR spectra (b) of Ras(wt)·Mg $^{2+}$ ·GppCH $_2$ p and the effector loop mutants Ras(T35S)·Mg $^{2+}$ ·GppCH $_2$ p and Ras(T35A)·Mg $^{2+}$ ·GppCH $_2$ p measured at 273 K.

4.3 Solid-State ^{31}P NMR Spectroscopy of $\text{Ras}\cdot\text{Mg}^{2+}\cdot\text{GppNHp}$

4.3.1 Solid-State ^{31}P NMR Spectroscopy of $\text{Ras}(\text{wt})\cdot\text{Mg}^{2+}\cdot\text{GppNHp}$

Figure 4.25 shows the ^{31}P $\{^1\text{H}\}$ CP MAS NMR spectra of $\text{Ras}(\text{wt})\cdot\text{Mg}^{2+}\cdot\text{GppNHp}$ measured at a sample spinning rate of 10 kHz. At 303 K, the central line exhibits three well resolved signals at isotropic chemical shifts of -11.4, -3.3, and -0.2 ppm. The signals in the solid-state ^{31}P NMR spectra are of equal intensity if the spinning sidebands are added to the central lines as is expected.

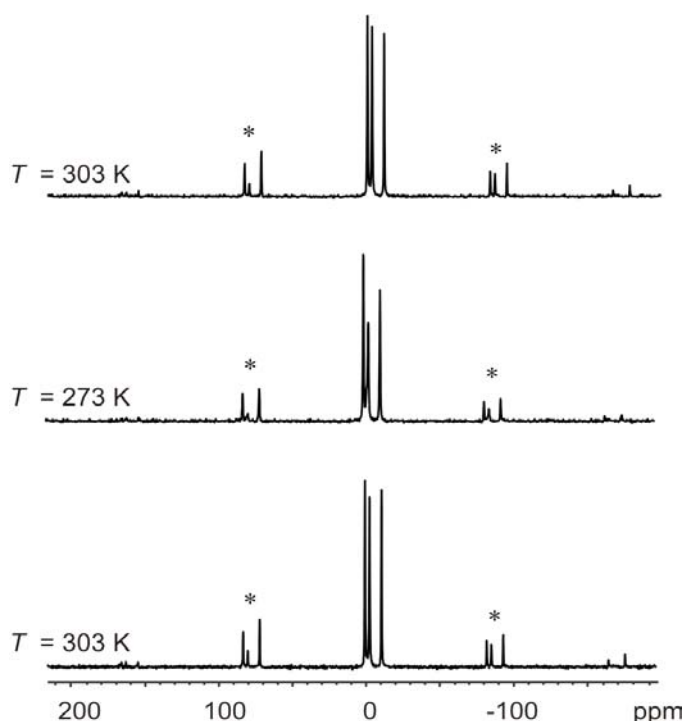


Figure 4.25 1D ^{31}P $\{^1\text{H}\}$ CP MAS NMR spectra of $\text{Ras}(\text{wt})\cdot\text{Mg}^{2+}\cdot\text{GppNHp}$ at different temperatures: Top: 303 K, Middle: 273 K, Bottom: 303 K (measured after cooling the sample to 273 K and heating it up to 303 K in order to show the reversibility of the sample cooling). Spinning side bands are marked with asterisks. The spectra (64 k scans) were recorded at 10 kHz sample spinning rate using TPPM decoupling. The recycle delay was 0.5 s and the cross-polarization mixing time was set to 2.8 ms.

As in the case of $\text{Ras}(\text{wt})\cdot\text{Mg}^{2+}\cdot\text{GppCH}_2\text{p}$, the signals corresponding to the β - and γ -phosphate group appeared to be strongly pH-dependent in the liquid-state. Therefore, extended experiments were carried out in order to assign the spectra properly. Proton driven spin diffusion experiments were carried out on the Ras protein for determining an accurate assignment of the β - and γ -phosphate group of the triphosphate nucleotide GppNHp complexed to the Ras protein. Figure 4.26 shows the 2D proton driven spin diffusion spectrum of $\text{Ras}(\text{wt})\cdot\text{Mg}^{2+}\cdot\text{GppNHp}$.

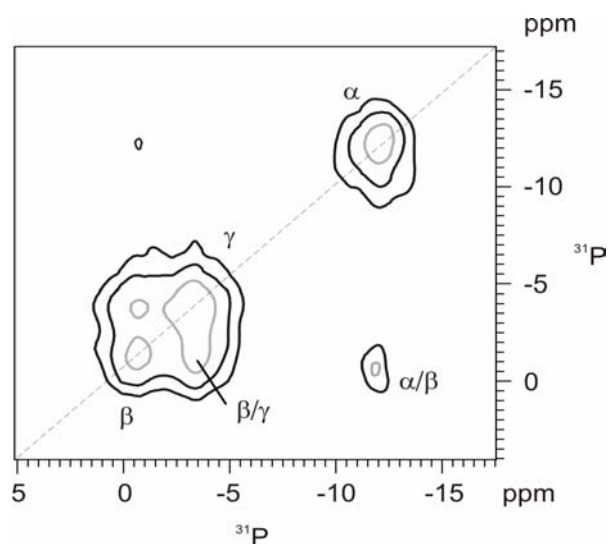


Figure 4.26 ^1H driven spin diffusion spectrum of Ras(wt) $\cdot\text{Mg}^{2+}\cdot\text{GppNHp}$ with a mixing time of 0.4 ms at a sample spinning rate of 10 kHz. The recycle delay was 0.5 s, mixing time was 3 ms. 2200 scans were acquired for each of the 256 increments in t_1 .

Cross-peaks originating from dipolar interactions between ^{31}P atoms appear for the peaks having isotropic chemical shifts of -11.4 ppm and -0.2 ppm and for the signals at -3.3 ppm and -0.2 ppm. The lack of cross-peaks between the resonances at -11.4 ppm and at -3.3 ppm indicate that the corresponding phosphate groups are not in close neighbourhood. Liquid-state NMR measurements unequivocally assigned the peak at -11.4 ppm to be due to the α -phosphate group. The assignment of the peak at -3.3 ppm to the γ -phosphate group is then straightforward. Therefore, the peak at -0.2 ppm must be due to P_β . The rate constant for spectral spin diffusion is known to be inversely proportional to the second power of the isotropic chemical shift difference [Suter *et al.*, 1982]. Therefore, β/γ cross-peaks are stronger than the α/β cross-peaks.

Furthermore, the 2D refocused INADEQUATE experiment was carried out in order to characterise Ras(wt) $\cdot\text{Mg}^{2+}\cdot\text{GppNHp}$. Figure 4.27 shows the refocused INADEQUATE spectrum of Ras(wt) $\cdot\text{Mg}^{2+}\cdot\text{GppNHp}$. This spectrum was acquired within a total experiment time of 39 h using a sample spinning rate $\omega_r/(2\pi) = 10$ kHz and a ^1H decoupling field strength $\omega_1/(2\pi) = 52$ kHz. The delay τ in which the ^{31}P magnetization evolved under the isotropic homonuclear J -coupling Hamiltonian was synchronized with the sample spinning rate. In this case the overall efficiency of an INADEQUATE sequence depends on the efficiency of excitation of the double quantum coherence, which periodically depends on τ , and on the decay of ^{31}P magnetization during the τ delays. Liquid-state NMR measurements on pure GppNHp nucleotide gave values of 20.7 Hz and 7.8 Hz for the coupling constants $J(\text{P}_\alpha\text{-O-P}_\beta)$ and $J(\text{P}_\beta\text{-O-P}_\gamma)$ [Spoerner, *Biochemistry*, accepted]. Since the coherence transfer is mediated by the scalar J -coupling an unambiguous identification of the through-bond connectivity peaks is straightforward. Thus, having the connectivity between P_α and the signal

at -0.2 ppm indicated by the two correlation peaks, the later signal could be assigned to the β -phosphate group of the GppNHp nucleotide in agreement with the ^1H driven spin diffusion experiment (see above). In contrast, the $\text{P}_\beta\text{-O-P}_\gamma$ connectivity does not give rise to correlation peaks. The reason is the small value of the $J(\text{P}_\beta\text{-O-P}_\gamma)$ coupling constant.

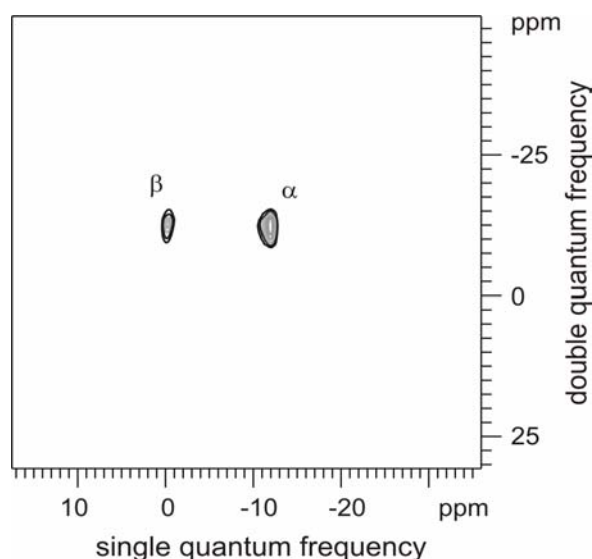


Figure 4.27 ^{31}P 2D refocused INADEQUATE spectrum of Ras(wt)·Mg $^{2+}$ ·GppNHp at a sample spinning rate of 10 kHz. A total of 64 increments with 7000 scans each were collected with a τ delay (synchronized with the sample spinning rate) set to 4 ms. The recycle delay was 0.5 s and the CP mixing time was 3 ms.

The reason for using refocused INADEQUATE instead of the 2D INADEQUATE was the higher sensitivity of the former experiment [Lesage *et al.*, 1999]. The reason for the higher sensitivity is the detection of in-phase peaks in contrast to the anti-phase lineshapes detected in the INADEQUATE spectrum.

In conclusion, the ^1H driven spin diffusion and refocused INADEQUATE experiments lead to the following assignment: P_α : -11.4 ppm, P_β : -0.2 ppm, and P_γ : -3.3 ppm. Note that the assignment of the signals at -3.3 ppm (P_γ) and -0.2 ppm (P_β) is different from the assignment of Reinstein *et al.* [1991] which was adopted in later publications [Geyer *et al.*, 1996; Spoerner *et al.*, 2001] as well as in an initial solid-state ^{31}P NMR study [Stumber *et al.*, 2002]. However, our new assignment is consistent with the results of a recent liquid-state ^{31}P NMR study of Ras(wt)·Mg $^{2+}$ ·GppNHp [Spoerner *et al.*, *Biochemistry*, accepted].

Heteronuclear correlation spectroscopy gives access to intramolecular correlations [van Rossum *et al.*, 1996]. There are several advantages of using ^1H - ^{31}P heteronuclear dipolar correlation spectroscopy. First, the gyromagnetic ratio for protons is 2.4 times larger than for phosphorus nuclei. Secondly, a distinction between intramolecular and intermolecular homonuclear ^{31}P coherence transfer is difficult due to rapid spin diffusion. For heteronuclear correlation spectroscopy, spin diffusion among protons can be suppressed effectively by the application of the PMLG ^1H homonuclear decoupling. Intermolecular heteronuclear

correlations involve the transfer of magnetization over distances up to 4 Å. This corresponds to a heteronuclear dipolar coupling of ~ 300 Hz and requires a relatively long transfer time. The ^1H resolution and the selectivity of the ^1H - ^{31}P transfer can be optimized effectively by applying fast spinning, LG decoupling during ^1H evolution, and CP. The heteronuclear correlation peaks provide structural information. Figure 4.28 shows the 2D PMLG decoupled ^1H - ^{31}P LG-CP HETCOR spectrum of Ras(wt)·Mg $^{2+}$ ·GppNHp using a sample spinning rate of 16 kHz. The LG-CP was adjusted to the $n = 1$ matching condition. The $n = 0$ condition should not be chosen since it results in a reduction of the effective heteronuclear dipolar interactions, which will lead to much less efficient polarization transfer.

It is clear from Figure 4.28 that the overall resolution (in both dimensions) is sufficient. P_β and P_γ show correlations with protons resonating at 8.7 ppm, 3.3 ppm, and 2.5 ppm. The cross-peak at 8.7 ppm is not completely resolved due to partial overlap of at least two peaks in the ^1H dimension. These two signals are attributed to hydrogen bonded protons of the NH groups of the amino acid residue with the phosphate groups and to the NH group of the GppNHp nucleotide (see Figure 4.29).

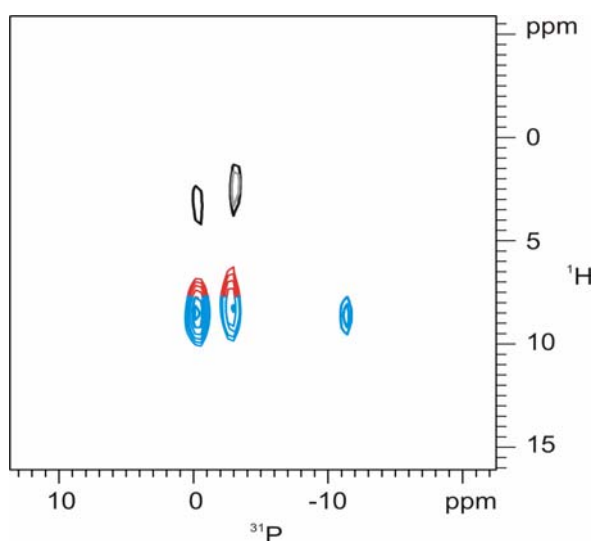


Figure 4.28 Contour plot of 2D PMLG decoupled ^1H - ^{31}P LG-CP HETCOR spectrum of Ras(wt)·Mg $^{2+}$ ·GppNHp recorded at a sample spinning rate of 16 kHz. The data were obtained with a LG-CP contact time of 2 ms and with 128 t_1 increments (2300 scans per increment).

The α -phosphate group exhibits a cross-peak to the protons resonating at 8.9 ppm indicating a magnetization transfer from the protons of the NH groups of the protein backbone to this phosphate group.

The cross-peaks of the 2D PMLG decoupled ^1H - ^{31}P LG-CP HETCOR spectrum of Ras(wt)·Mg $^{2+}$ ·GppNHp could easily be assigned due to the fact that proton chemical shifts were identified for the phosphorylated amino acids. In the 2D PMLG decoupled ^1H - ^{31}P LG-CP HETCOR spectra of P-Ser, P-Thr, and P-Tyr the peaks in between 10 ppm and 16 ppm in

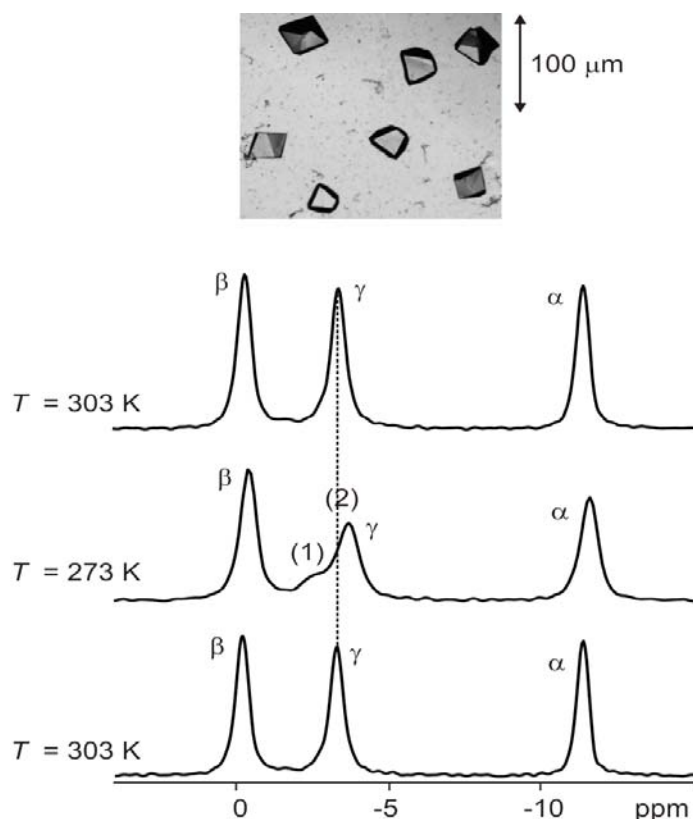


Figure 4.30 ^{31}P $\{^1\text{H}\}$ CP MAS NMR spectra of Ras(wt)·Mg $^{2+}$ ·GppNHp (central lines) measured at 303 K and 273 K. The bottom spectrum was measured at 303 K after cooling down the sample to 273 K in order to show the reversibility of the effects observed at low temperatures. The inset shows a microscopic image of characteristic microcrystallites used for the solid-state NMR measurements.

An image of characteristic microcrystallites used for the solid-state NMR spectroscopic studies is also shown (see inset). At 303 K, three well resolved signals are observed at isotropic chemical shifts of -11.4, -3.3, and -0.2 ppm as already described above. If the samples are cooled down to 273 K, the signal due to P_γ splits into two signals at -2.4 ppm and -3.6 ppm. In state 2 (-3.6 ppm), hydrogen bonds are formed between the γ -phosphate group and amino acid residues Thr35 and Gly60. These hydrogen bonds do probably not exist in the "open" state 1 (-2.4 ppm). The structural differences between states 1 and 2 obviously give rise to changes in the electronic environment of P_γ resulting in a chemical shift difference of 1.2 ppm between states 1 and 2. It should be noted that the ^{31}P NMR chemical shift of phosphates is influenced by various structural parameters such as the P-O-P bond angle and the P-O bond strengths [Cheatham *et al.*, 1986; Sternberg *et al.*, 1990] which may be different for states 1 and 2. The intensity ratio between the two signals corresponding to the "open" state 1 and state 2, respectively, amounts to 1 : (2.5 \pm 0.5). That means, the wild-type protein molecules preferentially exist in state 2. The signal due to P_α is broadened from about 60 Hz at 303 K to 85 Hz at 273 K while the signal due to the P_β remains almost unchanged. This behaviour is in striking analogy with the observations made for the liquid-state (see Figure 4.31 and Geyer *et al.*, 1996).

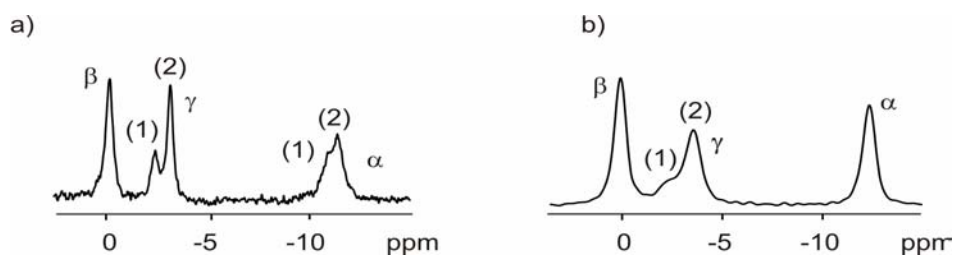


Figure 4.31 Liquid-state ^{31}P NMR (a) and solid-state ^{31}P $\{^1\text{H}\}$ CP MAS NMR spectra (b) of Ras(wt)·Mg $^{2+}$ ·GppNHp at 273 K.

Our observations also agree well with the initial solid-state NMR spectroscopic studies carried out by Stumber *et al.* [2002]. However, the quality of the spectra shown in Figure 4.25 and Figure 4.30 is considerably improved compared to spectra of Stumber *et al.* [2002]. Most likely, this progress is due the optimised experimental conditions, especially the use of an efficient heteronuclear decoupling sequence (TPPM, [Bennet *et al.*, 1995]) and an improved crystallisation procedure. It should be noted within this context that the solid-state ^{31}P NMR spectra were measured with a similar amount of sample (ca. 20 – 30 mg) and with the same acquisition time as the liquid-state ^{31}P NMR spectrum shown in Figure 4.31. The repetition time for the solid-state NMR experiments is limited by T_1^{H} of the ^1H nuclei due to the application of the CP technique. In contrast, the repetition time of the liquid-state NMR experiments is determined by the much longer T_1^{P} of ^{31}P . The corresponding gain in repetition time and in sensitivity due to the cross-polarization [Pines *et al.*, 1972] from ^1H to ^{31}P results in the excellent signal-to-noise ratio of the solid-state ^{31}P NMR spectra which even exceeds that of the liquid-state spectra. It is also important to note that the spectral resolution of the solid-state NMR spectra is comparable with that of the liquid-state NMR spectra. The residual linewidth (full width at half maximum) observed in the solid-state ^{31}P NMR spectra amounts to ca. 60 – 70 Hz while the liquid-state NMR spectra exhibit residual linewidths of ca. 30 – 40 Hz.

α		β	γ	
$\delta_{\text{iso1}} / \text{ppm}$	$\delta_{\text{iso2}} / \text{ppm}$	$\delta_{\text{iso}} / \text{ppm}$	$\delta_{\text{iso1}} / \text{ppm}$	$\delta_{\text{iso2}} / \text{ppm}$
-11.15	-11.85	-0.3	-2.69	-3.41

Table 4.9 Liquid-state ^{31}P NMR isotropic chemical shifts of Ras(wt)·Mg $^{2+}$ ·GppNHp at 273 K.

The chemical shift values observed in the crystalline state (see text above) agree perfectly with the chemical shift values measured in the liquid-state ^{31}P NMR spectra of Ras(wt)·Mg $^{2+}$ ·GppNHp (Table 4.9).

That means, crystallisation does not cause measurable chemical shift changes for Ras(wt)·Mg $^{2+}$ ·GppNHp. The two signals observed for P $_{\gamma}$ at 273 K merge into one single signal at 303 K. It is, therefore, concluded that the molecules switch fast between states 1 and 2 (conformational exchange). At 273 K, this exchange is slow on the NMR time scale while the exchange becomes fast at 303 K. Since the two signals are, however, not well enough resolved even at 273 K, the determination of the exchange rate by conventional lineshape analysis in analogy to Geyer *et al.* [1996] would lead to relatively large experimental errors. Nevertheless, the exchange rate can roughly be estimated according to the equation $\Delta\omega\tau_C \sim 1$ which describes the situation of intermediate exchange present at ca. 278 K. Here, $\Delta\omega$ denotes the angular frequency difference between the two signals which amounts to 923 s $^{-1}$ ($\Delta\nu = 147$ Hz) and τ_C is the correlation time, i.e. the inverse exchange rate. From this consideration we derive an exchange rate of ca. 900 s $^{-1}$, i.e. a correlation time of ca. 1 ms at 278 K. This value is close to the rate observed in solution; an observation which raises the question why these two different states could not be observed by X-ray crystallography. A possible explanation would be the assumption that state 1 exhibits dynamic disorder which prevents its X-ray crystallographic detection.

A striking difference between Ras(wt)·Mg $^{2+}$ ·GppCH $_2$ p and Ras(wt)·Mg $^{2+}$ ·GppNHp is observed for the temperature-dependence of the CP build-up times. As seen before, T_{IS} shortens by about 50% if Ras(wt)·Mg $^{2+}$ ·GppCH $_2$ p is cooled down to 273 K. In contrast, the CP build-up time is almost independent of temperature for Ras(wt)·Mg $^{2+}$ ·GppNHp.

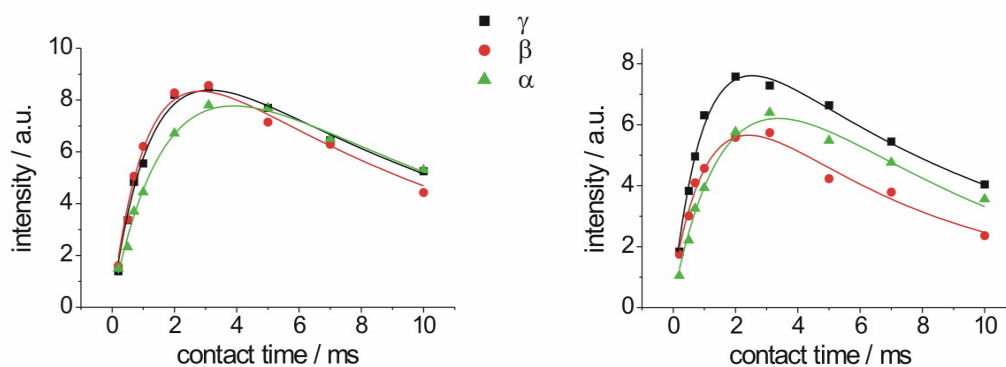


Figure 4.32 Variation of the α, β, γ ^{31}P $\{^1\text{H}\}$ cross-polarization MAS signals, I_{CP} , of Ras(wt)·Mg $^{2+}$ ·GppNHp at $T = 303$ K (left) and $T = 273$ K (right) as function of contact time. The solid lines represent a fit to the equation:

$$I_{CP} \sim (1 - \lambda)^{-1} (1 - e[-(1 - \lambda)t/T_{IS}]) e(-t/T_{1\rho}^H) \text{ with } \lambda = T_{IS}/T_{1\rho}^H$$

	$T_{IS} / \mu\text{s}$ ($\pm 10\%$)	$T_{1\rho}^{\text{H}} / \text{ms}$ ($\pm 10\%$)
α (303 K)	169	10.1
α (273 K)	171	5.6
β (303 K)	120	10.9
β (273 K)	111	9.0
γ (303 K)	108	9.9
$\chi(1)$ (273 K)	n.m.	n.m.
$\chi(2)$ (273 K)	198	6.7

Table 4.10 Values of the CP build-up times and rotating frame spin-lattice relaxation times as determined from the CP build-up curves of Ras(wt)·Mg²⁺·GppNHp at 303 K and 273 K.

This is an interesting effect: The described conformational exchange between states 1 and 2 is significantly slowed down upon cooling the samples from 303 K down to 273 K. Since the CP build-up time is almost independent of the temperature within this range it is concluded, that the nucleotide does not move relative to the rest of the molecule while the switch regions change their conformation.

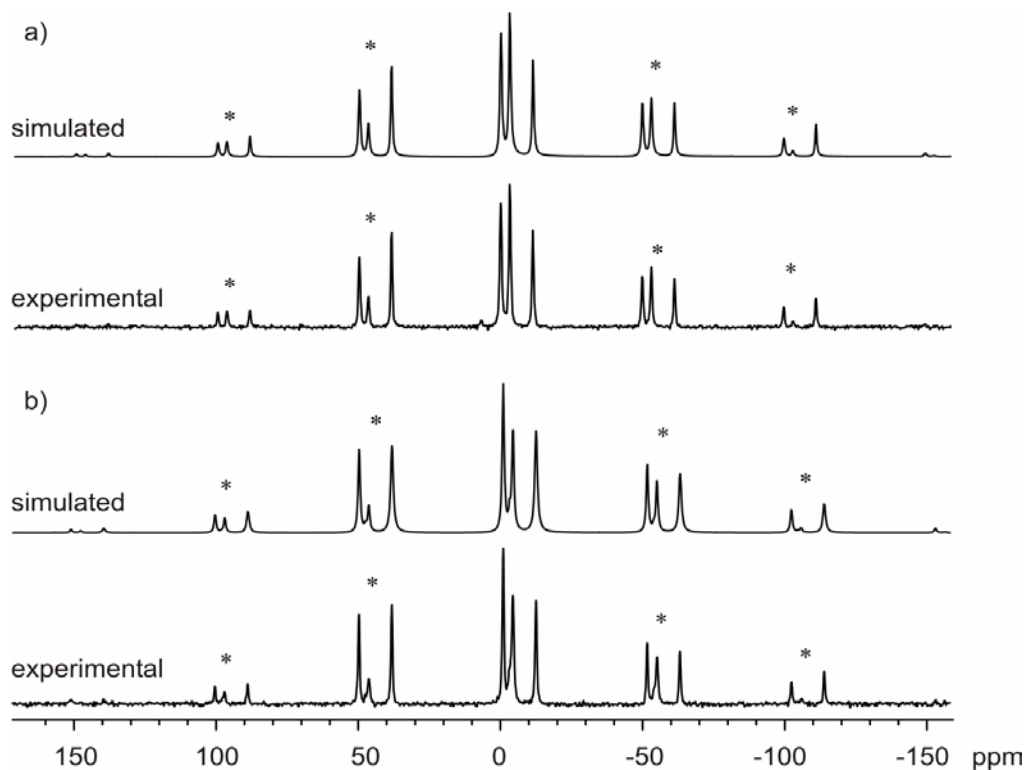


Figure 4.33 Simulated and experimental ³¹P {¹H} CP MAS NMR spectrum of Ras(wt)·Mg²⁺·GppNHp measured at 303 K (a) and 273 K (b). Sample spinning rate: 6 kHz, 64 k scans, 0.5 s recycle delay, 2.8 ms cross-polarization mixing time.

Information about the chemical shift anisotropy can be extracted from the spinning sideband pattern obtained under slow magic angle spinning (see Table 4.11). The experimental 1D ^{31}P $\{^1\text{H}\}$ CP MAS solid-state NMR spectra of Ras(wt)·Mg $^{2+}$ ·GppNHp measured at 303 K and 273 K with a sample spinning rate of 6 kHz together with the simulated spectra are given in Figure 4.33.

	$\delta_{\text{iso}} / \text{ppm}$ ($\pm 0.1 \text{ ppm}$)	$\Delta\sigma / \text{ppm}$ ($\pm 3 \text{ ppm}$)	η (± 0.1)
α (303 K)	-11.4	188	0.6
α (273 K)	-11.6	195	0.7
β (303 K)	-0.2	160	0.8
β (273 K)	-0.3	165	0.8
γ (303 K)	-3.3	-147	0.3
χ (1) (273 K)	-2.4	-135	0.8
χ (2) (273 K)	-3.6	-147	0.3

Table 4.11 NMR spectroscopic parameters of crystalline Ras(wt)·Mg $^{2+}$ ·GppNHp measured at 303 K and 273 K.

4.3.2 Effector Loop Mutants of Ras in the GppNHp-Bound State

Recently, it has become clear that Ras uses more than one pathway to mediate the downstream response [Vojtek *et al.*, 1998]. Different mutants of Ras in the effector loop region are supposed to be specifically blocked in a particular pathway. Such partial loss-of-function mutants can be used to mark the specific downstream signalling components of a particular pathway [White *et al.*, 1995; Akasaka *et al.*, 1996; Rodriguez-Viciana *et al.*, 1997]. It was suggested that the combination of partial loss-of-function restores biological activity. However, Schmidt *et al.* [2000] have demonstrated that none of the combinations of two point mutations restore the biological activity to a higher extent. Only a triple combination was shown to restore 50% of the activity. This confirms the fact that all commonly used partial loss-of-function mutations have reduced affinities to the different effectors. This makes it unlikely that the combination of mutants would fully restore the pathways and, thus, the biological function. Table 4.12 shows that the affinity of Ras(T35S)·Mg $^{2+}$ ·GppNHp to Raf is decreased by a factor of 60 and to RalGDS by a factor of 100. Binding to AF6 and Byr2 is affected as well [Spoerner *et al.*, 2001]. The absolute affinity of wild-type Ras to Raf is much higher than to the other effectors, which explains the observation that T35S appears to selectively activate the Raf pathway *in vivo*.

Ras variant	Effector	$K_D / \mu\text{M}$
Ras(wt)·Mg ²⁺ ·GppNHp	Raf	0.02
	RalGDS	1.0
	AF6	3.0
	Byr2	0.3
Ras(T35S)·Mg ²⁺ ·GppNHp	Raf	1.2
	RalGDS	>100
	AF6	>100
	Byr2	3.7
Ras(T35A)·Mg ²⁺ ·GppNHp	Raf	3.4

Table 4.12 Interaction of Ras(wt), Ras(T35S), and Ras(T35A) with different effectors (see [Spoerner *et al.*, 2001]). K_D is the dissociation constant of the complexes between the Ras proteins and several effectors.

Table 4.12 shows also the affinity of T35A to the various effectors. Replacing Thr35 in Ras by an alanine residue leads to a further reduction of the affinity to Raf by a factor of almost three compared with the T35S mutant.

4.3.2.1 Solid-State ³¹P NMR Spectroscopy of Ras(T35S)·Mg²⁺·GppNHp

As it was shown before, the switch I region of Ras wild-type in the GppNHp-bound state adopts two conformations that can be detected by ³¹P NMR spectroscopy. Figure 4.34 exhibits the ³¹P {¹H} CP MAS NMR spectra of crystalline Ras(T35S)·Mg²⁺·GppNHp. Ras(T35S) also shows single signals for the α -phosphate (-9.7 ppm) and β -phosphate (-0.3 ppm) groups. Two peaks are seen for the γ -phosphate (-1.8 ppm and -2.9 ppm). The relative intensities of the two signals due to P _{γ} behave like 3 : 1 in Ras(T35S). In contrast to the behaviour of the signals due to states 1 and 2 in the wild-type protein, however, even an increase of the temperature up to 313 K does not result in fast exchange between these two states. This observation is in agreement with the liquid-state ³¹P NMR spectra (see Figure 4.34). The mutant protein molecules preferentially exist in the "open" state 1 in solution. The same seems to be true in the crystalline state which makes the nucleotide accessible for interactions with water and may allow additional intermolecular contacts within the unit cell.

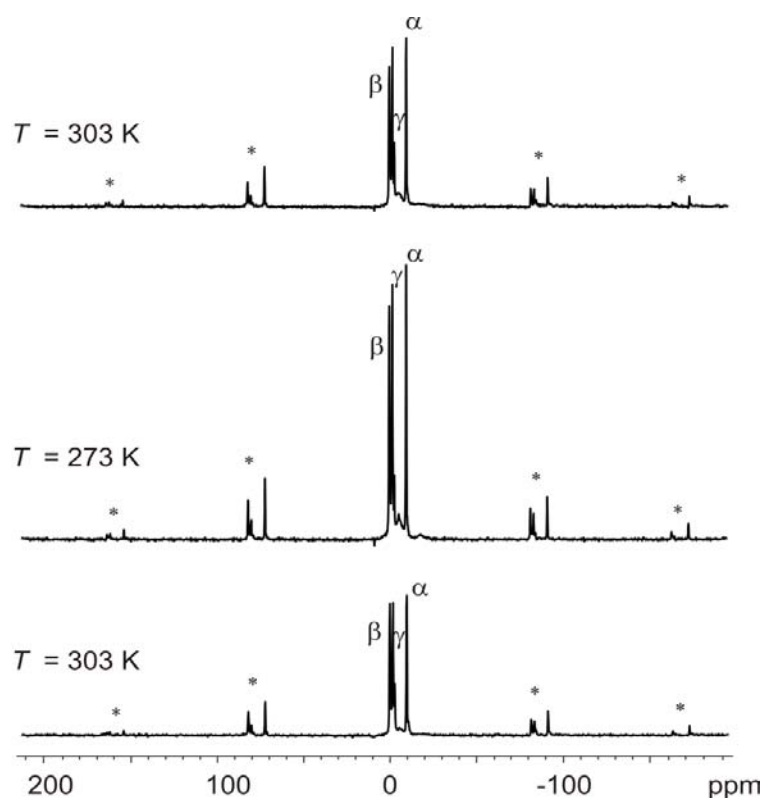


Figure 4.34 1D ^{31}P $\{^1\text{H}\}$ CP MAS spectra of Ras(T35S)·Mg $^{2+}$ ·GppNHp at different temperatures. The bottom spectrum was detected after cooling the sample down to 273 K and heating it up again to 303 K in order to show the reversibility. Spinning side bands are marked with asterisks. The central lines marked with α , β , and γ correspond to the α -, β -, and γ -phosphate groups of the GppNHp nucleotide. The spectra (128 k scans) were recorded at 10 kHz sample spinning rate using TPPM decoupling. The recycle delay was 0.5 s and the cross-polarization mixing time was set to 2.8 ms.

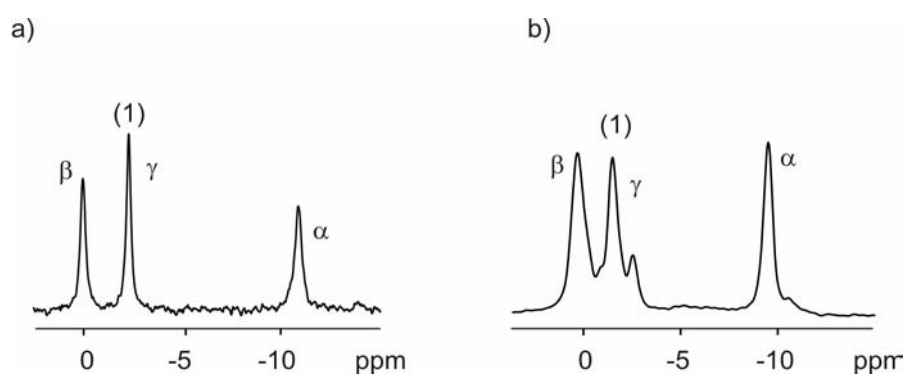


Figure 4.35 Liquid-state ^{31}P NMR (a) and solid-state ^{31}P $\{^1\text{H}\}$ CP MAS NMR spectra (b) of Ras(T35S)·Mg $^{2+}$ ·GppNHp at 273 K.

In contrast to the wild-type protein, pronounced crystallisation-induced chemical shift changes are observed for the mutant. A distinct chemical shift difference is observed between the liquid-state and the crystalline state especially for P $_{\alpha}$ (see Table 4.13). As mentioned

before, this is explained by the fact that the equilibrium in the mutant in the GppNHp-bound form is shifted such that it occurs predominantly in the non-binding conformation (state 1).

	a) $\delta_{\text{iso}} / \text{ppm}$ ($\pm 0.1 \text{ ppm}$)	b) $\delta_{\text{iso}} / \text{ppm}$ ($\pm 0.1 \text{ ppm}$)
α (273 K)	-9.7	-11.1
β (273 K)	-0.3	-0.27
γ (1) (273 K)	-1.8	-2.57
γ (1') (273 K)	-2.9	

Table 4.13 ^{31}P NMR isotropic chemical shift values of Ras(T35S)·Mg $^{2+}$ ·GppNHp in a) solid-state and b) liquid-state at 273 K. γ (1') represents the P $_{\gamma}$ resonance line at -2.9 ppm of crystalline Ras(T35S)·Mg $^{2+}$ ·GppNHp.

An expanded view of the 1D ^{31}P $\{^1\text{H}\}$ CP MAS spectra of Ras(T35S)·Mg $^{2+}$ ·GppNHp is given in Figure 4.36.

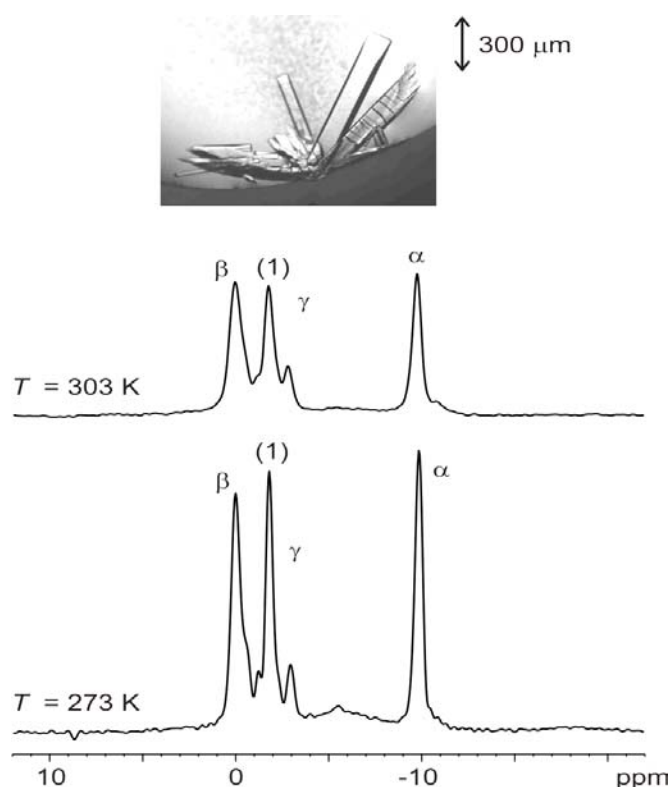


Figure 4.36 The microscopic image (top) of characteristic Ras(T35S)·Mg $^{2+}$ ·GppNHp microcrystallites used for the solid-state NMR measurements. ^{31}P $\{^1\text{H}\}$ CP MAS NMR spectra of Ras(T35S)·Mg $^{2+}$ ·GppNHp measured at 303 K and 273 K. Only the central lines are shown.

X-ray crystallography on Ras(T35S) showed that the asymmetric unit cell contains three molecules. The nucleotide is located in similar position and exhibits basically the same contacts like in the wild-type protein. In all three T35S molecules the switch I and switch II regions are disordered. The “invisibility” of these regions indicates either static or dynamic disorder in the crystals. The missing electron density of switch I and switch II in the X-ray

structure of Ras may be due to the existence of different conformations around the γ -phosphate group since the mutant protein molecules preferentially exist in the "open" state 1 which makes the nucleotide more accessible to the interaction with other molecules in the crystallites.

The small signals at -5.5 ppm and -1.2 ppm are due to minor amounts of free GppNHp nucleotide. Since the P_γ lines do not merge into one resonance at high temperature it was concluded that the splitting of the P_γ signal may be due to intermolecular contacts (see above). Another explanation would be that the nucleotide is complexed with Mg^{2+} ions in one of the states and with Ca^{2+} ions in the other state since the Ras(T35S)· Mg^{2+} ·GppNHp crystallization necessarily requires the addition of $CaCl_2$ to the solution which results in a partial exchange of Mg^{2+} by Ca^{2+} . Liquid-state NMR experiments on the same sample have confirmed this assumption. Within this context, it is also interesting to note that the habit of the crystallites is strongly influenced by the described partial loss-of-function mutation. For a comparison between wild-type Ras crystallites and Ras(T35S) crystallites see Figure 4.30 and Figure 4.36.

The 1D ^{31}P $\{^1H\}$ CP MAS NMR spectrum of Ras(T35S)· Mg^{2+} ·GppNHp at 6 kHz sample spinning rate and at room temperature is given in Figure 4.37.

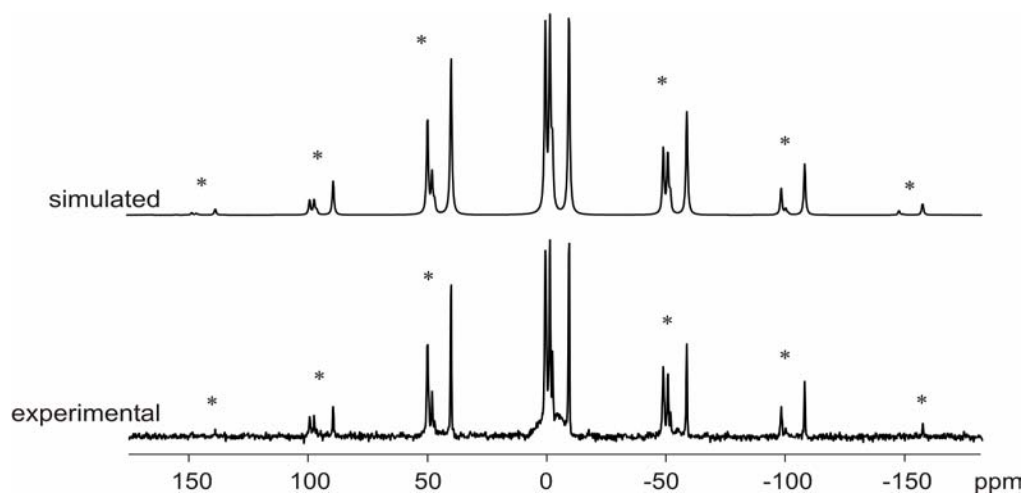


Table 4.37 Simulated and experimental ^{31}P $\{^1H\}$ CP MAS NMR spectrum of Ras(T35S)· Mg^{2+} ·GppNHp measured at 303 K. The sample spinning rate was 6 kHz, the number of scans was 128 k, the recycle delay was 0.5 s, and the cross-polarization mixing time was set to 2.8 ms.

Simulation of the spinning sideband pattern of the 1D ^{31}P $\{^1H\}$ CP MAS NMR spectrum using the SIMPSON software allowed us to determine the chemical shift anisotropy, $\Delta\sigma$, and the asymmetry parameter, η (see Table 4.14).

	$\Delta\sigma$ / ppm (± 3 ppm)	η (± 0.1)
α (303 K)	188	0.6
β (303 K)	159	0.6
$\gamma(1)$ (303 K)	-134	0.4
$\gamma(2)$ (303 K)	-131	0.3

Table 4.14 NMR spectroscopic parameters of crystalline Ras(T35S) \cdot Mg²⁺ \cdot GppNHp measured at 303 K.

The values given in Table 4.14 indicate that P _{α} nuclei experience the largest chemical shift anisotropy. The CSA of P _{γ} resonances have negative signs. The values for the chemical shift anisotropy of Ras(T35S) \cdot Mg²⁺ \cdot GppNHp are similar to the values of CSA of Ras(wt) \cdot Mg²⁺ \cdot GppNHp at room temperature (see also Table 4.11). The comparison between the value for the asymmetry parameter of P _{β} of Ras(T35S) \cdot Mg²⁺ \cdot GppNHp and Ras(wt) \cdot Mg²⁺ \cdot GppNHp indicates a smaller deviation from axial symmetry in the first case. Therefore, from comparison between NMR spectroscopic parameters of crystalline Ras(T35S) \cdot Mg²⁺ \cdot GppNHp and Ras(wt) \cdot Mg²⁺ \cdot GppNHp it appears that the local geometry at the nucleotide site is similar in these two cases.

In conclusion, the replacement of Thr35 by Ser perturbs the equilibrium of the conformational states and, possibly, also the rate of interconversion of these conformations, and thereby also effect interactions with target proteins. Thr35, being invariant in all Ras-like (and other) GTP-binding proteins, is thus apparently conserved not for structural but rather for the dynamic properties of these switch molecules. While a Thr \rightarrow Ser mutation should be tolerated from structural considerations, the results presented here indicate that the methyl group of this residue is important for the capability of Ras to dynamically switch between different conformations. This residue has been mutated not only in Ras but also in other Ras-like proteins [Bae *et al.*, 1998; Mott *et al.*, 1999] and it was found to be important for the proteins' function and dynamics of the switch regions.

4.3.2.2 Solid-State ³¹P NMR Spectroscopy of Ras(T35A) \cdot Mg²⁺ \cdot GppNHp

The binding of GTP to Ras is strongly influenced by the T35A mutation. The ratio of affinities for GDP and GTP is 4-fold for T35A [John *et al.*, 1993]. This means that the mutant protein binds GDP more strongly than GTP. The slow intrinsic GTPase activity of Ras(T35A) is reduced to 23% of the wild-type value. The mutation also influences the affinity of the Ras protein for GAP. Ras(T35A) shows drastically decreased affinity for GAP.

It was shown that the structure of the effector region in the structure of Ras is regulated by the coordination of Thr35 to Mg^{2+} [Pai *et al.*, 1990]. X-ray crystallography on Ras(T35S)· Mg^{2+} ·GppNHp found that the effector region is extremely mobile because of the loss of the methyl group of Thr35. This effect would be more pronounced for Ras(T35A)· Mg^{2+} ·GppNHp which has lost its hydroxyl group as well. Therefore, the ^{31}P NMR spectrum of Ras(T35A)· Mg^{2+} ·GppNHp is expected to have only one resonance line each for the α -, β -, and γ -phosphate group.

The 1D ^{31}P $\{^1H\}$ CP MAS NMR spectrum of crystalline Ras(T35A)· Mg^{2+} ·GppNHp is given in Figure 4.38 at different temperatures.

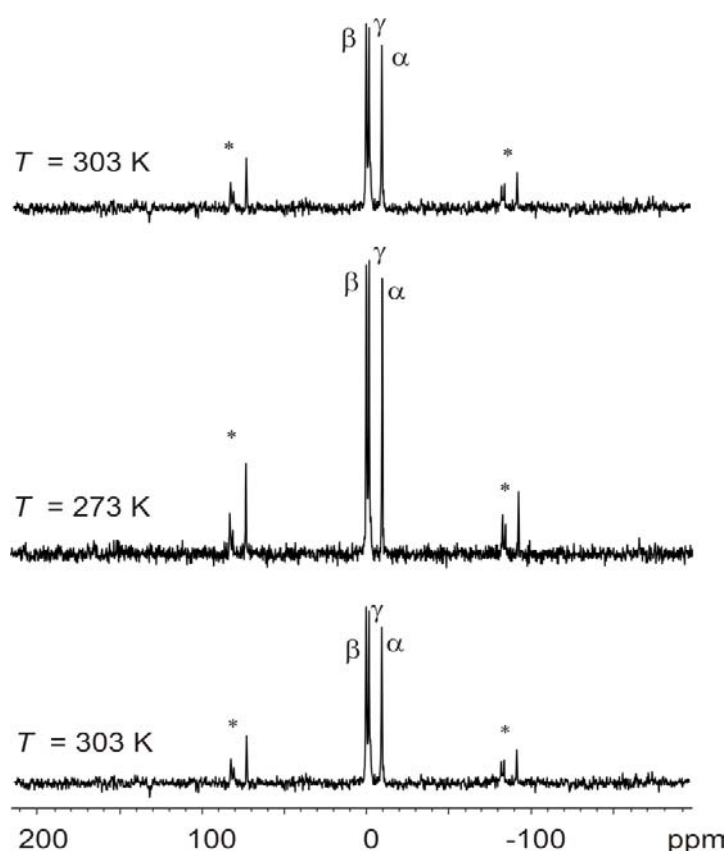


Figure 4.38 1D ^{31}P $\{^1H\}$ CP MAS spectra of Ras(T35A)· Mg^{2+} ·GppNHp at different temperatures. Spinning side bands are marked with asterisks. The central lines, marked with α , β , and γ correspond to the α -, β -, and γ -phosphate group of the GppNHp nucleotide. The spectra (256 k scans) were recorded at 10 kHz sample spinning rate using TPPM decoupling. The recycle delay was 0.5 s and the cross-polarization mixing time was set to 2.8 ms.

As already pointed out above, the dynamic equilibrium of the switch region is of major importance for the function of Ras and its interaction with effectors. Ras(T35A) obviously prefers state 1, i.e. its non-bonding conformation rather than state 2, as can be seen from the spectra. Similar to liquid-state ^{31}P NMR experiments, solid-state ^{31}P NMR showed that the replacement of the residue Thr35 by alanine resulted in the stabilisation of the "open" state 1.

Figure 4.39 exhibits the liquid-state ^{31}P NMR spectra of Ras(T35A)· Mg^{2+} ·GppNHp and - for comparison - again the spectrum of crystalline Ras(T35A)· Mg^{2+} ·GppNHp.

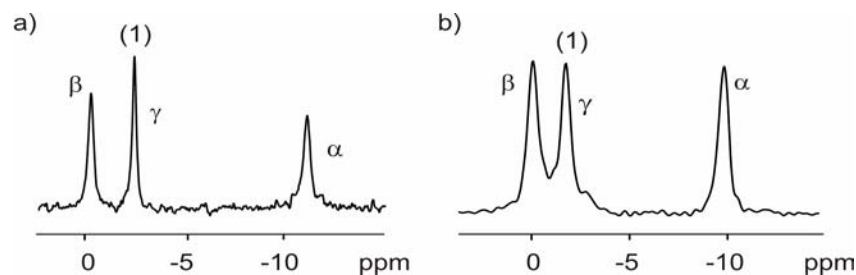


Figure 4.39 Liquid-state ^{31}P NMR (a) and solid-state ^{31}P $\{^1\text{H}\}$ CP MAS NMR spectra (b) of Ras(T35A)·Mg $^{2+}$ ·GppNHp at 273 K.

A distinct chemical shift difference is observed between the liquid-state and the crystalline state for the P_α line (liquid-state: $\delta_{\text{iso}}(\text{P}_\alpha) = -11.9$ ppm; solid-state: $\delta_{\text{iso}}(\text{P}_\alpha) = -9.8$ ppm). Responsible for the above-described chemical shift change are crystallization-induced interactions already observed for the T35S mutant.

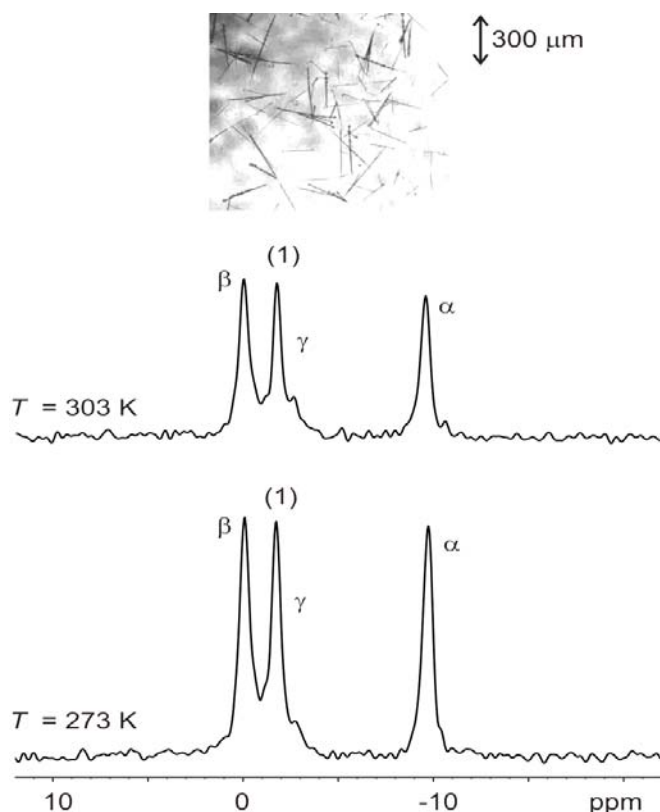


Figure 4.40 Microscopic image (top) of characteristic Ras(T35A)·Mg $^{2+}$ ·GppNHp microcrystallites used for the solid-state NMR measurements. ^{31}P $\{^1\text{H}\}$ CP MAS NMR spectra of Ras(T35A)·Mg $^{2+}$ ·GppNHp measured at 303 K and 273 K. Only the central lines are shown.

The stabilisation of the state 1 in Ras(T35A) is clearly shown in Figure 4.40 which contains only the central band of the 1D ^{31}P $\{^1\text{H}\}$ CP MAS NMR spectrum of Ras(T35A)·Mg $^{2+}$ ·GppNHp at different temperatures. The signal of P_γ splits into two lines at -1.8 ppm and -2.8 ppm. The relative intensities of these two signals behave like 4 : 1. An increase in temperature, however, does not lead to a coalescence of the two P_γ lines in analogy to the behaviour of Ras(T35S). Again, a possible explanation for the observation of the two

states could be that the nucleotide is complexed with Mg^{2+} in one state and with Ca^{2+} in the other state since $CaCl_2$ is required for the $Ras(T35A) \cdot Mg^{2+} \cdot GppNHp$ crystallization. Another possibility is the existence of intermolecular contacts in the crystalline state. Liquid-state NMR experiments on the same sample are in line with this assumption since complexation with Ca^{2+} leads to a shift of about 1 ppm for P_γ . On the other hand, initial experiments show that an increasing fraction of the nucleotide is released from the protein molecules at raising Ca^{2+} exchange degree. Independent of this question and of the final assignment of the small signal at -2.8 ppm in the mutant, however, it can be stated that the conformational exchange between the biologically relevant states 1 and 2 observed in the wild-type protein does not occur for the effector loop mutants. The spectra of these mutants turned out to be temperature independent in the considered range between 273 and 313 K. It was observed that the habit of the effector loop mutants crystallites is very different from the wild-type crystallites (see Figure 4.40, Figure 4.36, and Figure 4.30).

The 1D $^{31}P \{^1H\}$ CP MAS NMR spectrum of $Ras(T35A) \cdot Mg^{2+} \cdot GppNHp$ at a sample spinning rate of 6 kHz and at 303 K is given in Figure 4.41.

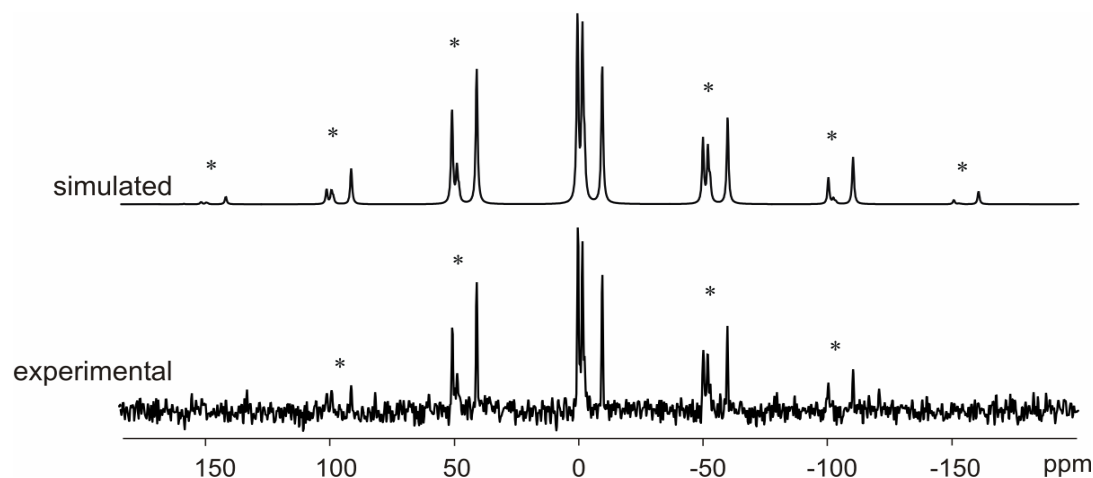


Figure 4.41 Simulated and experimental $^{31}P \{^1H\}$ CP MAS NMR spectrum of $Ras(T35A) \cdot Mg^{2+} \cdot GppNHp$ measured at 303 K. The sample spinning rate was 6 kHz, the number of scans was 280 k, the recycle delay was 0.5 s, and the cross-polarization mixing time was set to 2.8 ms.

Chemical shift anisotropy parameters can be accurately extracted with the SIMPSON simulation program from the spinning sideband pattern of the experimental spectrum showed above. Table 4.15 shows the ^{31}P NMR data of $Ras(T35A) \cdot Mg^{2+} \cdot GppNHp$. The chemical shift anisotropy, $\Delta\sigma$, and the asymmetry parameter, η of $Ras(T35A) \cdot Mg^{2+} \cdot GppNHp$ are equivalent with the chemical shift anisotropy parameters of $Ras(T35S) \cdot Mg^{2+} \cdot GppNHp$ (compare Table 4.14 and Table 4.15). This means that the $GppNHp$ nucleotide in both mutants experience

approximately the same environment and, furthermore, the local geometry of the nucleotide site is the same as in Ras(wt)·Mg²⁺·GppNHp.

	$\delta_{\text{iso}} / \text{ppm}$ ($\pm 0.1 \text{ ppm}$)	$\Delta\sigma / \text{ppm}$ ($\pm 3 \text{ ppm}$)	η (± 0.1)
α (303 K)	-9.6	188	0.6
α (273 K)	-9.8	-	-
β (303 K)	-0.1	159	0.6
β (273 K)	-0.1	-	-
γ (1) (303 K)	-1.8	-134	0.4
γ (2) (303 K)	-2.7	-131	0.3
γ (1) (273 K)	-1.8	-	-
γ (2) (273 K)	-2.8	-	-

Table 4.15 ³¹P NMR spectroscopic parameters of crystalline Ras(T35A)·Mg²⁺·GppNHp at 303 K.

4.4 Solid-State ^{31}P NMR Spectroscopy of Ras·Mg $^{2+}$ ·GTP γ S

Ras(wt), Ras(T35A), and Ras(T35S) in complex with Mg $^{2+}$ and the GTP γ S nucleotide could be crystallized as well (see Figure 4.42).

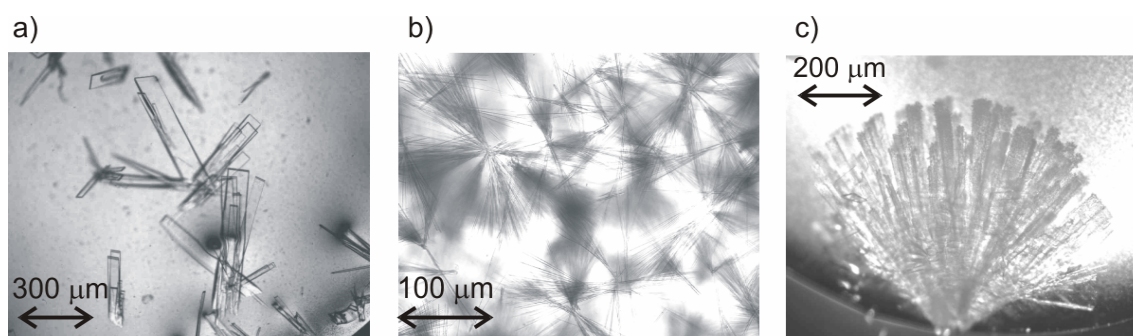


Figure 4.42 Photographs of a) Ras(wt)·Mg $^{2+}$ ·GTP γ S, b) Ras(T35A)·Mg $^{2+}$ ·GTP γ S, and c) Ras(T35S)·Mg $^{2+}$ ·GTP γ S.

Figure 4.42 exhibits the ^{31}P $\{^1\text{H}\}$ CP MAS NMR spectra of Ras(wt)·Mg $^{2+}$ ·GTP γ S. Three well-resolved signals occur at chemical shifts of -10.6, -16.5, and 37.2 ppm (303 K) corresponding to the α -, β -, γ -phosphate group of the nucleotide. The relative intensities of these three signals together with their spinning side band intensities do not behave like 1 : 1 : 1. The reason for this behaviour is, that signals due to GDP (P_α : -10.5 ppm and P_β : -1.9 ppm) resulting from partial hydrolysis of the GTP γ S nucleotide are superimposed to the spectrum of GTP γ S (see Figure 4.43). In addition to these signals, a line at 1.7 ppm occurs which is attributed to the free phosphate coming from the hydrolysis of GTP γ S to GDP. No significant changes in the isotropic chemical shift could be observed by cooling down the sample (see the values in Table 4.16). When the temperature was raised to 303 K the initial spectrum was obtained again. Note that the assignment of the signals could not be verified because of the fast hydrolysis of the GTP γ S nucleotide. Therefore, we have used the assignment used by Spoerner [Spoerner, Ph.D. thesis].

	T / K	$\delta_{\alpha\text{iso}}$ / ppm	$\delta_{\beta\text{iso}}$ / ppm	$\delta_{\gamma\text{iso}}$ / ppm
Ras(wt)·Mg $^{2+}$ ·GTP γ S	303	-10.6	-16.5	37.2
	273	-10.7	-16.7	37

Table 4.16 NMR isotropic chemical shifts of crystalline Ras(wt)·Mg $^{2+}$ ·GTP γ S measured at 303 K and 273 K.

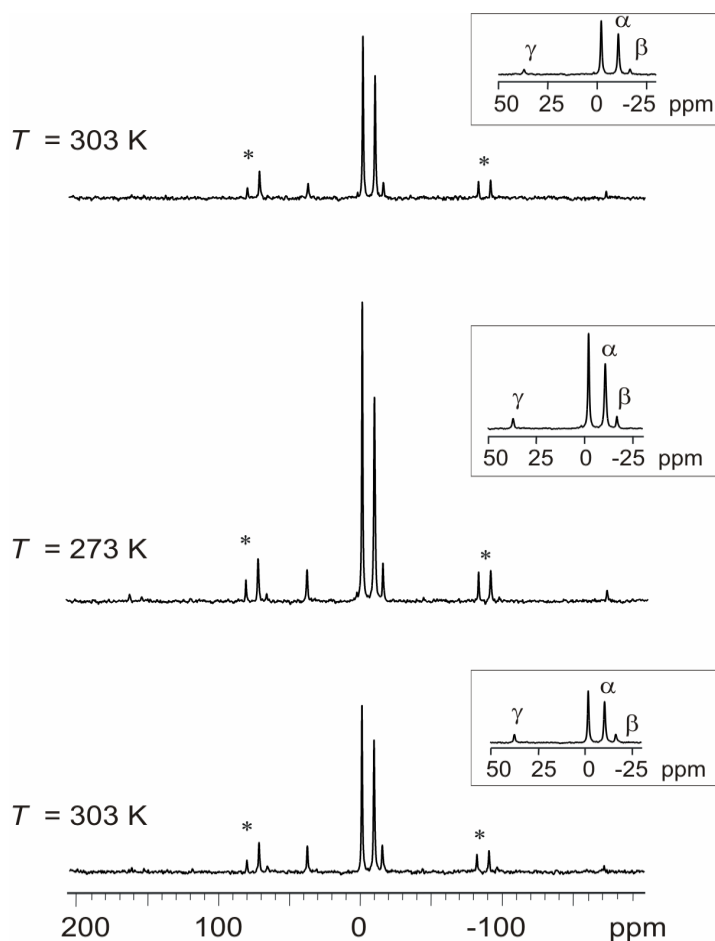


Figure 4.43 1D ^{31}P $\{^1\text{H}\}$ CP MAS NMR spectra of Ras(wt)·Mg $^{2+}$ ·GTP γ S at different temperatures. Spinning side bands are marked with asterisks. The insets show the central lines. The spectra (128 k scans) were recorded at 10 kHz sample spinning rate using TPPM decoupling. The recycle delay was 0.5 s and the cross polarization mixing time was set to 3 ms.

^{31}P $\{^1\text{H}\}$ CP MAS NMR spectra of Ras(T35A)·Mg $^{2+}$ ·GTP γ S and Ras(T35S)·Mg $^{2+}$ ·GTP γ S were acquired (Figure 4.44). The nucleotide hydrolysed faster than the time required for obtaining well resolved 1D spectra of good signal-to-noise (~ 20 h). The signals at -9 ppm and -1.9 ppm in the Ras(T35A)·Mg $^{2+}$ ·GTP γ S spectrum correspond to the α - and β -phosphate group of the GDP. The peaks at -10.2 ppm and -1.8 ppm in Ras(T35S)·Mg $^{2+}$ ·GTP γ S spectrum correspond to α - and β -phosphate group of the GDP while the broad peak at 2.9 ppm is assigned to the free phosphate.

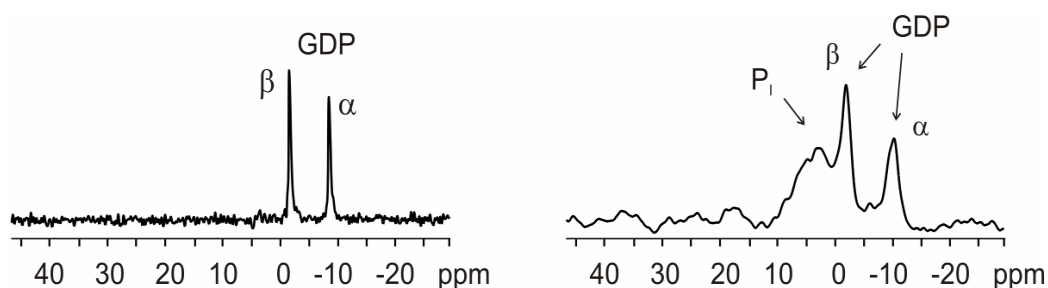


Figure 4.44 1D ^{31}P $\{^1\text{H}\}$ CP MAS spectra of Ras(T35A)·Mg $^{2+}$ ·GTP γ S (left) and Ras(T35S)·Mg $^{2+}$ ·GTP γ S at room temperature. Due to fast GTP γ S hydrolysis, only the GDP signals and the free phosphate peak could be detected.

5. Summary and Conclusions

Before solid-state ^{31}P NMR spectroscopy could be applied to protein samples, the experiments had to be optimised and tested on well-suited model compounds. For this reason solid-state ^{31}P NMR spectroscopy was applied to three phosphorylated amino acids: O-phospho-L-serine, O-phospho-L-threonine, and O-phospho-L-tyrosine. It was shown that these substances can be used as model compounds in order to design and optimise solid-state ^{31}P NMR experiments for the investigation of phosphorylated peptides and proteins. 2D exchange spectra of P-Tyr indicate the presence of slow conformational exchange and - possibly - spin diffusion due to ^{31}P - ^{31}P coupling. Conventional analysis of the cross-peak intensities of a series of 2D EXSY experiments at high decoupling field strength allowed to determine an exchange rate of 6 s^{-1} at 302 K. The 2D PMLG decoupled ^1H - ^{31}P LG-CP HETCOR experiment applied to the three phosphorylated amino acids allowed the assignment of the ^1H signals of NH_2 , POH, and COOH groups. We obtained high resolution in the indirect dimension of the 2D proton-proton correlation spectra of phosphorylated amino acids by employing a 2D ^1H - ^1H experiment where PMLG decoupling was used in the t_1 dimension.

Since variable temperature MAS NMR spectroscopy is of great importance for the study of dynamics in solid-state, the determination of the accurate temperature of the sample under different MAS rates and bearing gas or air flow temperatures was performed using the temperature-dependence of the isotropic chemical shift of the ^{207}Pb resonance of lead nitrate $\text{Pb}(\text{NO}_3)_2$.

The major results of the present work are related to low molecular weight guanosine triphosphate (GTP) binding Ras proteins which play an essential role in a variety of diverse cellular signal transduction and transport processes by cycling between a GTP-bound “on” state and a guanosine diphosphate (GDP) bound “off” state. The present work includes Ras expression, purification, exchange of nucleotides, and crystallization. The crystallization was performed using the sitting drop method. For the NMR measurements, the crystallites were transferred into 2.5 mm rotors. For the first time, we have crystallized the effector loop mutants $\text{Ras}(\text{T35S})\cdot\text{Mg}^{2+}\cdot\text{GppCH}_2\text{p}$, $\text{Ras}(\text{T35S})\cdot\text{Mg}^{2+}\cdot\text{GTP}\gamma\text{S}$, $\text{Ras}(\text{T35A})\cdot\text{Mg}^{2+}\cdot\text{GppCH}_2\text{p}$, and $\text{Ras}(\text{T35A})\cdot\text{Mg}^{2+}\cdot\text{GppNHp}$. The habit of the crystallites is strongly influenced by the effector loop mutations.

After having optimised the experiments, ^{31}P $\{^1\text{H}\}$ CP MAS NMR spectra of Ras proteins of unexpectedly high resolution and signal-to-noise could be obtained. Therefore, proton driven spin diffusion and rotational resonance methods could be applied for determining the accurate assignment of the α -, β -, and γ -phosphate group of the triphosphate nucleotides GppCH₂p and GppNHp complexed to the Ras(wt) and effector loop mutants.

Using the 2D ^{31}P refocused INADEQUATE experiment, an oxygen mediated J -coupling could be observed in the solid-state NMR of proteins for the first time. $\text{P}_\alpha\text{-O-P}_\beta$ connectivity in Ras(wt)·Mg²⁺·GppNHp and Ras(wt)·Mg²⁺·GppCH₂p was clearly indicated by two correlation peaks in the solid-state refocused INADEQUATE spectra. In contrast, the $\text{P}_\beta\text{-O-P}_\gamma$ connectivity did not give rise to cross-peaks. This was due to the small $J(\text{P}_\beta\text{-O-P}_\gamma)$ and, therefore, the low efficiency of excitation of the corresponding DQ coherence.

The presence of two different states, 1 and 2, in Ras(wt)·Mg²⁺·GppCH₂p could be shown by liquid-state ^{31}P NMR spectroscopy but not by solid-state ^{31}P NMR spectroscopy. It was, therefore, assumed that the exchange between these two states was fast in the crystalline sample even at 273 K. The study of the exchange process is, furthermore, complicated by the existence of four molecules in the unit cell. The presence of dynamic disorder was corroborated by the dependence of the linewidth and CP build-up rate on the temperature.

Ras(wt)·Mg²⁺·GppNHp exists in two biological relevant conformational states: state 1 and state 2. State 1 is an "open", disordered conformation of the switch regions similar to the GDP-bound state. State 2 appears to be very similar to the conformation of Ras in the "on" state which is observed for Ras interacting with effector proteins. It was shown that the wild-type protein molecules preferentially exist in state 2. The molecules switch between states 1 and 2. At 273 K, this exchange is slow on the NMR time scale while the exchange becomes fast at 303 K.

The 2D PMLG decoupled ^1H - ^{31}P LG-CP HETCOR experiment was applied for the first time in solid-state ^{31}P NMR spectroscopy of proteins. It was demonstrated that the ^{31}P nuclei of Ras(wt)·Mg²⁺·GppNHp and Ras(wt)·Mg²⁺·GppCH₂p predominantly receive their magnetization from protons of the NH groups of the backbone.

In contrast to the wild-type protein, the mutant protein molecules preferentially exist in the "open" state 1 which makes the nucleotide more accessible to the interaction with other molecules in the crystallites.

Pronounced crystallisation-induced chemical shift changes are observed for Ras(T35A)·Mg²⁺·GppNHp and Ras(T35S)·Mg²⁺·GppNHp, especially for P_α.

Ras(wt)·Mg²⁺·GTPγS also exists in only one conformation. The existence of different substates in fast exchange cannot be excluded. The study of these samples was, however, complicated by fast GTPγS hydrolysis resulting in the formation of GDP. This hydrolysis is even faster for the effector loop mutants than for Ras(wt). Therefore, no reliable information could be obtained from the solid-state ³¹P NMR spectra of GTPγS complexes.

6. Bibliography

- Akasaka, K., Tamada, M., Wang, F., Kariya, K-i., Shima, F., Kikuchi, A., Yamamoto, M., Shirouzu, M., Yokoyamas, S. & Kataoka, T. (1996) *J. Biol. Chem.* **271** (10), 5353-5360.
- Andrew, E. R., Bradbury, A. & Eades, R. G. (1958) *Nature* **182**, 1659-1663.
- Andrew, E. R., Bradbury, A., Eades, R. G. & Wynn, V. T. (1963) *Phys. Lett.* **4**, 99-100.
- Andrew, E. R., Clough, S. Farnell, L. F., Gledhill, T. D. & Roberts, I. (1966) *Phys. Lett.* **21**, 505-506.
- Andrew, E. R., Hinshaw, W. S., Hutchins, M. G. & Canepa, P. C. (1974) *Chem. Phys. Lett.* **26**, 50-52.
- Bae, C. D., Min, D. S., Fleming, I. N. & Exton, J. H. (1998) *J. Biol. Chem.* **273** (19), 11596-11604.
- Balazs, Y. S. & Thomson, L. (1999) *J. Magn. Reson.* **139**, 371-376.
- Baldus, M. Iulicci, R. J. & Meier, B. H. (1997) *J. Am. Chem. Soc.* **119**, 1121-1124.
- Bak, M., Rasmussen, J. T. & Nielsen, N. C. (2000) *J. Magn. Reson.* **147**, 296-330.
- Barbacid, M. (1987) *Annu. Rev. Biochem.* **56**, 779-827.
- Battle, A. R., Platts, J. A., Hambley, T. W. & Deacon, G. B. (2002) *J. Chem. Soc., Dalton Trans.* **2002**, 1898-1902.
- Bax, A., Freeman, R. & Kempell, S. (1980) *J. Am. Chem. Soc.* **102**, 4849-4851.
- Bax, A., Freeman, R. & Frenkiel, T. A. (1980) *J. Am. Chem. Soc.* **103**, 2102-2104.
- Bellew, B. F., Halkides, C. H., Gerfen, G. J., Griffin, R. G. & Singel, D. J. (1996) *Biochemistry* **35**, 12186-12193.
- Bennet, A. E., Rienstra, C. M., Auger, M., Lakshmi, K. V. & Griffin, R. G. (1995) *J. Chem. Phys.* **103**, 6951-6958.
- Bertani, P., Raya, J., Reinheimer, P., Gougeon, R., Delmotte, L. & Hirschinger, J. (1998) *Solid State NMR* **13**, 219-229.
- Bielecki, A. & Burum, D. P. (1995) *J. Magn. Reson.* **116**, 215-220.
- Bivona, T. G., de Castro, I. P., Ahearn, I. M., Grana, T. M., Chiu, V. K., Lockyer, P. J., Cullen, P. J., Pellicer, A., Cox, A. D. & Phillips, M. R. (2003) *Nature* **424**, 694-698.
- Bodenhausen, G., Freeman, R. & Morris, G. A. (1976) *J. Magn. Reson.* **23**, 171-175.
- Bos, J. L. (1989) *Cancer Research* **49**, 4682-4689.
- Bos, J. L. (1997) *Biochim. Biophys. Acta* **1333**, M19-M31.
- Boquet, P. (2000) *Int. J. Med. Microbiol.* **290**, 429-434.
- Bouchard M., Le Guerneve, C. & Augere, M. (1998) *Biochim. Biophys. Acta* **1415**, 181-192.
- Bradford, M. M. (1976) *Analytical Biochemistry* **72**, 248-254.
- Brauer, M. & Sykes, B. (1981) *Biochemistry* **20**, 6767-6775.

- Brown, S. P., Perez-Torralba, M., Sanz, D., Claramunt, R. M. & Emsley L. (2002) *J. Am. Chem. Soc.* **124** (7), 1152-1153.
- Brown, S. P., Perez-Torralba, Sanz, D., Claramunt, R. M. & Emsley, L. (2002) *Chem. Commun.* **2002**, 1852-1853.
- Brunner, E. (1995) *J. Mol. Struct.* **355**, 61-85.
- Brunner, E. & Sternberg, U. (1998) *Progress in NMR Spectroscopy* **32**, 21-57.
- Brus, J. (2000) *Solid State NMR* **16**, 151-160.
- Brünger, A. T., Milburn, M. V., Tong, L., de Vos, A. M., Jancarik, J., Yamaizumi, Z., Nishimura, S., Ohtsuka, E. & Kim, S.-H. (1990) *Proc. Natl. Acad. Sci. USA* **87**, 4849-4853.
- Bryndal L., Picur B. & Lys T. (2002) *Acta Cryst.* **A58** (supplement), C122.
- Burum, D. P. & Rhim, W.-K. (1979) *J. Chem. Phys.* **71** (2), 944-956.
- Cheetham, A. K., Clayden, N. J., Dobson, C. M. & Jakeman, R. J. B. (1986) *J. Chem. Soc., Chem. Commun.* **3**, 195-197.
- Cherfils, J., Menetrey, J., le Bras, G., le Bras, G., Janoueix-Lerosey, I., de Gunzburg, J., Garel, J.-R. & Auzat, I. (1997) *EMBO J.* **16**, 5582-5591.
- Creighton, T. E. (ed.) (2002) *Encyclopedia of Molecular Medicine*, John Wiley and Sons, New York.
- Di Fiore, P. P. (2003) *Nature* **424**, 624-625.
- DiVerdi, J. A. & Spella, S. J. (1981) *Biochemistry* **20**, 280-284.
- Dollase, W. A., Feike, M., Schaller, T., Schnell, I. & Steuernagel, S. (1997) *J. Am. Chem. Soc.* **119**, 3807-3810.
- Duncan, T. M. & Douglas, C. D. (1984) *Chem. Phys.* **87** (3), 339-349.
- Dybowsky, C. & Neue, G. (2002) *Progress in Nuclear Magnetic Resonance Spectroscopy* **41**, 153-170.
- Edzes, H. T. & Bernardis, J. P. C. (1984) *J. Am. Chem. Soc.* **106**, 1515-1517.
- Ernst, M. (2003) *J. Magn. Reson.* **162**, 1-34.
- Ernst, M., Samoson, A. & Meier, B. H. (2001) *Chem. Phys. Lett.* **348**, 293-302.
- Ernst, M., Zimmermann, H. & Meier, B. H. (2000) *Chem. Phys. Lett.* **317**, 581-588.
- Ernst, M., Meier, B., Tomaselli, M. & Pines, A. (1998) *Molecular Physics* **95** (5), 849-858.
- Ernst, M., Bush, S., Kolbert, A. C. & Pines, A. (1996) *J. Chem. Phys.* **105** (9), 3387-3397.
- Ernst, M., Kolbert, A. C., Schmidt-Rohr, K. & Pines, A. (1996) *J. Chem. Phys.* **104** (21), 8258-8268.
- Ernst, M., Detken, A., Böckmann, A. & Meier, B. (2003) *J. Am. Chem. Soc.* **125**, 15807-15810.
- Ernst, R. R., Bodenhausen, G. & Wokaun, A. (1987) *Principles of Nuclear Magnetic Resonance in One and Two Dimensions*, Clarendon Press, Oxford.
- Fayon, F., Le Saout, G., Emsley, L. & Massiot, D. (2002) *Chem. Commun.* **2002**, 1702-1703.
- Fayon, F., King, I. J., Harris, R. K., Gover, R. K. B., Eavens, J. S. O. & Massiot, D. (2003) *Chem. Mater.* **15**, 2234-2239.

- Fayon, F., Massiot, D., Suzuya, K. & Price, D. L. (2001) *J. Non-Crystalline Solids* **283**, 88-94.
- Feig, L. A. (1994) *Current Opin. in Cell Biol.* **6**, 204-211.
- Feig, L. A. & Cooper, G. M. (1988) *Mol. Cell. Biol.* **8**, 3235-3243.
- Ferguson, D. B. & Haw, J. F. (1995) *Anal. Chem.* **67**, 3342-3348.
- Feng, X., Verdegem, P. J. E., Lee, Y. K., Helmle, M., Shekar, S. C., de Groot, H. J. M., Lugtenburg, J. & Levitt, M. H. (1999) *Solid State NMR* **14**, 81-90.
- Franken, S. M., Scheidig, A. J., Kregel, U., Rensland, H., Lautwein, A., Geyer, M., Scheffzek, K., Goody, R. S., Kalbitzer, H. R., Pai, E. & Wittinghofer, A. (1993) *Biochemistry* **32**, 8411-8420.
- Geyer, M., Schweins, T., Herrmann, C., Prisner, T., Wittinghofer, A. & Kalbitzer, H. R. (1996) *Biochemistry* **35**, 10308-10320.
- Geyer, M. & Wittinghofer, A. (1997) *Current Opinion in Structural Biology* **7**, 786-792.
- Geyer, M., Assheuer, R., Klebe, C., Kuhlmann, J., Becker, J., Wittinghofer, A., & Kalbitzer, H. R. (1999) *Biochemistry* **38**, 11250-11260.
- Glennon, T. M., Villa, J. & Warshel, A. (2000) *Biochemistry* **39**, 9641-9651.
- Gorenstein, D. G. (1975) *J. Am. Chem. Soc.* **97**, 898-900.
- Gorenstein, D. G. (1975) *J. Am. Chem. Soc.* **99**, 2254-2258.
- Griffin, R. G., Powers, L. & Pershan, P. S. (1978) *Biochemistry* **17** (14), 2718-2722.
- Grimmer, A. R. (1978) *Spectrochim. Acta* **34A**, 941.
- Grimmer, A. R. (1983) *Chem. Phys. Lett.* **99** (5,6), 487-490.
- Grimmer, A. R., Müller, D., Gözel, G. & Kniep, R. (1997) *Fresenius J. Anal. Chem.* **357**, 485-488.
- Gu Z., Ebisawa, K. & McDermott, A. (1996) *Solid State NMR* **7**, 161-172.
- Hafner, S. & Demco, D. E. (2002) *Solid State NMR* **22**, 247-274.
- Hall, B. E., Bar-Sagi, D. & Nassar, N. (2002) *Proc. Natl. Acad. Sci.* **99** (19), 12138-12142.
- Hardy, E. H., Verel, R. & Meier, B. H. (2001) *J. Magn. Reson.* **148**, 459-464.
- Harris, R. K., Jackson, P., Merwin, L. H., Say, B. J., & Haegelle, G. (1988) *J. Chem. Soc., Faraday Trans.* **84**, 3649-3672.
- Hartmann, S. R. & Hahn, E. L. (1962) *Phys. Rev.* **128**, 2042-2053.
- Hartmann, P., Vogel, J. & Schnabel, B. (1994) *J. Magn. Reson. A* **111**, 110-114.
- Harvey, J. J. (1964) *Nature* **204**, 1104-1105.
- Herrmann, C. & Nassar, N. (1996) *Prog. Biophys. Molec. Biol.* **66** (1), 1-41.
- Herrmann, C., Martin, G. A. & Wittinghofer, A. (1994) *J. Biol. Chem.* **270** (7), 2901-2905.
- Herzfeld, J. & Berger, A. E. (1980) *J. Chem. Phys.* **73**, 6021-6030.
- Herzfeld, J., Griffin, R. G. & Haberkorn, R. A. (1978) *Biochemistry* **17**(14), 2711-2718.
- Hodgkinson, P. & Emsley, L. (1999) *J. Magn. Reson.* **139**, 46-59.
- Hohwy, M., Jakobsen, H. J., Eden, E., Levitt, M. H. & Nielsen, N. C. (1998) *J. Chem. Phys.* **108** (7), 2686-2694.
- Hu, J.-S. & Redfield, A. G. (1997) *Biochemistry* **36**, 5045-5052.

- Huster, D., Kuhn, K., Kadereit, D., Waldmann, H. & Arnold K. (2001) *Angew. Chem. Int. Ed.* **40** (6), 1056-1058.
- Iuliucci, R. J. & Meier, B. H. (1998) *J. Am. Chem. Soc.* **120**, 9059-9062.
- Iuga, A. & Brunner, E. (2004) *Magn. Reson. Chem.* **42**, 369-372.
- Jeneer, J., Meier, B. H., Bachmann, P. & Ernst, R. R. (1979) *J. Chem. Phys.* **71**, 4546-4553.
- John, J., Sohmen, R., Feuerstein, J., Linke, R., Wittinghofer A. & Goody, R. S. (1990) *Biochemistry* **29**, 6058-6065.
- John, J., Rensland, H., Schlichting, I., Vetter, I., Borasio, G. D., Goody, R. S. & Wittinghofer, A. (1993) *J. Biol. Chem.* **268** (2), 923-929.
- Joneson, T., White, M. A., Wigler, M. H. & Bar-Sagi, D. (1996) *Science* **271**, 810-812.
- Krushelnitsky, A., Reichert, D., Hempel, G., Fedotov, V., Schneider, H., Yagodina, L. & Schulga, A. (1999) *J. Magn. Reson.* **138**, 244-255.
- Kuhlmann, J. & Herrmann, C. (2000) *Topics in Curr. Chem.* **211**, 61-116.
- Kumon, A., Kodama, H., Kondo, M., Yokoi F. & Hiraishi, H. (1996) *J. Biochem.* **119**, 719-743.
- Kye, Y.-S., Connolly, S., Herreros, B. & Harbison, G. S. (1999) *Main Group Metal Compounds* **22**, 373-383.
- Langer, B., Schnell, I., Spiess, H. W. & Grimmer, A.-R. (1999) *J. Magn. Reson.* **138**, 182-186.
- Lee, M. & Goldberg, W. I. (1965) *Phys. Rev.* **140** (4A), 1261-1271.
- Lee, Y. K., Kurur, N. D., Helmle, M., Johannessen, O. G., Nielsen, N. C. & Levitt, M. H. (1995) *Chem. Phys. Lett.* **242**, 304-309.
- Lesage, A., Auger, C., Caldarelli, S. & Emsley, L. (1997) *J. Am. Chem. Soc.* **119**, 7867-7868.
- Lesage, A., Bardet, M. & Emsley, L. (1999) *J. Am. Chem. Soc.* **121**, 10987-10993.
- Letcher, J. H. & van Wazer, J. R. (1966) *J. Chem. Phys.* **44**, 815.
- Levitt, M. H., Raleigh, D. P., Creuzet, F. & Griffin, R. G. (1990) *J. Chem. Phys.* **92**, 6347-6364.
- Levitt, M. H. (2001) *Spin Dynamics*, John Wiley & Sons, Chichester, England.
- Li, G. & Zhang, X. C. (2004) *JMB* **340**, 921-932.
- Lowe, I. J. (1959) *Phys. Rev. Lett.* **2**, 258-287.
- Lowy, D. R. & Willumsen, B. M. (1993) *Annu. Rev. Biochem.* **62**, 851-891.
- Ma, J. & Karplus, M. (1997) *Proc. Natl. Acad. Sci. USA* **94**, 11905-11910.
- Malumbres, M. & Pellicer, A. (1998) *Frontiers in Bioscience* **3**, 887-912.
- Maniukiewicz, W., Kwiatkowski, W. & Blessing, R. H. (1996) *Acta Cryst.* **C52**, 1736-1741.
- Martin, R. W. & Zilm, K. W. (2003) *J. Magn. Reson.* **165**, 162-174.
- Maricq, M. M. & Waugh, J. S. (1979) *J. Chem. Phys.* **70** (7), 3300-3316.
- Maricq, M. M. (1982) *Phys. Rev. B.* **25** (11), 6622-6632.
- McCormick, F. (1991) *Environmental Health Perspectives* **93**, 17-18.
- McDowell, L. M., Klug, C. A., Beusen, D. D. & Schaefer J. (1996) *Biochemistry* **35**, 5395-5403.
- Mehring, M. (1983) *Principles of High Resolution NMR in Solids*, Springer, Berlin.

- Mehring, M. & Waugh, J. S. (1972) *Phys. Rev. B.* **5** (9), 3459-3471.
- Meier, B. H. & Earl, W. L. (1987) *J. Am. Chem. Soc.* **109** (26), 7937-7942.
- Mello, L. V., van Aalten, D. M. F. & Findlay, J. B. C. (1997) *Protein Engineering* **10** (4), 381-387.
- Metz, G., Wu, X. & Smith S. O. (1994) *J. Magn. Reson. A* **110**, 219-227.
- Milburn, M. V., Tong, L., deVos, A. M., Bruenger, A., Yamaizumi, Z., Nishimura, S. & Kim, S.-H. (1990) *Science* **24**, 939-945.
- Mott, H. R., Owen, D., Nietlispach, D., Lowe, P. N., Lim, L. & Laue, E. D. (1999) *Nature* **399**, 384-388.
- Muller, N., Lauterbur, P. C. & Goldenson, J. (1956) *J. Am. Chem. Soc.* **78**, 3557-3561.
- Müller, L. (1979) *J. Am. Chem. Soc.* **101** (16), 4481-4484.
- Nielsen, N. C., Bildsoe, H. & Jakobsen, H. J. (1994) *J. Chem. Phys.* **101** (3), 1805-1812.
- Odahara, T., Nishimoto, S., Katsutani, N., Kyogoku, Y., Morimoto, Y., Matsushiro, A. & Akutsu, H. (1994) *J. Biochem.* **115**, 270-278.
- Opella, S. J., Wise, W. B. & DiVerdi, J. A. (1981) *Biochemistry* **20**, 284-290.
- Pai, E. F., Kregel, U., Petsko, G. A., Goody, R. S., Kabsch, W. & Wittinghofer, A. (1990) *EMBO J.* **9**, 2351-2359.
- Pai, E. F., Kabsch, W., Kregel, U., Holmes, K. C., John, J. & Wittinghofer, A. (1989) *Nature* **341**, 209-214.
- Parks, J. R. (1957) *J. Am. Chem. Soc.* **79**, 757.
- Perrin, C. L. & Dwyer T. J. (1990) *Chem. Rev.* **90**, 935-967.
- Pines, A., Gibby, M. G. & Waugh, J. S. (1972) *J. Chem. Phys.* **56**, 1776-1777.
- Pines, A., Gibby, M. G. & Waugh, J. S. (1973) *J. Chem. Phys.* **59**, 569-590.
- Pinheiro, T. J. & Watts, A. (1994) *Biochemistry* **33**, 2451-2459.
- Potrzebowski, M. J., Assfeld, X., Ganicz, K., Olejniczak, S., Cartier, A., Gardiennet, C. & Tekely, P. (2003) *J. Am. Chem. Soc.* **125**, 4223-4232.
- Raiford, D., Fisk, C. & Becker, E. (1997) *Anal. Chem.* **51**, 2050-2051.
- Raleigh, D. P., Levitt, M. H. & Griffin, R. G. (1988) *Chem. Phys. Lett.* **146**, 71-76.
- Raw, A. S., Coleman, D. E., Gilman, A. G. & Sprang, S. R. (1997), *Biochemistry* **36**, 15660-15669.
- Reinstein, J., Schlichting, I., Frech, M., Goody, R. S. & Wittinghofer, A. (1991) *J. Biol. Chem.* **266**, 17700-17706.
- Rhim, W.-K., Elleman, D. D. & Vaughan, R. W. (1973) *J. Chem. Phys.* **58** (4), 1772-1773.
- Rodriguez-Viciana, P., Warne, P. H., Khwaja, A., Marte, B. M., Pappin, D., Das, P., Waterfield, M. D., Ridley, A. & Downward, J. (1997) *Cell* **89** (3), 457-467.
- Rohrer, M., Priesner, T. F., Bruegmann, O., Haess, H., Spoerner, M., Wittinghofer, A., & Kalbitzer, H. R. (2001) *Biochemistry* **40**, 1884-1889.
- Rosay, M., Weis, W., Kreischer, K. E., Temkin, R. J. & Griffin, R. G. (2002) *J. Am. Chem. Soc.* **124**, 3214-3215.

- Sassone-Corsi, P., Cer, C. J., & Verma, I. M. (1989) *Mol. Cell. Biol.* **9**, 3174-3183.
- Scheffzek, K., Ahmadian, M. R., Kabsch, W., Wiesmüller, L., Lautwein, A., Schmitz, F. & Wittinghofer, A. (1997) *Science* **277**, 5324-5333.
- Scheidig, A. J., Burmester, C. & Goody, R. S. (1999) *Structure* **7** (11), 1311-1324.
- Scherer, A., John, J., Linke, R., Goody, R. S., Wittinghofer, A., Pai, E. F. & Holmes, K. C. (1989) *J. Mol. Biol.* **206**, 257-259.
- Schmidt, G. & Wittinghofer, A. (2000) *FEBS Letters* **474** (2-3), 184-188.
- Schmidt-Rohr, K. & Spiess, H. W. (1994) *Multidimensional Solid-State NMR and Polymers*, Academic Press Inc, San Diego.
- Schweins, T., Scheffzek, K., Assheuer, R., & Wittinghofer, A. (1997), *J. Mol. Biol.* **266**, 847-856.
- Scolnick, E. M., Papageorge, A. G. & Shih, T. Y. (1979) *PNAS* **76**, 5355-5359.
- Soares, T. A., Miller, J. H. & Straatsma, T. P. (2001) *Proteins: Structure, Function, and Genetics* **45** (4), 297-312.
- Song, Z., Antzutkin, O. N., Lee, Y. L., Schekar, S. C., Rupprecht, A. & Levitt, M. H. (1997) *Biophys. J.* **73**, 1539-1552.
- Spoerner, M., Herrmann, C., Vetter, I. R., Kalbitzer, H. R. & Wittinghofer, A. (2001) *Proc. Natl. Acad. Sci. USA* **98**, 4944-4949.
- Spoerner, M. (2002) *Ph.D. thesis*.
- Spoerner, M., Nuehs, A., Ganser, P., Herrmann, C., Wittinghofer, A. & Kalbitzer, H. R., *Biochemistry*, accepted.
- Stejskal, E. O. & Schaefer J. (1977) *J. Magn. Reson.* **28**, 105-112.
- Sternberg, U., Pietrowski, F. & Priess, W. (1990) *Z. Phys. Chem.* **168**, 115-128.
- Stumber, M., Geyer, M., Graf, R., Kalbitzer, H. R., Scheffzek, K. & Haebleren, U. (2002) *J. Mol. Biol.* **323**, 899-907.
- Stumber, M., Herrmann, C., Wohlgemuth, S., Kalbitzer, H. R., Jahn, W. & Geyer, M. (2002) *Eur. J. Biochem.* **269**, 3270-3278.
- Suga, T., Inubushi, C. & Okabe, N. (1998) *Acta Cryst.* **C54**, 83-85.
- Sundaralingam, M. & Putkey, E. F. (1970), *Acta Cryst.* **B26**, 790-800.
- Suter, D. & Ernst, R. R. (1982) *Phys. Rev. B* **25**, 6038-6041.
- Schweins, T., Scheffzek, K., Assheuer, R. & Wittinghofer, A. (1997) *J. Mol. Biol.* **266**, 847-856.
- Szeverenyi, N. M., Sullivan, M. J. & Maciel, G. E. (1982) *J. Magn. Reson.* **47**, 462-475.
- Szeverenyi, N. M., Bax, A. & Maciel, G. E. (1983) *J. Am. Chem. Soc.* **105**, 2579-2582.
- Takai, Y., Sasaki, T. & Matozaki, T. (2001) *Physiol. Rev.* **81**, 153-208.
- Tanokur, M. & Suzuki, Y. (1999) *Mol. Cell. Biochem.* **190**, 75-83.
- Tong, L., de Vos, A. M., Milburn, M. V. & Kim, S.-H. (1991) *J. Mol. Biol.* **217**, 503-516.
- Tucker, J., Sczakiel, G., Feuerstein, J., John, J., Goody, R. S. & Wittinghofer A. (1986) *EMBO J.* **5**, 1351-1358.

- Turner, G. L., Smith, K. A., Kirkpatrick, R. J. & Oldfield, E. (1986) *J. Magn. Reson.* **70**, 408-415.
- Un, S. & Klein, M. P. (1989) *J. Am. Chem. Soc.* **111**, 5119-5124.
- van Dam, L. & Levitt, M. H. (2000) *JMB* **304**, 541-561.
- van Rossum, B.-J., Boender, G. J. & de Groot, H. J. M. (1996) *J. Magn. Reson. A* **120**, 274-277.
- van Rossum, B.-J., de Groot, C. P., Ladizahansky, V., Vega, S. & de Groot, H. J. M. (2000) *J. Am. Chem. Soc.* **122**, 3465-3472.
- van Rossum, B.-J., Förster, H. & de Groot H. J. M. (1997) *J. Magn. Reson.* **124**, 516-519.
- van Wazer, J. R. (1956) *J. Am. Chem. Soc.* **78**, 5709-5715.
- Verdegem, P. J. E., Helmle, M., Lugtenburg, J. & de Groot, H. J. M. (1997) *J. Am. Chem. Soc.* **119**, 169-174.
- Verel, R., van Beek, J. D. & Meier, B. H. (1999) *J. Magn. Reson.* **140**, 300-303.
- Veter, I. R. & Wittinghofer, A. (2001) *Science* **294**, 1299-1304.
- Vinogradov, E., Madhu, P. K. & Vega, S. (1999) *Chem. Phys. Lett.* **314**, 443-450.
- Vinogradov, E., Madhu, P. K. & Vega, S. (2000) *Chem. Phys. Lett.* **329**, 207-214.
- Vojtek, A. B. & Der, C. J. (1998) *J. Bio. Chem.* **273** (32), 19925-19928.
- Wang, Y. L., Belton, P. S. & Tang, H. R. (1999) *Solid State NMR* **14**, 19-32.
- Waugh, J. S., Huber, L. M. & Haeberlen, U. (1968) *Phys. Rev. Lett.* **20** (5), 180-182.
- White, M. A., Nicolette, C., Minden, A., Polverino, A., van Aelst, L., Karin, M. & Wigler, M. H. (1995) *Cell* **80**, 533-541.
- Willingham, M. C., Pastan, I., Shih, T. Y. & Scolnick, E. M. (1980) *Cell* **19**, 1005-1014.
- Wittinghofer, F. & Pai, E. F. (1991) *Trends Biochem. Science* **16**, 382-387.
- Wittinghofer, F., Krengel, U., John, J., Kabsch, W. & Pai, E. F. (1991) *Environmental Health Perspective* **93**, 11-15.
- Wittinghofer, A. & Hermann, C. (1995) *FEBS Letters* **369**, 52-56.
- Wittinghofer, A. & Waldmann, H. (2000) *Angew. Chem. Int. Ed.* **39**, 4192-4214.
- Wittinghofer, A. & Nassar, N. (1996) *Trends Biol. Sci.* **21**, 488-491.
- Zang, J. & Matthews, C. R. (1998) *Biochemistry* **37**, 14881-14890.
- Zhang, Z., Kennedy, J. H. & Eckert, H. (1992) *J. Am. Chem. Soc.* **114**, 5775-5784.

Acknowledgments

Many grateful thanks are due to my supervisor Prof. Dr. Eike Brunner who initiated this interesting project. I am very grateful for allowing me to penetrate into the fabulous world of solid-state NMR, and for all his help, support, and guidance I received during the last three years. I appreciate how you identify yourself with your students' research, the respect you inspire to us; all that and much more making you the best supervisor. Thank you.

During my PhD, I had the opportunity to also work in the modern lab of Prof. Dr. Dr. Hans Robert Kalbitzer and I thank him for this chance. The experience of his biochemistry group was extremely useful for the progress of my research.

I am very grateful to Dr. Michael Spoerner for all the things he taught me, for his patience, his enthusiastic way of tackling problems. I do appreciate and thank you all for your time, assistance, and outstanding help.

Many warm thanks to Dr. Michael Wenzler and Dr. Bjoern Heitmann for instructive discussions, help in a variety of topics and especially for the funny, joyful, and relaxed atmosphere in our office. Special thanks to their desks followers: Sonja Lorenz, Matthias Meier, Katharina Lutz, and Max Stadler who maintained this nice atmosphere.

I would like also to thank my friendly solid-state NMR colleagues: Daniela Baumer, Alexander Fink, and Christian Groeger for the stimulating discussions during group meetings and seminars.

I would like to thank Mrs. Ingrid Cuno. She was very kind in offering her comments on this manuscript. I am very grateful to her and to Mrs. Ingrid Kulbartz for help in the administrative work.

I also thank Petra Ganser, Christina Schreier, Andrea Nuehs, Emmi Fuchs, Roland Hofweber, and Doerte Rochelt for their help during my lab working period; Dr. Wolfram Gronwald and Peter Geyer for assisting me with computer problems; Sabine Ruppel, Kurt Schindler, and Gunnar Schmidt for technical support.

A special thank to Birgit and Juergen Klar from the Physiology Department for allowing me to take photographs of our beautiful Ras crystals.

I would like to thank all the other people of our department for the friendly working environment that made my Regensburg life experience very pleasant.

Finally, I would like to acknowledge financial support from the Deutsche Forschungsgemeinschaft.

Erklärung

Hiermit erkläre ich, dass ich die vorliegende Arbeit selbständig angefertigt und keine anderen als die angegebenen Quellen and Hilfsmittel benutzt habe.

Regensburg, Oktober 2004

Adriana Iuga